The Pennsylvania State University

The Graduate School

INFLUENCE OF MICROSTRUCTURE ON THE MULTIAXIAL PLASTICITY AND FRACTURE OF DUAL PHASE STEELS: EXPERIMENTS AND MULTISCALE COMPUTATIONAL MODELING

A Dissertation in

Materials Science and Engineering

by

Shipin Qin

Submitted in Partial Fulfillment

of the Requirements

for the Degree of

Doctor of Philosophy

May 2020

The dissertation of Shipin Qin was reviewed and approved * by the following:

Allison M. Beese

Associate Professor of Materials Science and Engineering and Mechanical Engineering

Dissertation Advisor

Chair of Committee

Zi-Kui Liu

Distinguished Professor of Materials Science and Engineering

Hojong Kim

Assistant Professor of Materials Science and Engineering

Charles E. Bakis

Distinguished Professor of Engineering Science and Mechanics

John C. Mauro

Professor of Materials Science and Engineering

Chair of the Intercollege Graduate Degree Program in Materials Science and Engineering

Abstract

As a class of advanced high strength steels (AHSS), dual phase (DP) steels are widely used in the automobile industry for their high strength to weight ratio. DP600 is a type of DP steel that have a tensile strength of 600 MPa or higher, and its microstructure is comprised of a soft ferrite phase and a hard martensite phase. The thesis focuses on identifying the multiaxial plasticity and fracture behavior of DP600 at the continuum level and understanding the influence of the heterogeneous microstructure on the macroscopic behavior.

The multiaxial plasticity behavior of DP600 was determined through macroscopic mechanical tests under five stress states. A continuum-level plasticity model was developed based on the experimental results. The plasticity model was found to accurately predict the multiaxial mechanical response of the material through macroscopic simulations. A representative volume element (RVE) model based on the observed microstructures was built, which was able to predict the macroscopic multiaxial plasticity behavior of the material from the microstructural level.

The stress state dependent fracture behavior of DP600 steel at the continuum level was investigated through a combined experimental and computational approach. A range of specimen geometries were used to probe the fracture behavior of the material under different stress states. Using an isotropic J2 plasticity framework, finite element simulations of all experiments captured the experimental force displacement curves, and provided information on the evolution of equivalent plastic strain, stress triaxiality, and Lode angle parameter with applied deformation at the location of eventual fracture

initiation. The calculated local failure strain as a function of stress state was used to calibrate the modified Mohr-Coulomb (MMC) fracture model.

At the microstructure level, fracture can initiate within the ferrite phase, the martensite phase, or at the interfaces between these phases, and the dominant fracture initiation mechanism is expected to depend on a number of factors, including the phase and interface properties as well as the applied stress state. An idealized RVE model containing a circular martensite particle was loaded under five different stress states. The RVE model incorporated a ductile fracture criterion for ferrite, a brittle fracture criterion for martensite, and a cohesive zone model (CZM) for the ferrite/martensite interface. A parametric study was performed to determine the relative influence of fracture properties of each constituent and stress state on the failure initiation behavior, and to identify the conditions under which the fracture initiation behavior was stress state dependent.

To study the fracture behavior in a more realistic microstructure, an RVE model based on the microstructure of DP600 was built. Fracture models for ferrite and martensite were incorporated into the RVE model for fracture simulations. Five RVE level failure criteria were presented, and their ability to predict the macroscopic stress state dependent fracture behavior of the material was discussed. To isolate the effect of microstructural heterogeneity on stress state dependent behavior, simulations were performed with the ferrite fracture model to be either stress state dependent or stress state independent. In both cases, the RVE strain to failure was stress state dependent, indicating that the microstructural inhomogeneity, which resulted in strain localization in the microstructure, plays an important role in the stress state dependent fracture behavior of DP600. Simulations revealed that in DP600, microcracks initiated from martensite first, regardless

of the global stress state. Under low stress triaxiality loading, the material fails by the propagation of these martensite microcracks into ferrite, accompanied by new microcracks initiation from both phases; while under high stress triaxiality loading, new microcrack initiated from ferrite subsequently, and the material fails by ferrite microcrack propagation.

Table of Contents

List of Figures

List of Tables

Acknowledgements

I wish to express my deepest gratitude to my advisor, Professor Allison Beese, for her invaluable guidance and consistent encouragement during my Ph.D. study. Without her support, the research in this thesis would be impossible for me to finish. She not only broadened my scientific knowledge, but also shaped my way of working and thinking, which will be a treasure of my future career and life.

My special thanks go to Professor Zi-Kui Liu and Dr. Shun-Li Shang for their valuable suggestions and insightful discussions on my research.

I also want to thank the rest of my committee, Professor Hojong Kim and Professor Charles Bakis, for their critical comments that make this thesis better.

I would like to thank my colleagues, Dr. Zhuqing Wang, Alexander Wilson-Heid, Lourdes Bobbio, John Shimanek, Cole Britt, and John O'Brien for their help and suggestions on both research and life.

I gratefully acknowledge the financial support of my research from National Institute of Standards and Technology (NIST, contract number 60NANB15D284), Office of Naval Research (ONR, contract number N00014-17-1-2567), and Department of Energy (DOE, award number DE-FE0031553).

Finally, I would like to thank my parents for their unconditional support over the past years. Their love will always motivate me to move forward.

Chapter 1 Introduction

Advanced high strength steels (AHSS) are widely used in the automobile industry for vehicle lightweighting as they simultaneously exhibit high strength and ductility due to their multiphase microstructures [1]. The first generation AHSS include dual phase (DP) steels, complex phase (CP) steels, and transformation induced plasticity (TRIP) steels [2]. Among them, DP steels are composed of relatively soft ferrite and relatively hard martensite [3,4]. The martensite enhances the strength of the material over purely ferritic steel, but also makes the microstructure inhomogeneous, resulting in strain partitioning between the two phases upon loading. The mechanical properties of DP steels depend on those of the two constituent phases, the volume fraction of the phases, the distribution of phases, and the morphology of the phases. At the microstructural level, the mechanical properties of the ductile ferrite depend primarily on its chemical composition [5], grain size [6], and initial dislocation density [7], while the mechanical properties of the martensite depend primarily on its carbon content [8].

1.1. Continuum scale mechanical behavior

The multiaxial plasticity and fracture behavior of AHSS at the continuum scale have been extensively investigated. Using a multiaxial testing technique developed in ref. [9], Mohr et al. investigated the multiaxial plasticity behavior of DP590 and TRIP780 under uniaxial tension and seven multiaxial loading states along three different orientations [10]. The authors modeled the material behavior using both associated plasticity models and non-associated plasticity models and showed that both types of model can well capture

the stress strain response under multiaxial loading, but the non-associated plasticity model provided better estimate of the thinning behavior. Using an optimized butterfly specimen [11], four tensile specimens, and a punch specimen, Dunand and Mohr investigated the stress state dependent fracture behavior of TRIP780 under nine different stress states [12]. They evaluated the predictive capability of the shear modified Gurson model [13] and the modified Mohr-Coulomb (MMC) model [14], and concluded that the MMC model can better predict the experimental data, with an error of less than 4%.

Lian et al. [15] experimentally investigated the damage initiation behavior of DP600 for stress states near pure shear, uniaxial tension, and plane strain tension. They defined the instant of damage initiation in each experiment as the moment in which material discontinuity, due to void coalescence, microcrack formation, or shear band formation, was identified using the direct current potential drop method. Habibi et al. [16] studied the stress state dependent fracture behavior of DP600 and calibrated five uncoupled fracture models, including the modified Mohr-Coulomb (MMC) model [14]. While Lian et al. [15] defined failure as a discontinuity at the microscale, Habibi et al. [16] defined failure by the complete loss of load bearing capability of the material.

1.2. Fracture mechanisms of DP steels

The presence of martensite within the ferrite matrix in DP steels gives rise to local deformation inhomogeneities during macroscale deformation, which lead to fracture initiation on the microscale. Reported fracture mechanisms at the microscale in DP steels include ferrite/martensite interface decohesion [17–19], martensite fracture [17,18,20], and deformation localization in ferrite [20–22]. Nevertheless, the dominant fracture

mechanisms, particularly as a function of stress state, are unclear, and contradicting results have been reported in the literature [23–27].

Experimental results have shown examples of each of the three local fracture mechanisms dominating failure. Szewczyk and Gurland found that in dual phase high strength low alloy (HSLA) VAN-QN steel with a martensite volume fraction of 15-20%, voids were formed by martensite/ferrite interface decohesion [19]. Through *in situ* tensile tests on an austenitic-ferritic duplex stainless steel, Guo et al. found that regions of clustered hard phase in a soft matrix resulted in early crack initiation in the matrix initiating from damage accumulation at the ferrite-austenite interface [28]. Jafari et al. investigated the influence of martensite morphology and distribution on local fracture behavior in DP780, and found that under macroscopic uniaxial tension, voids tended to nucleate via ferrite/martensite interface decohesion between closely spaced martensite grains enclosed by large ferrite grains [23]. Conversely, Saeidi et al. concluded from uniaxial and notched tension tests on DP780 that regardless of stress state, voids primarily nucleated via martensite fracture, followed by ferrite/martensite interface decohesion [25,26].

Calcagnotto et al. investigated experimentally the deformation and failure behavior of three DP steels with similar volume fractions of martensite but different grain sizes, and found that the strain partitioning was extensive in the coarse-grained DP steel (ferrite grain size ~ 12 μm), resulting in strain localization in the ferrite phase and early cracking in martensite. Upon grain refinement, the strain partitioning was reduced, leading to better interface cohesion, and delayed void formation, which was attributed to grain size strengthening of ferrite [29]. Void nucleation from ferrite in DP600 under biaxial tension was reported by Tasan et al. [30,31]. Most of the studies in the literature have inspected

only uniaxial tension [19–24,27], which limits the understanding of local dominant failure mechanisms over a range of stress states.

The above variations in experimental observations can be partially attributed to differences in martensite features (including volume fraction, size, morphology, etc.), phase and interface properties, and global stress state. Additionally, our previous study [32] showed that the local stress state in the ferrite depends on both the global stress state and the local phase configurations in the microstructure. Therefore, the effects of martensite morphology and global stress state on the fracture mechanisms of DP steels are strongly coupled.

1.3. Representative volume element modeling of DP steels

Representative volume element (RVE) modeling has been used to study microstructure based deformation and fracture mechanisms of multi-phase steels [33–36]. With a suitable RVE and constitutive equations, this type of modeling provides micromechanics insight as it enables the inspection of local stresses, strains, and potentially damage mechanisms in the material during deformation. Required inputs for RVE modeling include the mechanical properties of individual phases [37] and the interfacial properties between phases [34,38], which are very challenging to determine experimentally. Experimental studies have been performed to determine the constitutive behavior of individual phases through direct methods, such as micro-pillar compression [39–43] and nanoindentation [44,45], as well as through indirect methods, such as *in situ* neutron diffraction [46] and *in situ* high energy X-ray diffraction (HEXRD) [36]. Some investigators have simply used the constitutive relationships of single phase martensitic

and ferritic steels to represent the constitutive behavior of the individual phases in their DP steels [36,47].

Due to difficulties with experimentally determining constitutive behavior of disparate phases, some researchers have predicted the initial yield stresses of individual phases based on their chemical composition, and their strain hardening behavior based on dislocation density evolution [23,33,37,48,49] through the use of an empirical model proposed by Rodriguez and Gutierrez [5]. The constitutive behaviors of both ferrite and martensite from computational and experimental studies in the literature are shown in Figure 1.1. Note that when comparing properties from different studies, it is important to recognize that the mechanical properties of each phase is affected by many factors, including heat treatment, chemical composition, and grain size, resulting in a spread in reported properties.

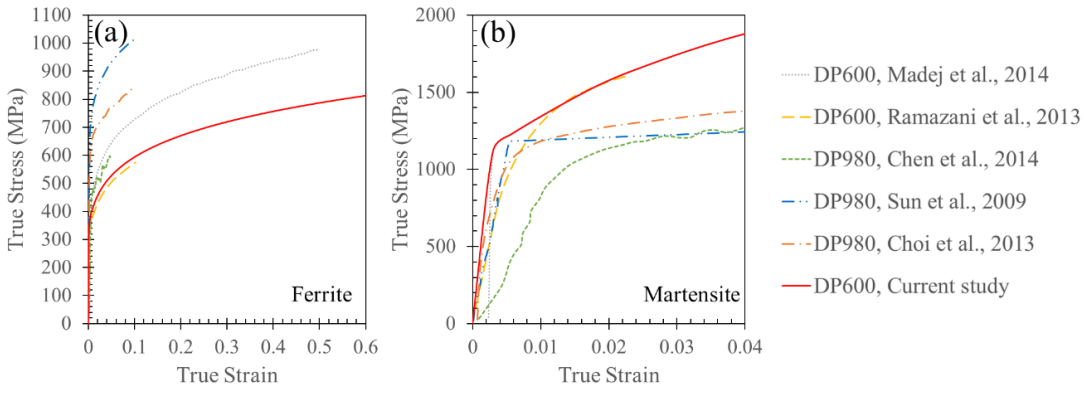

Figure 1.1: True stress-strain behavior for (a) ferrite and (b) martensite reported in the literature. The solid (red) lines show the behavior for each phase adopted in current study. Note that for martensite, the adopted true stress-strain curve is that in [39].

Researchers have been using RVE models for investigating the fracture behavior in the microstructure of DP steels. Uthaisangsuk et al. used a cohesive zone model (CZM) to

simulate the martensite/ferrite interface decohesion in DP600 and TRIP600, and the Gurson-Tvergaard-Needleman (GTN) model [50] in ferrite to simulate its stress-state dependent ductile fracture behavior, but they did not consider martensite cracking [35]. Their simulation accurately predicted the failure strain of DP600 in a hole expansion test, but underestimated the failure strain of TRIP600 in a Nakazima stretch test. Sirinakorn and Uthaisangsuk developed RVE models for DP600 and DP1000 steels, in which the martensite fracture behavior was modeled through a cohesive zone model with the extended finite element method (XFEM), and the ferrite fracture behavior was modeled using the MMC model [51]. They loaded their model under uniaxial tension, and their simulation results revealed that the damage initiation in DP steels was dominated by the damage in ferrite. Ramazani et al. applied a traction-separation law through the extended finite element method (XFEM) to simulate the fracture of martensite particles in four types of DP steel, but assumed perfect bonding at the ferrite/martensite interface, and did not consider damage in ferrite [34]. The DP steels they used had different martensite volume fraction, carbon content, and subsequently ultimate tensile strengths, and the RVE simulations' prediction of the homogeneous strains at which martensite cracked matched well with experimental results. In simulations of DP980, Choi and co-workers also found that the strain at localization and the failure strain of the material decreased with an increase in the strength difference between martensite and ferrite [52].

The RVE modeling of DP steels reported in the literature [23,24,36,52,53] has been primarily limited to loading under uniaxial tension, but there have also been studies considering the influence of stress state on the fracture behavior of DP steels through RVE simulations [35,49,54–56]. Gerbig et al. developed RVE models for two DP steels with

similar strength but different ductility, and implemented the Gurson-Tvergaard-Needleman (GTN) model [50,57] to both the ferrite and the martensite phase [56]. They calibrated the GTN model parameters with simulation results from a void cell model (i.e., a solid cube with a microvoid at the center), and then predicted the stress state dependent fracture strains of the two DP steels at the high stress triaxiality range (stress triaxiality between 1 to 3).

While RVE models have been subjected to multiaxial loadings in some studies, only a few of them validated the simulation results with multiaxial loading experimental data [35,49]. Lian et al. loaded an RVE model of DP600 to uniaxial tension, plane strain tension, and equi-biaxial tension [49], and predicted a stress state dependent damage initiation strain that agree well with macro scale experiments. In their simulations, the authors did not apply any fracture model to the constituent phases; instead, the stress drop in the simulations due to microstructure inhomogeneity was taken as an indication of damage, and the strain at the maximum stress was taken as the damage initiation strain. In another study, Uthaisangsuk et al. loaded their RVE models under different stress state through a multiscale approach [35]. The authors performed macroscale finite element simulations for a Nakazima stretching test and a hole expansion test, and the local deformation field at the site where crack initiated experimentally was adopted as the boundary conditions in the microscale RVE simulations. Their RVE models adopted the Gurson-Tvergaard-Needleman (GTN) model [50,57] to simulate ferrite fracture and a cohesive zone model to simulate ferrite/martensite interface decohesion. The moment when fracture initiated from the microscale RVE model was mapped back to the macroscale simulations, and the corresponding displacement was taken as the damage initiation displacement, which agreed well with experiments.

Since it is well accepted that the eventual failure behavior of metals is stress state dependent [12,58–60], for a mechanistic understanding of failure in DP steels, a comprehensive investigation of the stress state dependence of deformation inhomogeneity and fracture mechanisms DP steels is important.

1.4. Definition of stress state

During metal shaping or forming, within structural components under load, or during machining operations, stress state varies depending on factors including loading type (e.g., tension, shear) and sample geometry. Additionally, at the microscale, the stress state can vary locally due to microstructural heterogeneities. The stress state of a material can be described by two parameters: stress triaxiality, η, and Lode angle parameter, $\bar{\theta}$. Stress triaxiality is defined as:

$$\eta = \frac{\sigma_m}{\sigma_{vM}} \qquad \text{Eq. 1.1}$$

where $\sigma_m = \frac{1}{3} tr(\boldsymbol{\sigma})$ is the mean stress, $\sigma_{vM} = \sqrt{\frac{3}{2}\boldsymbol{s}:\boldsymbol{s}}$ is the von Mises equivalent stress, $\boldsymbol{\sigma}$ is the Cauchy stress tensor, $\boldsymbol{s} = \boldsymbol{\sigma} - \sigma_m \boldsymbol{I}$ is the deviatoric stress tensor, and $\boldsymbol{I}$ is the second order identity tensor.

The Lode angle parameter is defined as:

$$\bar{\theta} = 1 - \frac{2}{\pi}\arccos\left(\frac{3\sqrt{3}}{2}\frac{J_3}{\sqrt{J_2^3}}\right) \qquad \text{Eq. 1.2}$$

where $J_2 = \sqrt{\frac{1}{2}\boldsymbol{s}:\boldsymbol{s}}$ and $J_3 = \det(\boldsymbol{s})$ are the second and third invariants of the deviatoric stress tensor, respectively.

For a state of plane stress ($\sigma_3 = 0$), the relationship between stress triaxiality and Lode angle parameter is given as [58]:

$$\sin\left(\frac{\pi}{2}\bar{\theta}\right) = -\frac{27}{2}\eta\left(\eta^2 - \frac{1}{3}\right) \qquad \text{Eq. 1.3}$$

This relationship is shown in Figure 1.2.

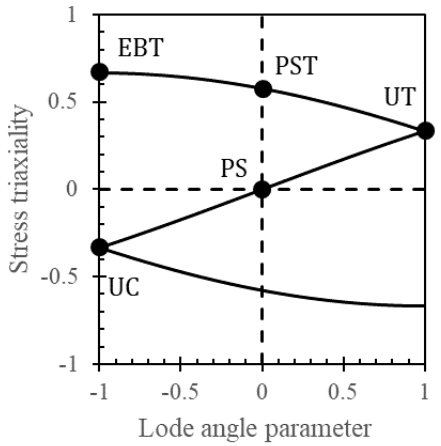

Figure 1.2: Stress triaxiality versus Lode angle parameter for a range of stress states (uniaxial compression (UC), pure shear (PS), uniaxial tension (UT), plane strain tension (PST), and equi-biaxial tension (EBT)), with the line denoting the relationship between these parameters for plane stress.

1.5. Thesis outline

The objective of this thesis is to determine the multiaxial plasticity and fracture behavior of DP600 at the macroscale and understand the connection between the macroscopic behavior and the microscopic mechanisms. Macroscopic experiments, continuum level simulations, and microstructure based simulations were performed. The thesis is arranged as the following chapters:

In Chapter 2, the multiaxial plasticity behavior of DP600 steel is evaluated through macroscopic testing and predicted through both continuum and micromechanics simulations. The stress state dependent mechanical properties of the material are examined through multiaxial loading under five stress states.

In Chapter 3, the continuum level stress state dependent fracture behavior of DP600 steel is investigated through a combined experimental and computational approach. The fracture behavior of the material under different stress states is experimentally determined by the adoption of different specimen geometries. Fracture strains under different stress state are determined by combining experimental data with finite element simulations. The MMC model is calibrated to describe the stress state dependent fracture strain of DP600.

In Chapter 4, an idealized RVE model containing a circular martensite particle is developed to study the relationship among fracture initiation behavior, phase/interface properties, and stress state in DP steels. A ductile fracture criterion for ferrite, a brittle fracture criterion for martensite, and a cohesive zone model (CZM) for the ferrite/martensite interface are implemented in the idealized RVE model. The relative influence of fracture properties of each constituent and stress state on the failure initiation behavior is investigated through a parametric study.

In Chapter 5, a microstructure based RVE model is developed to simulate the microstructural level fracture behavior of DP600. Five microstructural level failure criteria are investigated. The influence of the microstructure inhomogeneity on the stress state dependent fracture behavior is discussed.

Chapter 6, a summary and conclusions, as well as suggested future research, are presented.

Chapter 2 Micromechanics of multiaxial plasticity of DP600: experiments and microstructural deformation modeling[1]

2.1. Introduction

In order to develop a predictive plasticity model for DP steels, the effect of microstructure on deformation mechanisms must be understood. Three microstructural damage mechanisms in DP steels have been reported in the literature: martensite/ferrite interface decohesion [17–19], martensite cracking [17,18,20], and deformation localization in ferrite [20–22]. Despite extensive research, it is not clear which mechanisms dominate as a function of stress state. In addition to stress state, martensite volume fraction, martensite distribution and morphology, and the strain hardening behaviors of martensite and ferrite are expected to significantly influence the dominant deformation mechanisms.

In this chapter, the multiaxial plasticity behavior of DP600 was studied through a combination of macroscopic multiaxial tests, continuum modeling, microstructural evaluation, and micromechanics-based modeling. Micromechanics simulations were performed using an RVE model, which was calibrated using uniaxial tension tests. The macroscopic behavior under multiaxial deformation was compared with both continuum and micromechanics-based simulations. Through micromechanics simulations, the localization behavior of the material under different stress states was inspected. In this chapter, the material used is described in Section 2.2. The multiaxial mechanical

[1] Reproduced from: Qin, S., McLendon, R., Oancea, V. and Beese, A.M., 2018. Micromechanics of multiaxial plasticity of DP600: Experiments and microstructural deformation modeling. *Materials Science and Engineering: A*, 721, pp.168-178.

experiments and corresponding continuum simulations are discussed in Section 2.3. Section 2.4 introduces the micromechanics modeling procedure, including RVE modeling steps, model calibration, and multiaxial loading of the model. Section 2.5 compares experimental observations and computational results.

2.2. Material

The material used in this study was 1 mm thick DP600 (UTS $\geqslant$ 600 MPa) rolled sheet, whose specified chemical composition was (in wt.%): 0.17 C, 0.08 P, 0.015 S, 0.2 Cu, 0.5 Ni 1.4 Cr+Mo, 4.75 Mn+Al+Si, and 0.35 V+Nb+Ti [61]. Optical microscope (OM) images obtained after conventional polishing followed by etching with 2 vol% Nital for 18 s showed the presence of ferrite and martensite. Ferrite grains were equiaxed, with an average diameter of 6 ± 1.6 μm. A representative image is given in Figure 2.1. Through image processing analysis, the area fraction of martensite was found to be 22% ± 3%. Electron backscatter diffraction (EBSD) analysis results shown in Figure 2.2 indicated that there was no preferred texture in the rolled material.

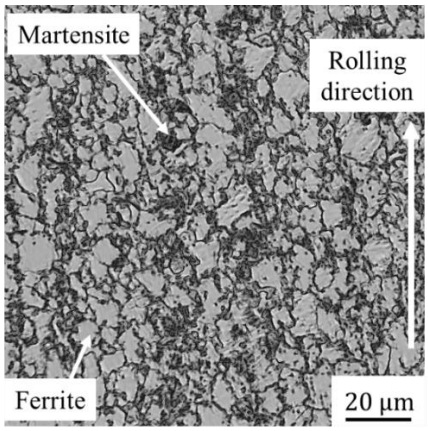

Figure 2.1: Optical micrograph in the rolling plane of as-received DP600. The bright regions are ferrite and dark regions are martensite.

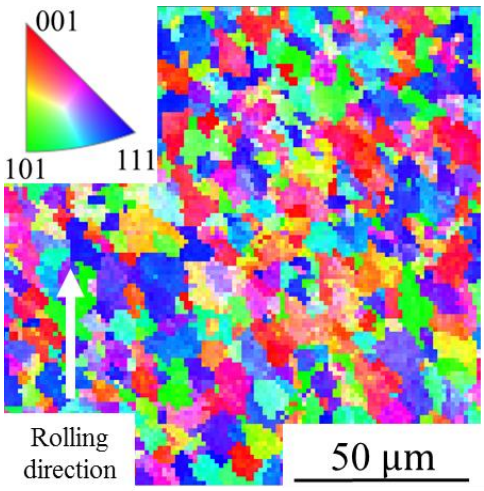

Figure 2.2: EBSD map of the rolling plane of DP600, indicating no preferred orientation of grains whose hkl normals are normal to the surface of the sheet.

2.3. Experimental methods

2.3.1. Uniaxial tension tests

Uniaxial tension tests were performed using specimens with gauge dimensions of $50\ \text{mm} \times 12.5\ \text{mm} \times 1\ \text{mm}$, in compliance with ASTM-E8 [62]. Specimens were extracted along three orientations in the plane of the sheet: the rolling direction (RD), the transverse direction (TD), or 90° from the RD, and 45° from the RD. Two uniaxial tension tests were performed in each direction. Tensile testing was performed under displacement control using a servomechanical test frame (Instron 4202 with a 10 kN load cell), under quasi-static strain rates on the order of $10^{-4}\ s^{-1}$. Strains were measured using Digital Image Correlation (DIC, Vic2D, Correlated Solutions, West Columbia, SC). The gauge section of each specimen was painted white with a random black speckle pattern, and images were taken at 1 Hz using a digital camera (Point Grey GRAS-50S5M-C) throughout

deformation. These images were then analyzed using Vic2D software to compute the evolving deformation fields using a cubic B-spline interpolation algorithm with a virtual strain gauge size of 56 pixels by 56 pixels (~ 3.8 mm by 3.8 mm) [63]. The strain evolution along the tensile loading direction (denoted as the *y*-direction in this paper) in each test was calculated using a 48 mm long virtual extensometer. To determine the constitutive relationship after necking, a continuum level finite element simulation was performed, in which one quarter of the specimen was modeled and discretized by 4664 3D linear elements with reduced integration (C3D8R, ABAQUS version 2016 [64]).

2.3.2. Multiaxial loading tests

Multiaxial loading tests were performed to measure the macroscopic plasticity behavior using the specimen geometry in Figure 2.3 and a custom-built dual actuator hydraulic test machine (MTS Systems Corp.) at the Pennsylvania State University. A schematic of the dual actuator hydraulic test machine is given in Figure 2.4a. With a width to height aspect ratio of 10 in the gauge section of the specimen and the constraint effect of the grips, the strain along the *x*-direction in the center of the gauge section during deformation was approximately zero. In this plane strain condition, only strains in the vertical (*y*) and thickness (*z*) directions were nonzero. Additionally, since the test specimens were thin, the stress in the thickness direction was negligible at the macroscale; therefore, the gauge region was also under plane stress with only nonzero stresses in the width (*x*) and vertical (*y*) directions. For details on the design of the specimen geometry we refer the reader to [9].

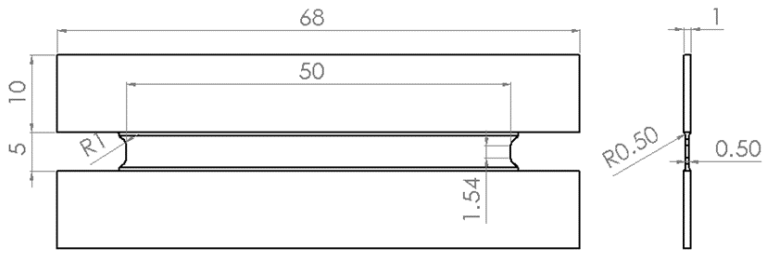

Figure 2.3: Specimen geometry for multiaxial plasticity loading modified from [9]. All dimensions are in mm.

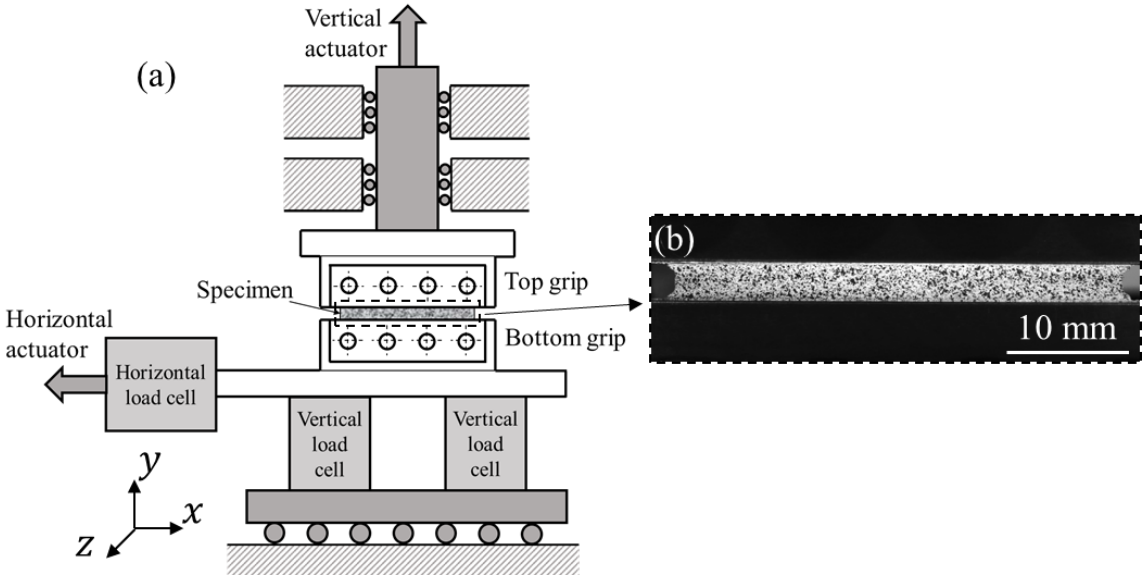

Figure 2.4: (a) Schematic of the dual-actuator hydraulic test frame, which can independently apply vertical (*y*-) and horizontal (*x*-) loads to the specimen gripped in the middle. (b) Gauge section of a test specimen in Figure 2.3 installed in the test frame grips and painted for DIC analysis.

As shown in Figure 2.4a, the testing machine consists of two perpendicular actuators, which can independently apply a vertical (normal) force, F_y, and a horizontal (shear) force, F_x, to the specimen clamped between them. By varying the ratio of F_y/F_x, the dual-actuator system can apply multiaxial stress states ranging from plane strain tension

to pure shear to the test specimen in Figure 2.3. If expressing this ratio as the tangent of an angle β,

$$\tan\beta = \frac{F_y}{F_x} \qquad \text{Eq. 2.1}$$

$\beta = 90°$ corresponds to plane strain tension while $\beta = 0°$ corresponds to pure shear. For each orientation, specimens were tested using four different β values: 0°, 30°, 60° and 90°. Tests with $\beta = 0°$ and 90° were performed under displacement control, while the other two configurations were performed under force control to maintain proportional stress loading.

For all loading conditions except plane strain tension, test specimens (Figure 2.3) were extracted from the DP600 sheets in three directions (α=0°, 45° and 90°, where α denotes the angle between normal force and the rolling direction) to examine the in-plane orientation dependence of the macroscopic plasticity behavior. In plane strain tension only $\alpha = 0°$ was tested. Two digital cameras were used to record the surface deformation of the specimens during loading: one in front to capture overall deformation fields of the entire gauge section, and one in the back to capture the local deformation in the center of each specimen. An example of the images taken by the front camera is shown in Figure 2.4b. Two tests were performed for each orientation and loading configuration.

2.4. Micromechanical modeling

Understanding the influence of microstructures on the mechanical properties under different stress states can be used to enhance the transferability and predictability of plasticity models. The macroscopic experiments described above provide information

about the macroscopic multiaxial plasticity of the material, but do not directly provide information about the underlying deformation mechanisms. Empirical or phenomenological continuum plasticity models have poor transferability from one material to another because microstructural information is neglected. In the current study, RVE models based on the experimentally observed microstructures were used to gain insight into the effect of the microstructure on the macroscopic plasticity behavior.

2.4.1. RVE model[2]

In order to compare observed 2D images of microstructures with the resulting mechanical properties, the samples were modeled using 2D elements in ABAQUS [64]. While the plane stress condition is satisfied at the macroscale, the approximation of plane stress at the microscale needs additional consideration. In particular, the microstructure inhomogeneity in multiphase materials may induce out-of-plane stresses locally that cannot be accounted for by plane stress elements, which assume zero out-of-plane stress at every material point.

The plane stress assumption should be regarded as true only on an average sense for microscale models. This can be achieved by using generalized plane strain elements in ABAQUS. Generalized plane strain elements in ABAQUS use a reference point to control the out-of-plane behavior [64]. By constraining the out-of-plane rotation while leaving the out-of-plane movement free, the stress state in the generalized plane strain model will be,

[2] The work in this section includes contributions from R. McLendon and V. Oancea.

on average, plane stress, but at each individual node, there can be non-zero through-thickness stress. In RVE models for DP steels, the ferrite and martensite phases can be assigned to either the same reference point or two different reference points. When they are assigned to the same reference point, the average plane stress state is met for the entire model, and the two phases will have the same out-of-plane normal strain. Conversely, when they are assigned to two different reference points, the average plane stress state is not only true for the whole model, but also true for each individual phase, and the out-of-plane normal strain will be different for the two phases.

In the current work, the 2D RVE results are being compared to experimental data obtained from finite-thickness specimens. Because no load was applied out-of-plane, the specimen will exhibit plane stress in an average sense at all locations through its thickness, as discussed above. At the free surface, equilibrium requires that plane stress be perfectly satisfied. Internally, however, the kinematic constraints between phases will give rise to local out-of-plane stresses that average to zero across the specimen. Therefore, the 2D model that is most representative of the varied conditions in the 3D specimen is one that possesses a state of average plane stress, and that lies between being pure plane stress (i.e., each element is plane stress) and strictly average plane stress (i.e., a uniform out-of-plane strain across the entire specimen yielding zero averaged out-of-plane stress). In this scenario, constraining the out-of-plane strain in a given phase to be uniform independent of the other phases yields the best approximation to the actual state in the full 3D specimen. Zhou et al. [65] also showed that generalized plane strain elements best represented the behavior of thin DP steel sheets through comparing simulation results using continuum plane stress (CPS) elements, continuum plane strain (CPE) elements, and continuum

generalized plane strain (CPEG) elements; however, they did not specify if in their simulations the phases were constrained to the same reference point or different reference points.

Software that enable semi-automated construction of 2D RVE models based on input images, including OOF2 (Object-Oriented Finite element analysis 2, developed at NIST, [66,67]) and Simpleware (developed by Synopsys, [68]) can generate finite element meshes based on metallographic images, in which the meshes in different phase regions can be assigned different material properties. However, typically, the generated meshes have non-physical stepped boundaries at phase interfaces, causing artificial stress concentrations at these locations. In addition, the generated meshes typically contain triangular elements, which are often artificially stiffer than their rectangular counterparts. In the present study, we reconstructed the microstructure directly in ABAQUS [64] using spline curves to ensure smooth phase boundaries. This also makes it possible to discretize the microstructures with only quadrilateral elements.

In order to determine an appropriate size for the RVE, RVEs ranging from $10\ \mu m \times 10\ \mu m$ to $80\ \mu m \times 80\ \mu m$ were constructed in ABAQUS 2016 [64]. The martensite area fraction in each RVE model considered was $22 \pm 0.5\%$, which is within the range observed experimentally ($22 \pm 3\%$) across an area of $\sim 0.1\ mm^2$. Figure 2.5a shows that, for a constant area fraction of martensite, the simulated macroscopic flow curves converged when the models were $40\ \mu m \times 40\ \mu m$ or larger, indicating that models above this size can be considered sufficiently representative to reproduce the continuum behavior.

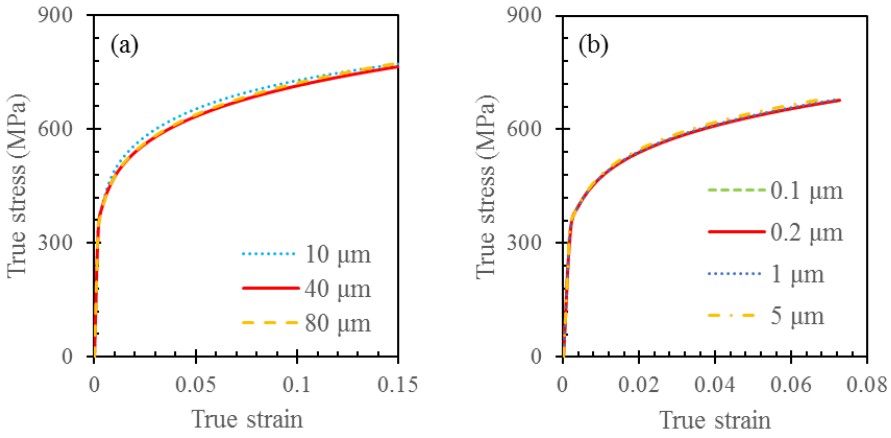

Figure 2.5: True stress-strain curves for DP600 from RVE simulations for the same martensite area fraction (22± 0.5%) to investigate the sensitivity of the results to the RVE size and mesh size. (a) RVE size sensitivity: the physical size of the models ranged from $10 \times 10\ \mu m^2$ to $80 \times 80\ \mu m^2$. (b) Mesh size sensitivity: the 40 μm × 40 μm model with different mesh sizes (shown in Figure 2.6). The 40 μm × 40 μm model with 0.2 μm mesh was adopted for subsequent analysis.

To ensure mesh size independence of the results, the 40×40 μm model was discretized with four different mesh sizes: 0.1 μm, 0.2 μm, 1 μm, and 5 μm, with refined meshes near the martensite/ferrite interfaces, as illustrated in Figure 2.6. The simulated true stress-strain curves for the different mesh sizes are shown in Figure 2.5b. The good agreement in the figure indicates that the simulation results were indeed mesh independent within the bounds tested. However, as shown in Figure 2.6, the shapes of the martensite particles were poorly approximated when the mesh size was 1 μm and 5 μm. To ensure a sufficiently fine mesh at the interfaces while maintaining simulation efficiency, the 0.2 μm

mesh was adopted for subsequent simulations. For this mesh size, there were a total of 60,743 (CPEG4) elements.

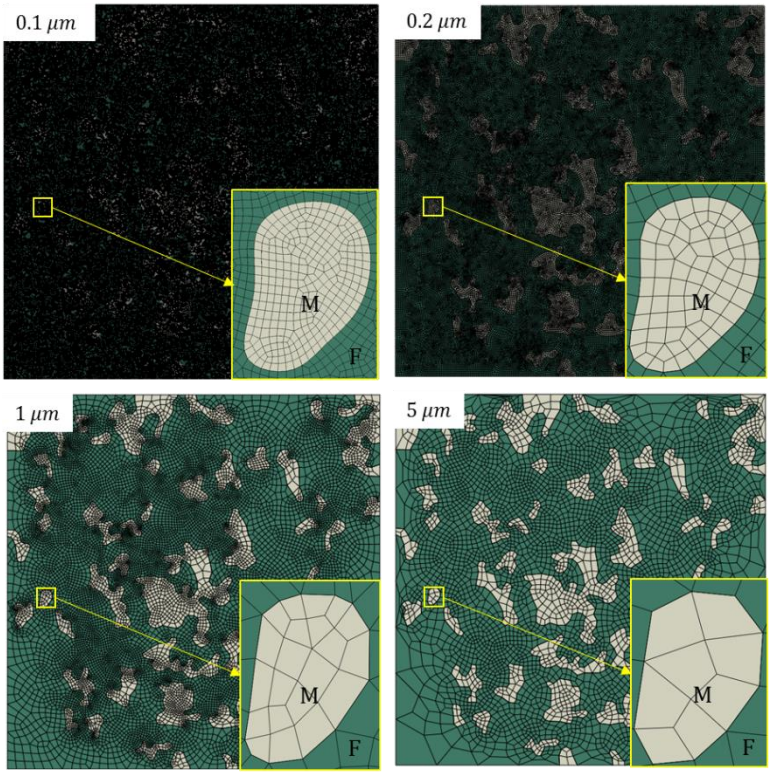

Figure 2.6: RVE models with different approximate mesh sizes (noted in upper left corner). In each model, the mesh size near the phase boundaries was automatically refined to better approach the microstructures. In the figure, "M" and "F" denote martensite and ferrite, respectively.

For the elasto-plastic constitutive behavior of the individual phases, the results by Madej et al. [39] were adopted in the present study, as micro-pillar compression provides direct data on the properties of the individual phases. However, the ferrite curve was adjusted to 80% of the ferrite flow stress in [39] as shown in Figure 1.1a to fit the

macroscopic uniaxial tension data in the present work. Note that with this adjustment, the mechanical properties adopted here still fall within the wide range of ferrite properties reported in the literature. In addition, the adopted constitutive behavior for both phases are very close to the calculations of the same material by Ramazani et al. [69], who predicted the mechanical properties with a dislocation-based strain hardening model. The curves for both phases were fitted with a Swift law to obtain the stress-strain relation beyond the experimental range. Classical J2 plasticity with isotropic hardening was assumed for both phases.

2.4.2. RVE under multiaxial loading

In order to investigate the microstructural level responses as a function of stress state, the RVE model was subjected to four different loading conditions, with each corresponding to an experimentally performed macroscopic test. The definition of stress state is presented in Section 1.4. Using these definitions, the macroscopic stress states for the five tests performed in the present study are summarized in Table 2.1.

Table 2.1: Stress state at the center of test specimens under different loading conditions.

	Uniaxial tension	**Plane strain tension**	**Combined loading, $\boldsymbol{\beta = 60\,^\circ}$**	**Combined loading, $\boldsymbol{\beta = 30\,^\circ}$**	**Pure shear**
$\boldsymbol{\eta}$	0.33	0.58	0.38	0.16	0
$\boldsymbol{\bar{\theta}}$	1	0	0.85	0.46	0

Uniaxial tension was simulated in the RVE model by constraining the vertical movement of the bottom boundary, applying a uniform vertical displacement to the top

boundary, and constraining the left and right boundaries to remain vertical but free to move in the horizontal direction. For plane strain tension, the top and bottom boundaries were subjected to the same boundary conditions as uniaxial tension, but the horizontal displacements of the left and right boundaries were constrained to be zero.

For loading conditions involving shear, normal stresses were applied along principal stress directions, instead of applying shear and normal stresses to the RVE boundaries directly. This is because the rotation of the boundaries with finite deformation requires the addition of normal stresses to ensure a pure shear stress state in the volume. For more detailed discussions, the readers are referred to [70,71]. Therefore, for pure shear and the combined tension/shear loading conditions, the vertical displacement of the bottom boundary and the horizontal displacement of the left boundary were constrained, while two normal tractions, with ratios of -1, -2.5, and $\frac{23+\sqrt{513}}{4}$, were applied to the top and right boundaries for pure shear, combined loading with $\beta = 30°$, and combined loading with $\beta = 60°$, respectively. To keep the ratios constant under finite deformation, distributed surface loads, which apply tractions based on the current deformed area of the surface instead of total forces, were applied to the boundaries in ABAQUS.

Lastly, perfect bonding was assumed at the interface between ferrite and martensite; thus, these simulations did not allow for separation between phases. Ferrite grains were not modeled explicitly, but rather, the microstructure was assumed to consist of a homogeneous ferrite matrix with dispersed martensite particles.

2.5. Results and discussion

2.5.1. Uniaxial tension tests

The macroscopic elastic modulus, *E*, of the DP600 steel was measured experimentally to be 201 GPa. The average yield strength (0.1% offset) was found to be 393 ± 6 MPa. The average macroscopic fracture strain under uniaxial tension was 0.24 ± 0.01.

Von Mises equivalent stress-equivalent plastic strain curves for DP600 under uniaxial tension are shown in Figure 2.7a. The data for tension in the three in-plane directions are similar; thus, the material can be approximated as being in-plane isotropic at the macroscale. As shown in Figure 2.7a, the flow behavior of the material was fitted with a Swift law ($\sigma_y = A(\varepsilon_0 + \bar{\varepsilon}^p)^n$, [72]) before necking ($\bar{\varepsilon}^p \leq 0.14$), with linear hardening behavior after necking ($\bar{\varepsilon}^p > 0.14$) given as:

$$\dot{\sigma}_y = \begin{cases} nA(\varepsilon_0 + \bar{\varepsilon}^p)^{n-1}\,\dot{\bar{\varepsilon}}^p & \bar{\varepsilon}^p \leq 0.14 \\ K\dot{\bar{\varepsilon}}^p & \bar{\varepsilon}^p > 0.14 \end{cases} \qquad \text{Eq. 2.2}$$

The slope of the linear portion was determined through an inverse method to reproduce the experimentally measured force-displacement curve in Figure 2.7b. The calibrated parameters are given in Table 2.2. For the continuum modeling, we take Eq. 2.2 as the equivalent stress-strain relationship in an isotropic J2 plasticity framework [73].

2.5.2. Multiaxial loading tests

The force-displacement curves for the multiaxial plasticity tests are shown in Figure 2.8a and Figure 2.8b. The force-displacement behavior for plasticity tests with the same β

value, but different α values, had a maximum force difference of 6% between tests, further supporting the assumption of in-plane isotropy.

The multiaxial loading tests were also simulated at the continuum level using the model described in Section 2.5.3. In these simulations, half of the specimen along the through-thickness direction was modeled in ABAQUS [64] in a three-dimensional fashion. A total of 16,000 C3D8R elements were used to discretize this half-thickness model.

Table 2.2: Model parameters describing the Swift law strain hardening behavior of DP600.

A	ε_0	n	K
1056 MPa	0.002	0.16	730 MPa

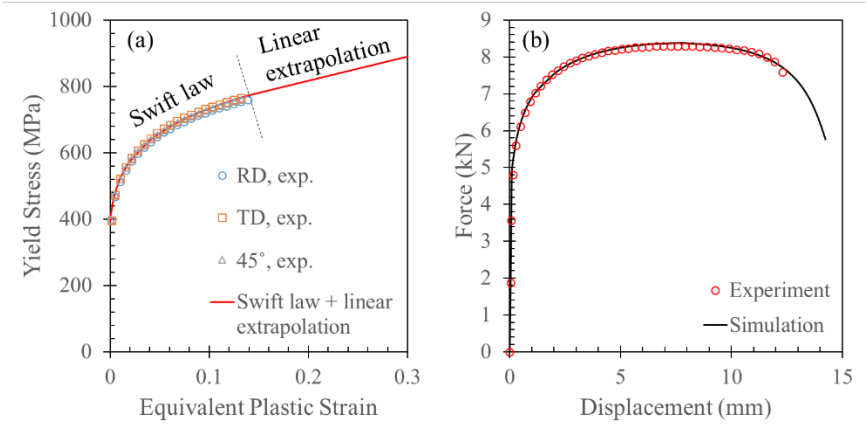

Figure 2.7: (a) DP600 strain hardening curves obtained from uniaxial tension tests (symbols) on specimens extracted from three material orientations, showing no in-plane anisotropy. These data were fitted with a Swift law hardening equation before necking and a linear extrapolation after necking. (b) Force versus displacement curves for uniaxial tension comparing experimental data (symbols) and the corresponding continuum simulation (line) using the fitted and extrapolated curve in (a).

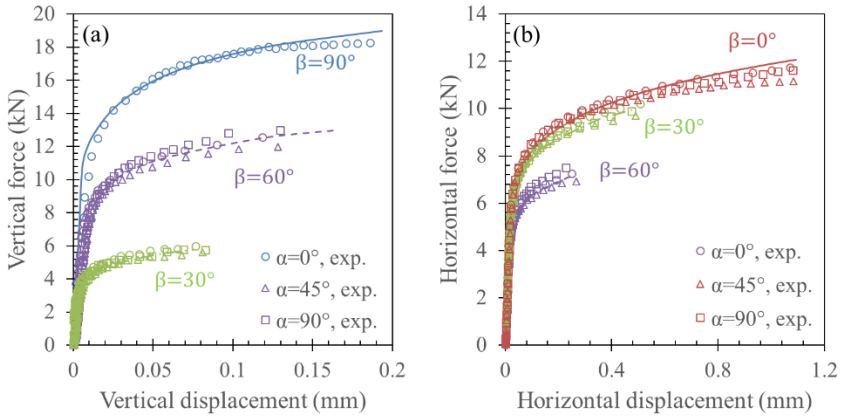

Figure 2.8: Vertical (a) and horizontal (b) force versus displacement curves for four multiaxial loading conditions with different β values (0°, which has only nonzero horizontal force, 30°, 60°, and 90°, which has only nonzero vertical force) showing the comparison between experimental data (symbols) and continuum simulation results (lines).

2.5.3. Plasticity model

The von Mises yield criterion was adopted to describe the continuum plasticity behavior, where the von Mises equivalent stress under plane stress is given as:

$$\bar{\sigma}_{vM} = \sqrt{\sigma_0^2 - \sigma_0\sigma_{90} + \sigma_{90}^2 + 3\tau^2} \qquad \text{Eq. 2.3}$$

where σ_0 and σ_{90} are the normal stresses along the RD and TD, respectively, and τ is the in-plane shear stress.

Figure 2.9 shows the experimental data plotted on the von Mises yield surface, indicating that this yield surface describes well the initial multiaxial yield behavior of the material.

The yield function, $\Phi(\sigma_{ij})$, is therefore given as:

$$\Phi(\sigma_{ij}) = \bar{\sigma}_{vM} - \sigma_y = 0 \qquad \text{Eq. 2.4}$$

where σ_y is the flow stress. The evolution of the flow stress, or strain hardening behavior is described by equation (4).

Finally, the flow rule is given as:

$$\dot{\varepsilon}_{ij}^{p} = \dot{\gamma} \frac{\partial \Psi(\sigma_{ij})}{\partial \sigma_{ij}} \qquad \text{Eq. 2.5}$$

where $\dot{\gamma}$ is the plastic multiplier and $\Psi(\sigma_{ij})$ is the flow potential. We adopt the associated flow rule, meaning $\Psi(\sigma_{ij}) = \Phi(\sigma_{ij})$.

This continuum plasticity framework was implemented in ABAQUS, and the results of macroscopic simulations of the uniaxial tension and multiaxial loading tests are given in Figure 2.7b, Figure 2.8a and Figure 2.8b, respectively. As this model was developed and calibrated with only uniaxial tension data, the simulations of multiaxial deformation serve as a partial validation of the plasticity model.

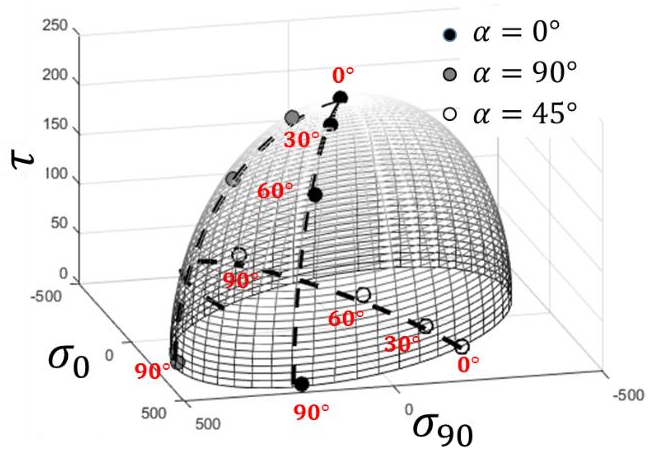

Figure 2.9: 3D representation of a von Mises yield surface under plane stress with experimentally-measured yield points shown as symbols. The angles on the surface indicate β values.

2.5.4. RVE simulations

One of the primary goals of the current work is to determine if the macroscopic stress-strain responses of the material under different stress states can be described and predicted from RVE simulations of the microstructural response. The boundary conditions for uniaxial tension and plane strain tension in the RVE simulations were the same as those described in Section 2.4.2. Pure shear and combined loadings were achieved by applying principal stresses, as illustrated in Figure 2.10a. Thus, the machine coordinates, which include the direction along which the normal strain should be zero (*x*-direction), are at an angle θ from the principal stress coordinate system as shown in Figure 2.10a. This angle is 45° for pure shear, 41° for combined loading with $\beta = 30°$, and 33° for combined loading with $\beta = 60°$. Figure 2.10b shows the normal strains along the *x*-direction for the three loading conditions as a function of the RVE volume average equivalent plastic strain. The values of ε_{xx} are two orders of magnitude smaller than the equivalent plastic strain, indicating negligible horizontal strains with the applied stress ratios, which is in good agreement with the experimentally imposed plane strain condition.

As stated above, only uniaxial tension results were used to calibrate the flow stress of the ferrite phase. The RVE simulated equivalent stress-plastic strain curve after calibration for uniaxial tension is shown in Figure 2.11a. To examine the RVE model's ability to describe macroscopic multiaxial plasticity behavior, and to inspect the simulated stress state dependent microstructural responses, the RVE model was subjected to plane strain tension, pure shear, and combined loading with β = 30° and β=60°. Comparisons of simulated and experimentally obtained von Mises equivalent stress-equivalent plastic

strain curves for multiaxial loading are given in Figure 2.11b-e, which show good agreement between microscopic simulations and macroscopic experiments.

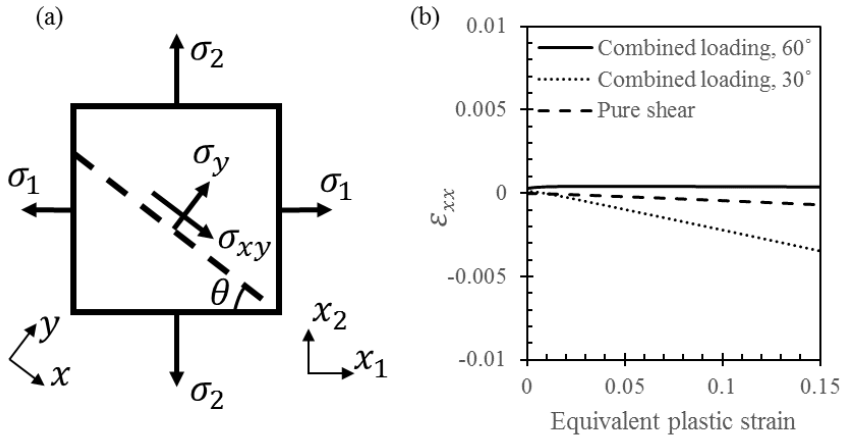

Figure 2.10: (a) Applied principal stresses for pure shear and combined loadings in the x_1 and x_2 directions, along with the x-y (machine coordinate) plane in which plane strain should be fulfilled along the *x*-direction. The angle between the machine coordinates and the principal stress coordinates is θ. (b) Normal strain along the *x*-direction as a function of RVE volume average equivalent plastic strain for different applied stress states achieved through applied stress boundary conditions.

A significant benefit of RVE modeling is the ability to investigate the predicted local deformation fields that lead to localization and damage accumulation under different stress states. The strain fields within the RVE at a macroscopically applied equivalent plastic strain of 7% for each stress state studied are shown in Figure 2.12. Under each loading condition studied (uniaxial tension, plane strain tension, pure shear, and combined loading with $\beta = 30°$ and $\beta = 60°$) ferrite between closely situated martensite particles developed the highest local strains in the RVE. This result corresponds to experimental

data in the literature [23,24]. Figure 2.12 shows that when the applied equivalent plastic strain was 7%, no shear band was developed in plane strain tension, but as shear loading was introduced, shear bands developed, and with increasing shear loading, the shear bands became more prominent. The shear bands connect the highly localized deformation in ferrite between closely situated martensite particles, indicating that the arrangement of the martensite particles impacts significantly the overall localization behavior.

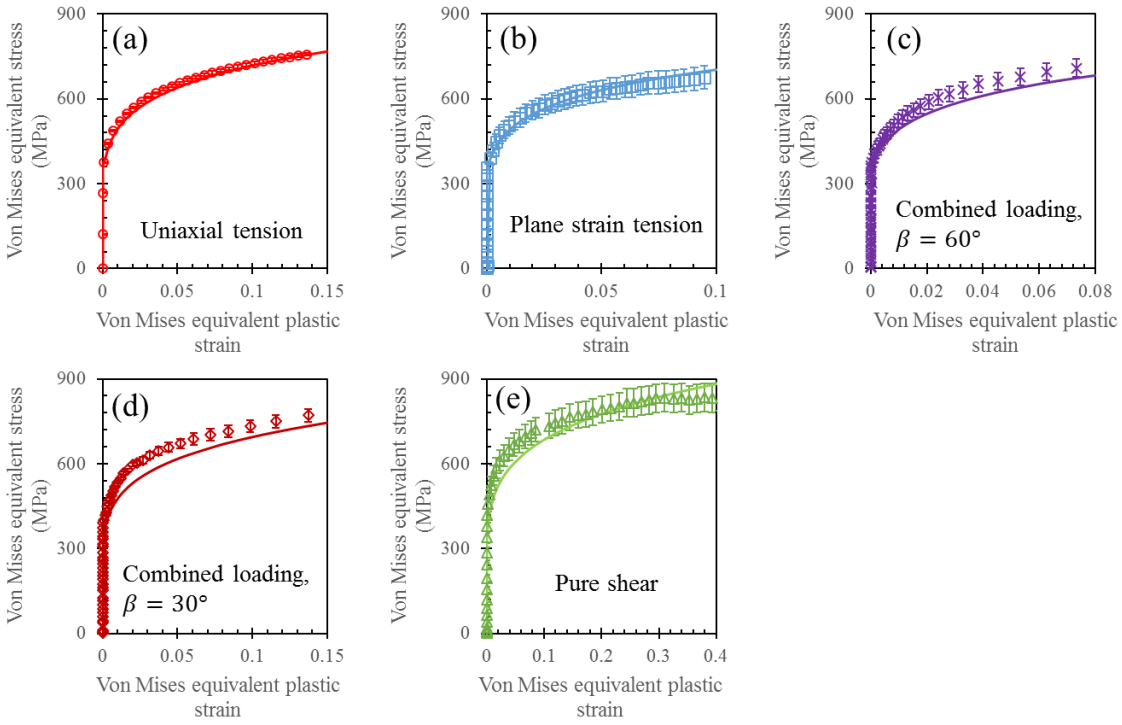

Figure 2.11: Comparison of von Mises equivalent stress-equivalent plastic strain curves for (a) uniaxial tension and (b-e) multiaxial experiments (symbols) and RVE simulations (lines).

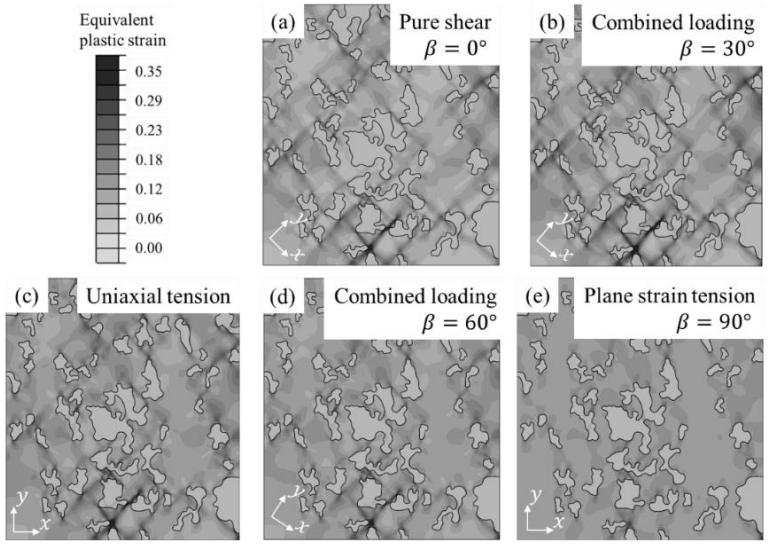

Figure 2.12: Equivalent plastic strain fields in the RVE model at a macroscopically applied equivalent plastic strain of 7% under (a) pure shear, (b) combined loading with $\beta = 30°$, (c) uniaxial tension, (d) combined loading with $\beta = 60°$, and (e) plane strain tension. The *x*-*y* coordinates in the figures correspond to the machine coordinates (Figure 2.4 and Figure 2.10), where the zero-strain condition is met along the x-direction.

Due to the significant difference in the constitutive behavior of the two phases, plastic deformation in DP steels typically localizes in the soft ferrite matrix, while the hard martensite particles remain elastic [29,74]. *In situ* neutron diffraction tests performed on a DP steel with ~ 50 vol% martensite, showed that martensite remained elastic until specimen necking began [74]. In uniaxial tension of DP steels with almost constant martensite content (29.8 vol% to 31.3 vol%) but varying grain sizes, Calcagnotto et al. found that when the ferrite grain size was ~ 12 μm, the martensite phase remained elastic after sample necking [29]. The simulation results in Figure 2.12 reproduced the phenomenon that under

macroscopic plastic deformation, ferrite undergoes plastic deformation while martensite remains elastic.

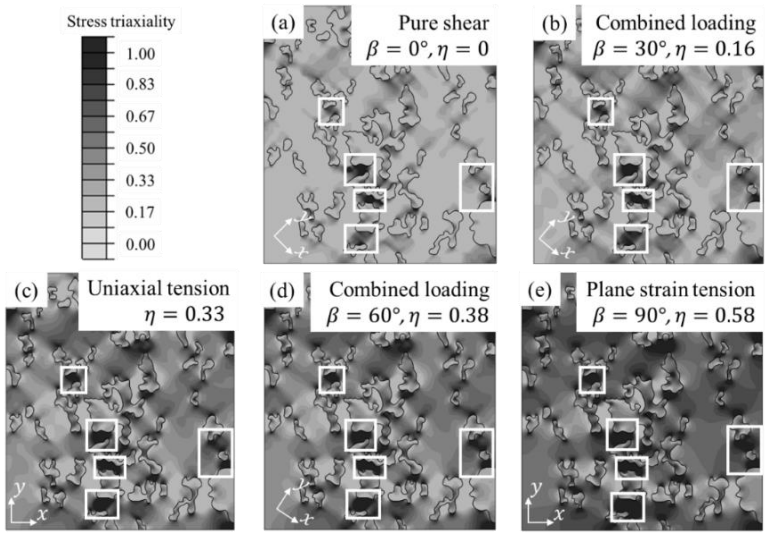

Figure 2.13: Stress triaxiality field, at a macroscopically applied equivalent plastic strain of 7%, in the RVE model under (a) pure shear, (b) combined loading with $\beta = 30°$, (c) uniaxial tension, (d) combined loading with $\beta = 60°$, and (e) plane strain tension. Black lines depict the outline of martensite in the RVE, and white rectangles mark high local stress triaxiality sites. The *x*-*y* coordinates in the figures correspond to the machine coordinates (Figure 2.4 and Figure 2.10), where the zero-strain condition is met along the x-direction.

Figure 2.13 and Figure 2.14 show the stress triaxiality and Lode angle parameter fields at a constant applied equivalent plastic strain under different loading conditions. On average, the stress triaxiality and Lode angle parameter in both ferrite and martensite increased with macroscopically applied stress triaxiality and Lode angle parameter, respectively. Under the loading conditions studied, the presence of martensite particles

changed the local stress triaxiality in the ferrite matrix. The stress triaxiality is locally higher in ferrite between closely situated martensite particles than regions without martensite as shown in Figure 2.13, similar to the plastic strain localization. However, the Lode angle parameter is increased between closely spaced martensite only under plane strain tension, while the presence of martensite does not notably affect the Lode angle parameter values in pure shear. While the Lode angle parameter field was affected by the martensite particles in the remaining three loading conditions, there was no notable trend in the location of the maximum or minimum Lode angle parameter values.

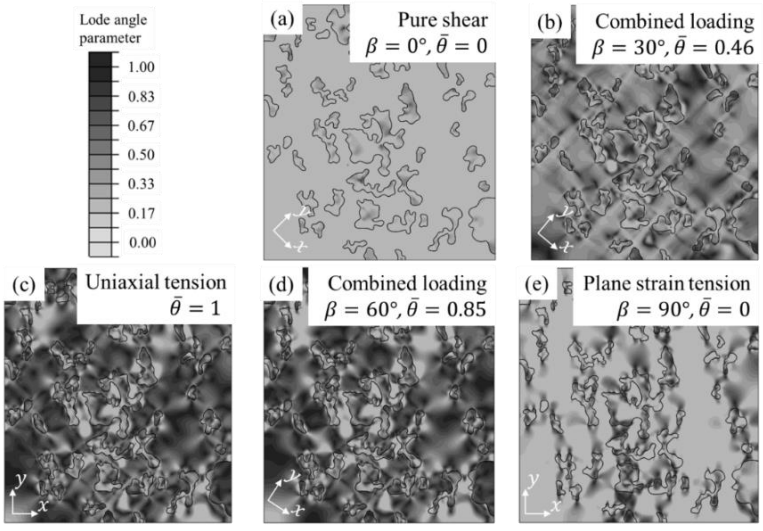

Figure 2.14: Lode angle parameter field, at a macroscopically applied equivalent plastic strain of 7%, in the RVE model under (a) pure shear, (b) combined loading with $\beta = 30°$, (c) uniaxial tension, (d) combined loading with $\beta = 60°$, and (e) plane strain tension. Black lines depict the outline of martensite in the RVE. The *x*-*y* coordinates in the figures correspond to the machine coordinates (Figure 2.4 and Figure 2.10), where the zero-strain condition is met along the x-direction.

Figure 2.12 through Figure 2.14 highlight the complex local deformation and stress state at the microscale due to the presence of martensite particles in DP steel. While closely situated martensite particles significantly increased the local strain and triaxiality in the ferrite between them with respect to the ferrite matrix, there was no clear trend in Lode angle parameter variations.

2.6. Summary and conclusions

In the present study, the multiaxial plasticity behavior of DP600 was examined through macroscopic multiaxial plasticity tests, continuum modeling, microstructural evaluation, and micromechanics modeling. The micromechanics modeling allowed for the inspection of deformation localization and local stress state variations in the material. The key conclusions are:

- The constitutive behavior of DP600 was found to be stress-state independent and isotropic in the plane of the sheet as the microstructure was composed of non-textured equiaxed grains. Therefore, a continuum plasticity model composed of an isotropic von Mises yield surface, with an associated flow rule, and a stress-state independent strain hardening law, was able to describe the macroscopic plasticity behavior of current material.
- Microscopic RVE modeling can be used to capture the macroscopic multiaxial mechanical responses of DP600 while also providing information about the intrinsic deformation inhomogeneity between the two phases, enabling the inspection of microstructural deformation mechanisms as well as local stress states.

- During macroscopic plastic loading, the martensite particles deformed elastically, while plastic deformation was limited to the ferrite matrix. Even though the microscopic and macroscopic strain hardening behaviors were defined to be independent of stress state, the sites of microscale localization deformation depended on stress state.
- Closely situated martensite particles concentrated the plastic deformation and stress triaxiality, but did not have a notable impact on the Lode angle parameter except in plane strain tension.

Chapter 3 Multiaxial fracture of DP600: experiments and finite element modeling[3]

3.1. Introduction

The ductile fracture behavior of dual phase (DP) steels has been investigated from both the macroscale [16,75,76] and the microscale [17–22]. Studies at the macroscale have focused on determining the continuum-level stress state dependent fracture behavior of DP steels, studies at the microscale have focused on understanding local fracture mechanisms and/or simulating the fracture behavior at the microscale, primarily under uniaxial tension. By performing experiments and finite element simulations over a wide range of stress states, this chapter aims to quantify the fracture behavior of DP600 at the continuum level and describe the multiaxial fracture behavior with an appropriately calibrated fracture model.

In the literature, the stress state dependent fracture behavior of DP600 has been investigated by Lian et al. [15] and Habibi et al. [16]. However, the stress triaxiality ranges probed in these papers were $0 < \eta < 0.58$ in ref. [15] and $0.33 < \eta < 0.67$ in ref. [16]. In this chapter, the fracture behavior of DP600 was investigated over a wide range of stress states through both experiments and computational simulations. To probe the fracture behavior under different stress states, several disparate specimen geometries were fabricated and subjected to mechanical loading, resulting in the probing of fracture

[3] Reproduced from: Qin, S. and Beese, A.M., 2020. Multiaxial fracture of DP600: through mechanical testing experiments and finite element modeling. *Submitted*.

behavior over a range of stress triaxiality values from 0 to 0.67 and a range of Lode angle parameter values from -1 to 1. The modified Mohr-Coulomb model was calibrated using experimental data in order to describe the fracture behavior at macroscopic scale, and the calibrated MMC model was compared to a MMC fracture locus reported previously in literature for DP600 [16]. The comparison revealed a notable difference in the two calibrated fracture models for the low stress triaxiality values, where the previously reported locus was unable to capture the newly presented experimental data, highlighting the importance of calibrating fracture models using a wide range of stress states to fully capture multiaxial ductile fracture behavior.

3.2. Experimental methods

3.2.1. Material and its strain hardening behavior

Here, rolled DP600 sheet with a thickness of 1.6 mm was studied. Uniaxial tension tests on samples with the geometry shown in Figure 3.1a were performed on two samples cut with their tensile axes along the rolling direction, since previous studies have shown the plasticity behavior of DP600 to be isotropic [18,32]. Tests were performed at a strain rate on the order of 10^{-4} s^{-1}. The tests were repeatable, with the experimentally measured engineering stress strain curves shown in Figure 3.1b. The strain hardening behavior of the material can be described with a Swift law prior to necking, with a linear extrapolation after necking:

$$\begin{cases} \sigma_y = A(\varepsilon_0 + \bar{\varepsilon}^p)^n, \bar{\varepsilon}^p < \bar{\varepsilon}^p_{necking} \\ \dot{\sigma}_y = K\dot{\varepsilon}^p, \bar{\varepsilon}^p > \bar{\varepsilon}^p_{necking} \end{cases} \quad \text{Eq. 3.1}$$

where $\bar{\varepsilon}^p$ is equivalent plastic strain, $\bar{\varepsilon}^p_{necking}$ is the $\bar{\varepsilon}^p$ at the maximum engineering stress, and σ_y is yield stress. Experimental results showed that $\bar{\varepsilon}^p_{necking} = 0.15$. The Swift law parameters ($A = 1004$ MPa ,$\varepsilon_0 = 0.002$, and $n = 0.16$) were determined by fitting the strain hardening curves determined from the uniaxial tension tests, and the linear extrapolation coefficient ($K = 694$ MPa) was determined using the inverse method described in [32]. The corresponding true stress-strain curve is shown in Figure 3.1b. Finite element simulations using the above strain hardening behavior produced a simulated engineering stress strain curve that accurately matched the experimental data as also shown in Figure 3.1b.

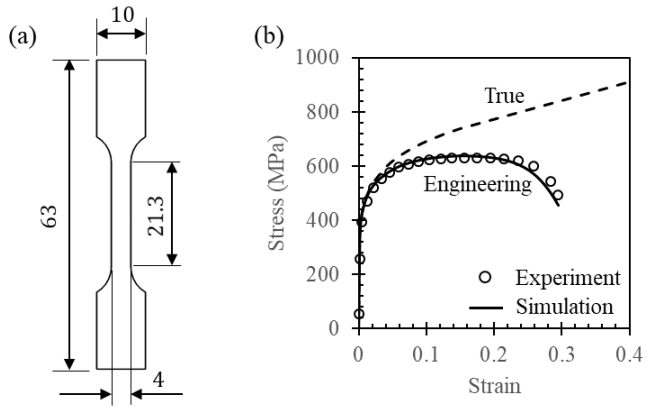

Figure 3.1: (a) Flat specimen geometry used in uniaxial tension tests (all dimensions in mm), for which the thickness was 1.6 mm. (b) Engineering stress strain curves measured experimentally (symbols) and produced through finite element simulations (solid line), as well as the true stress strain curve determined from the Swift law (strain < 0.15) plus linear extrapolation (strain > 0.15).

3.2.2. Fracture tests

To determine the fracture strain of the DP600 material under different stress states, the following specimen geometries were used: tension with a central hole (CH), butterfly, punch, and three notched tension (NT) specimens with different notch radii, all shown in Figure 3.2. Due to the isotropy of the material, the CH, butterfly, and NT specimens were manufactured with their tensile loading axes along the rolling direction. Mechanical tests performed on these specimens result in inhomogeneous strain fields; therefore, the locations of highest strain during deformation are assumed to be the locations of fracture initiation, or the 'critical point' for failure, as indicated in Figure 3.2. Note that all critical points are in the center of the thickness of the sample except for in the punch specimen, where the critical point is on the top surface.

In the present study, the CH specimens (Figure 3.2a) were subjected to uniaxial tension loading at a loading rate of 0.2 mm/min. This specimen is designed so that its critical point is under uniaxial tension ($\eta = 0.33$, $\bar{\theta} = 1$) up to failure.

The butterfly specimen (Figure 3.2b) has a very high aspect ratio in the gauge section, creating a transverse plane strain stress state at the specimen center. At the same time, it is also under plane stress due to its thin thickness (0.5 mm). More details about the design of the specimen can be found in Dunand and Mohr [11]. The specimen can be subjected to pure tension loading, pure shear loading, or any combination of tension/shear loading. To describe different load cases, a virtual angle β is defined so that $\tan\beta = F_V/F_H$, where F_V is the normal loading force and F_H is the horizontal loading force. In the current study, tests with four different β values (0°, 30°, 70°, and 90°) were performed. Note that $\beta = 90°$ corresponds to plane strain tension ($\eta = 0.58$, $\bar{\theta} = 0$), while $\beta = 0°$

corresponds to pure shear ($\eta = 0, \bar{\theta} = 0$). All tests were performed with the custom-made dual actuator hydraulic test machine (MTS Systems Corp.) at the Pennsylvania State University, whose schematic is shown in Qin et al. [32]. The tests with $\beta = 90°$ and $\beta = 0°$ were performed under displacement control, with a loading rate of 0.1 mm/min for $\beta = 90°$ and 0.4 mm/min for $\beta = 0°$. The rest of the tests were performed under force control, with $\dot{F}_V = 1.5\ \text{kN/min}$ and $\dot{F}_H = 0.546\ \text{kN/min}$ for $\beta = 70°$, and $\dot{F}_V = 0.864\ \text{kN/min}$ and $\dot{F}_H = 1.5\ \text{kN/min}$ for $\beta = 30°$, where $\dot{F}_V$ is the vertical loading rate and $\dot{F}_H$ is the horizontal loading rate.

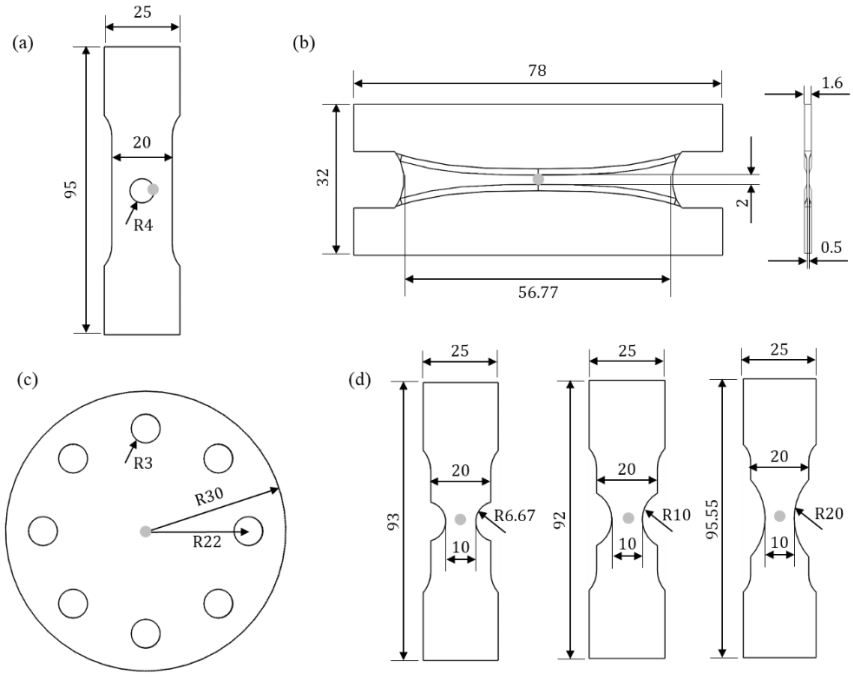

Figure 3.2: Specimen geometries for (a) central hole tension, (b) butterfly, (c) punch, and (d) notched tension tests. All dimensions in mm, with through-page thicknesses of 1.6 mm. Dots in the figures mark the locations of highest strain during deformation (i.e., critical points) within the specimens.

The punch specimen (Figure 3.2c) was loaded with a punch fixture, resulting in an equi-biaxial tension ($\eta = 0.67, \bar{\theta} = -1$) stress state at its critical point. The punch fixture features a top die with a 25.4 mm diameter through hole at the center and a bottom punch rod with a hemisphere end whose radius is 12.7 mm. The top die holds the punch specimen, while it is pushed onto the punch [76]. In order to minimize the friction between the punch rod and the specimen, two layers of Teflon sheet were applied. The tests were performed at a loading rate of 2 mm/min.

The NT specimens (Figure 3.2d) had three different notch radii: 6.67 mm (R6), 10 mm (R10), and 20 mm (R20), resulting in different stress states at the specimen center. The theoretical relationship between notch radius, sample width, and the initial stress state at the specimen center is given in Bai [77]. Under the plane stress assumption, the stress triaxiality at the specimen center can be expressed as:

$$\eta = \frac{1 + 2\Lambda}{3\sqrt{\Lambda^2 + \Lambda + 1}} \qquad \text{Eq. 3.2}$$

where $\Lambda = \ln(1 + a/2R)$, with R being the notch radius, and a being the half specimen width at the notch root. In general, notched tension tests result in stress states between uniaxial tension and plane strain tension. The specimens were subjected to tensile loading at a loading rate of 0.4 mm/min.

In all of the tests, digital image correlation (DIC) was adopted to measure the deformation. Two-dimensional DIC (2D DIC) was adopted for all tests except the punch tests, in which three-dimensional DIC (3D DIC) was used. Before a test, a uniform white coat of paint was applied to the specimen gauge section on top of which a random black speckle paint pattern was applied. Images of the deforming surface were taken during mechanical testing using one camera for 2D DIC and two cameras for 3D DIC (Point Grey

GRAS-50S5M − C) at a frequency of 1 Hz using image capture software (VicSnap, Correlated Solutions). Strains were computed using either the Vic2D or Vic3D software (Correlated Solutions). For the tests analyzed using 2D DIC, the displacement in the respective tests were extracted through a centrally located virtual extensometer, whose length was 30 mm for CH, NT-R6, and NT-R10 specimens, 35 mm for NT-R20 specimens, and 10 mm for butterfly specimens. For punch tests, the displacements were determined to be the relative displacement between the pixel at the specimen center and a pixel that was 6.39 mm away from the center.

3.3. Finite element simulations

3.3.1. Finite element models

Finite element simulations were performed for all of the fracture tests described above. These simulations are used for two key purposes: first, to validate that the strain hardening curve determined in the uniaxial tension tests can be used within the J2 plasticity framework to describe the flow behavior of all samples tested; second, to provide information on variables that are not directly measurable in experiments, like the evolution of stress state and local plastic strain at the critical points for failure.

The commercial finite element software ABAQUS/Standard was adopted for all simulations [78]. To reduce the model size, only one quarter of the in-plane CH, NT, and punch geometries were modeled, with symmetric boundary conditions being implemented on all cut planes, as illustrated in Figure 3.3. In addition, only half of the thickness was modeled for the CH, NT, and butterfly specimens, again with symmetric boundary conditions imposed on cut planes. The grip regions of the CH specimens, NT specimens,

and butterfly specimens were assumed to be rigid. For CH and NT specimens, the load was applied through a uniform upward displacement of the top grip. For simulations of the butterfly specimen, the bottom grip was fixed, while a uniform displacement or two concentrated forces were applied to a reference node in the top grip region, depending on the β angle being simulated. For the punch simulation, the bottom punch rod and the top die were modeled as rigid bodies in ABAQUS (part type: analytical rigid [78]), with frictionless contact between each of these entities and the specimen assumed [76]. All of the circumferential nodes of the specimen and the top die were fixed throughout the simulation, while a uniform displacement was applied to the bottom punch. The von Mises equivalent stress and plastic strain were used in the simulations due to the material being isotropic, and the strain hardening behavior described in Section 3.2.1 was adopted. No damage or fracture model was included in the simulations.

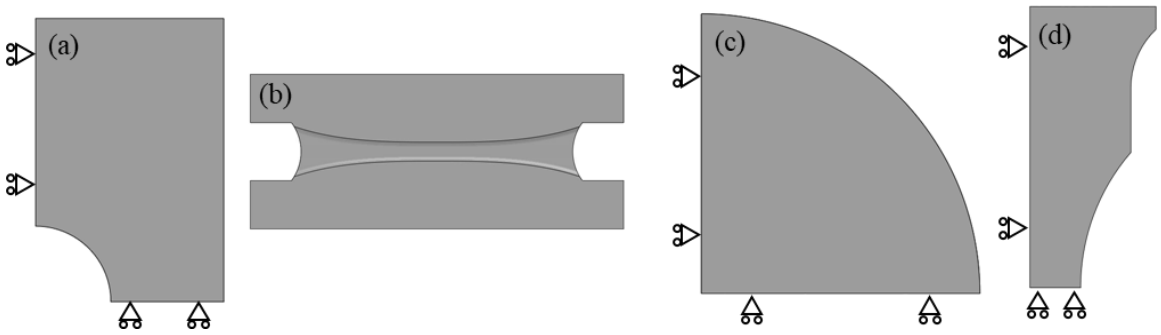

Figure 3.3: The geometries modeled in the finite element simulations for the (a) central hole tension, (b) butterfly, (c) punch, and (d) notched tension tests. The boundaries with symmetry boundary conditions are marked. Note that all specimens were modeled only half thickness except for the punch specimen, whose model has full thickness.

3.3.2. Mesh size dependence study

All of the fracture specimens (CH, NT, butterfly, and punch) were discretized with three-dimensional hexahedron meshes (ABAQUS element type C3D8). To determine an appropriate mesh size, mesh size dependence studies were performed. The gauge center regions of each specimen type were discretized with three different mesh sizes: fine, medium, and coarse meshes. For the CH, NT, and butterfly specimens, this corresponds to 0.05 mm, 0.1 mm, and 0.3 mm, and for the punch specimen, this corresponds to 0.005 mm, 0.01 mm, and 0.1 mm. The meshes gradually coarsened with increasing distance from the critical point to reduce simulation time. The relatively fine mesh adopted for the punch specimen was required due to its higher strain gradient at the center of the sample.

The simulated force displacement curves and evolutions of equivalent plastic strain at the specimen centers with different mesh sizes are shown in Figure 3.4. For all of the simulations, the simulated force and strain did not change for medium size meshes or finer. Therefore, in subsequent studies, a medium mesh size was applied at the gauge center. The resultant number of elements were CH: 59,760; NT-R6: 15,120; NT-R10: 19,800; NT-R20: 21,960; butterfly: 126,176; and punch: 303,600.

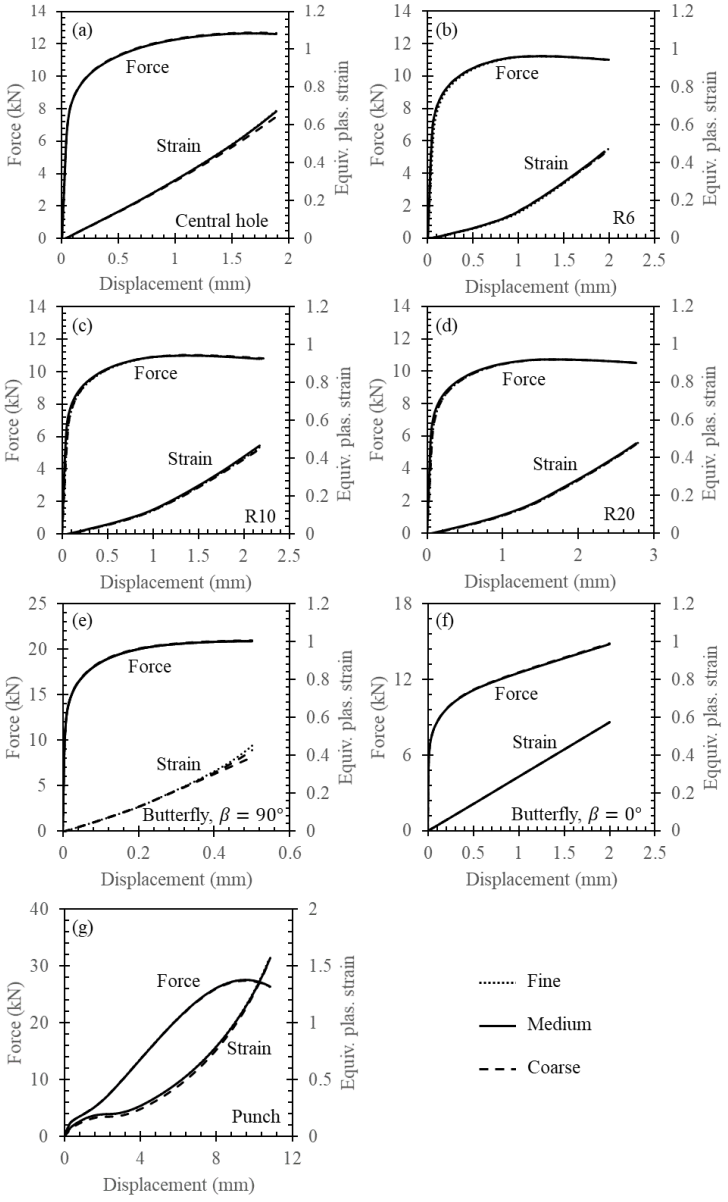

Figure 3.4: Mesh size study for (a) central hole, (b) notched tension with R=6.67 mm, (c) notched tension with R=10 mm, (d) notched tension with R=20 mm, (e) and (f) butterfly, and (g) punch simulations. For the punch test, mesh sizes of 0.005 mm, 0.01 mm, and 0.1 mm were investigated, while for all other simulations, mesh sizes of 0.05 mm, 0.1 mm, and 0.3 mm were investigated.

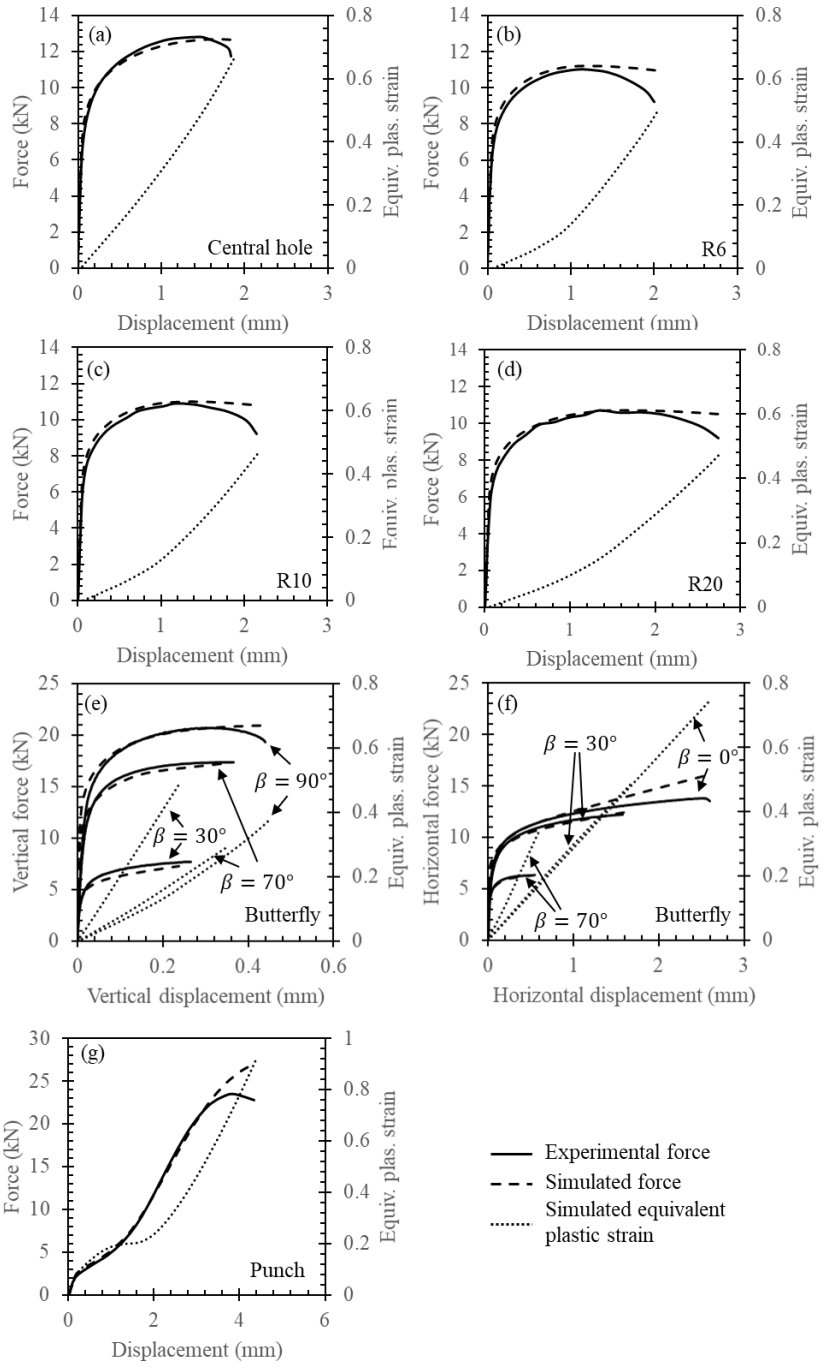

Figure 3.5: Force versus displacement curves obtained from experiments and finite element simulations, and evolution of equivalent plastic strain at the critical point in the (a) central hole, (b,c,d) notched tension, (e,f) butterfly, and (g) punch tests.

3.4. Results and discussion

3.4.1. Experimental and finite element simulation results

The force displacement curves obtained from the fracture tests and the corresponding finite element simulations are shown in Figure 3.5. All simulations agreed reasonably well with experimental data up to large strain regions, at which point damage initiated in the experiments, validating the strain hardening behavior determined above and the adoption of the J2 plasticity model.

The evolutions of the equivalent plastic strain, stress triaxiality, and Lode angle parameter at the critical points of the specimens are shown in Figure 3.5 and Figure 3.6. The symbols in Figure 3.6 show the moment when fracture occurred in experiments, and the corresponding equivalent plastic strain values at the critical points were determined to be the fracture strains ($\bar{\varepsilon}_f$) of the tests. For consistency among similar experiments, fracture was taken to be the moment when the measured force dropped 3% from its maximum in the CH and NT tests, the moment of complete catastrophic failure in the butterfly tests, and the moment of maximum force in the punch tests.

It can be seen that the stress state at the critical point of the CH test remained under uniaxial tension ($\eta = 0.33, \bar{\theta} = 1$) all the way to failure, with only minimal deviations. Similar stability was observed in the butterfly and the punch tests. The average stress triaxiality and Lode angle parameter values for each test were defined:

$$\eta_{avg} = \frac{1}{\bar{\varepsilon}_f} \int_0^{\bar{\varepsilon}_f} \eta \, d\bar{\varepsilon}^p \qquad \text{Eq. 3.3}$$

$$\bar{\theta}_{avg} = \frac{1}{\bar{\varepsilon}_f} \int_0^{\bar{\varepsilon}_f} \bar{\theta}\, d\bar{\varepsilon}^p$$

The resultant average stress triaxiality and average Lode angle parameter are marked as dashed lines in Figure 3.6. Their values, as well as the fracture strains, in all of the tests are summarized in Table 3.1.

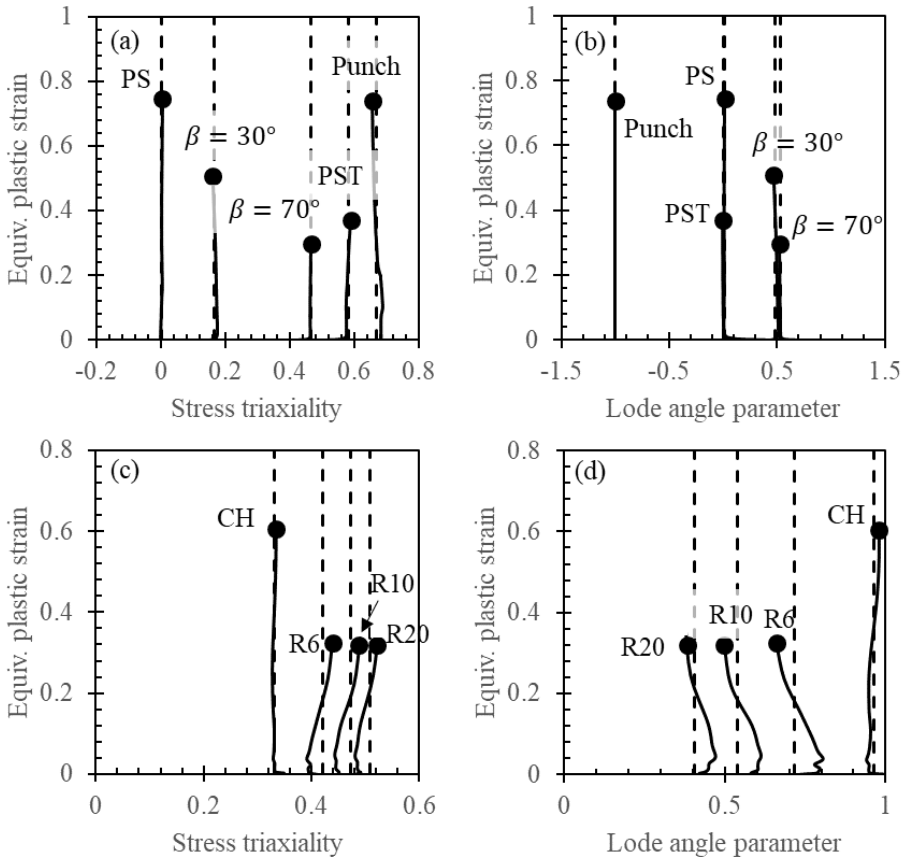

Figure 3.6: Evolution of stress triaxiality and Lode angle parameter at the critical point in (a,b) multiaxial loading and (c,d) uniaxial loading tests. The dashed lines mark the weighted average value in each test (calculated using Eq. 3.3). Data for plane strain tension (PST), pure shear (PS), central hole (CH), and notched tension (with notch radii denoted) tests are shown.

Table 3.1: Average stress triaxiality (η_{avg}), average Lode angle parameter ($\bar{\theta}_{avg}$), and local equivalent plastic strain at failure ($\bar{\varepsilon}_f$) for each test.

	CH	$\beta = 90°$	$\beta = 70°$	$\beta = 30°$	$\beta = 0°$	Punch	R6	R10	R20
η_{avg}	0.33	0.58	0.47	0.17	0.00	0.66	0.51	0.47	0.42
$\bar{\theta}_{avg}$	0.96	0.00	0.53	0.48	0.01	-1.00	0.41	0.54	0.72
$\bar{\varepsilon}^f$	0.605	0.369	0.296	0.507	0.746	0.738	0.318	0.318	0.324

3.4.2. Calibration of the MMC fracture model

Habibi et al. showed that the three-parameter version MMC model (MMC3) exhibited little error when describing the fracture behavior of DP600. It is therefore adopted here to describe the experimental results in the current study. This model describes the fracture strain $\bar{\varepsilon}_f$ as a function of the stress triaxiality η and Lode angle parameter $\bar{\theta}$:

$$\bar{\varepsilon}_f = \left\{ \frac{A}{c_2} \left[c_3 + \frac{\sqrt{3}}{2-\sqrt{3}} (1 - c_3) \left(\sec\left(\frac{\bar{\theta}\pi}{6} \right) - 1 \right) \right] \left[\sqrt{\frac{1 + c_1^2}{3}} \cos\left(\frac{\bar{\theta}\pi}{6} \right) + c_1 \left(\eta + \frac{1}{3} \sin\left(\frac{\bar{\theta}\pi}{6} \right) \right) \right] \right\}^{-\frac{1}{n}} \quad \text{Eq. 3.4}$$

where A and n are the Swift law parameters in Eq. 3.1, and c_1, c_2, and c_3 are the fracture model parameters.

While nine fracture tests were performed, only four of them were used for parameter calibration: CH, punch, and butterfly with $\beta = 0°$ and $70°$. Note that only c_1, c_2, and c_3 need to be calibrated, as A and n are determined from the tensile strain hardening behavior of the material. The values of these parameters are shown in Table 3.2. A comparison of the calibrated MMC model with the experimental data is shown in Figure 3.7a, in which the data points adopted for calibration are shown as solid symbols, while the

data points shown as open symbols validate the calibrated model. The validation data points in Figure 3.7a were, in general, captured by the calibrated MMC model, with an average error of 12%.

Table 3.2: Swift law and MMC model parameters calibrated in the current study.

	A	n	c_1	c_2	c_3
Current study	1004 MPa	0.16	0.222	587.7 MPa	1.037

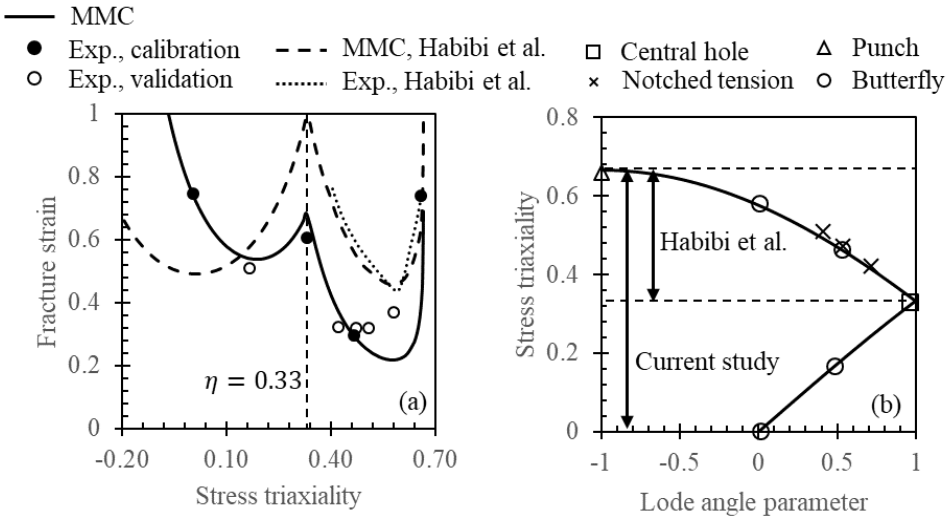

Figure 3.7: (a) Calibrated MMC model (solid line) along with experimental data used for model calibration (solid circles) and validation (open symbols) in the current study. The results reported by Habibi et al. [16] (dashed line and dotted line) are also included. (b) Stress triaxiality versus Lode angle parameter plot showing the stress state range used to calibrate the MMC model and the stress state(s) reached in the fracture tests in the current study.

3.4.3. Comparison of current MMC model with that calibrated by Habibi et al. [16]

In the work by Habibi et al. [16], the authors investigated the fracture behavior of 1 mm thick DP600, and calibrated the MMC model based on Nakazima tests with $\varepsilon_{minor}/\varepsilon_{major}$ ratios between -0.33 and 1, where ε_{minor} and ε_{major} are the minor and major strains in the tests. The stress state range reached in their tests is between uniaxial tension ($\eta = 0.33$, $\bar{\theta} = 1$) and equi-biaxial tension ($\eta = 0.67$, $\bar{\theta} = -1$). Their experimental results and the corresponding calibrated MMC model in their study are also shown in Figure 3.7a.

Comparing the MMC model reported by Habibi et al. [16] and the model calibrated in the current study, it is obvious that even though the absolute values of the fracture strains are different, the trend of the two calibrated models are similar for $\eta > 0.33$, but significantly different for $\eta < 0.33$. The difference in the absolute values of the fracture strains could be caused by differences in material supplier, material batch, or material specifications (e.g., thickness). However, the notable difference in trend in the $\eta < 0.33$ range is primarily caused by the difference in fracture model calibration, as this region was not directly studied by Habibi et al. [16]. Specifically, Figure 3.7b shows the stress state range used for MMC model calibration by Habibi et al. [16] and in the current study, as well as the stress state(s) achieved for each of the fracture specimens in the current study. While the MMC model reported by Habibi et al. was almost symmetric with respect to $\eta = 0.33$, the MMC model in the current study predicted much higher fracture strains in the $\eta < 0.33$ range. This comparison shows the possibility of MMC model to underestimating or overestimate fracture strains for stress states outside the calibration range. Therefore,

calibration of MMC model parameters should be made in a stress state range as wide as possible in order to get an accurate fracture behavior description, or its application to predict fracture under stress states outside of the calibration range should be avoided.

3.5. Summary and conclusions

In the current study, the stress state dependent fracture behavior of DP600 was investigated through a combined experimental and computational approach. The main conclusions are:

- The effect of stress state on fracture behavior can be studied through a combined experimental-computational approach, along with the selection of appropriate geometry samples to probe the stress range of interest. With the specimens used in the present study, fracture behavior under a wide range of stress states ($0 < \eta < 0.67$) was probed.
- The fracture behavior of DP600 exhibited a strong stress state dependence, with pure shear and equi-biaxial tension having the highest strain to failure values and tension-dominated combined loading having the lowest strain to failure values. The calibrated Modified Mohr-Coulomb model was able to accurately capture the stress state dependent fracture behavior of DP600 determined experimentally.
- Comparison of the MMC models calibrated in different stress state ranges revealed obvious difference between them, emphasizing the importance of calibrating the model in the full range of stress states of interests.

Application of MMC model to stress states out of the calibration range is not advised.

Chapter 4 Influence of phase and interface properties on the stress state dependent fracture initiation behavior in DP steels through computational modeling[4]

4.1. Introduction

This chapter aims to study the effect of stress state and phase/interface properties on fracture mechanisms while minimizing the contribution of martensite morphology through finite element simulations on an RVE model with an idealized microstructure consisting of a circular martensite particle at the center of a ferrite matrix. In the literature, attempts have been made to study the fracture behavior of DP steels through idealized RVE models. In the work by Al-Abbasi and Nemes, the authors developed RVE models containing two idealized circular martensite particles of different sizes to study the fracture behavior of DP steels [79]. They considered ferrite/martensite interface decohesion as the only fracture mechanism, which they modeled by embedding initial micro voids at the interfaces. The growth of these micro voids under loading was used to determine the parameters in a Gurson-Tvergaard-Needleman model, which was able to describe the fracture behavior of DP steels under uniaxial tension. However, the focus of their RVE simulations was to calibrate a fracture model that describes the macroscopic fracture

[4] Reproduced from: Qin, S., Lu, Y., Sinnott, S.B. and Beese, A.M., 2020. Influence of phase and interface properties on the stress state dependent fracture initiation behavior in DP steels through computational modeling. *Materials Science and Engineering: A*, p.138981.

behavior of the material, based only on void growth at the interface, instead of identifying the fracture mechanisms at the microscale.

Groups have also considered multiple fracture mechanisms with RVE modeling [34,35,38,51,80–83]. However, these RVE models were generally built based on actual microstructures, which better approach actual deformation behavior of DP steels, but do not allow for the decoupling of the effects of phase morphology and global stress state. In addition, most of these studies [34,51,79,82,83] have focused on only one globally applied stress state, and thus have not probed the dependence of fracture mechanisms on stress state.

In the present study, all three potential fracture initiation mechanisms were explicitly incorporated in the idealized RVE model. The RVE model was subjected to five different global stress states to investigate stress state dependent fracture mechanisms of DP steels. The influence of phase and interface properties on the failure initiation within DP steels was also studied. The stress state dependent modified Mohr-Coulomb model was adopted to simulate the ductile fracture behavior of ferrite, a cohesive zone model was adopted to simulate ferrite/martensite interface decohesion, and a maximum principal stress criterion was adopted to simulate martensite failure. Existing experimental and computational results were used to define a set of reference parameter values, and the corresponding fracture mechanisms under different applied stress states were investigated. The parameter values for martensite and for the cohesive interface were then varied to determine how fracture initiation behavior as a function of stress state changed with material properties. The parameter variation range for martensite was justified through its

carbon content, while that for the cohesive interface was justified through density functional theory (DFT) based calculations.

4.2. RVE modeling

4.2.1. RVE model with idealized morphology

To minimize the influence of martensite morphology on fracture initiation behavior of DP steels and focus on the influence of global stress state, an idealized RVE model containing a circular martensite grain at the center of a ferrite matrix (see Figure 4.1) was developed in Abaqus/Explicit [78]. This model is extruded along the thickness direction with the thickness being 5% of the in-plane dimensions to mimic a state of plane stress. A thin cohesive layer was included between the martensite grain and the ferrite matrix to capture the potential ferrite/martensite interface debonding behavior in DP steels. The mesh size in the ferrite/martensite interface and in each of the phases near the interface was refined to capture any potential stress/strain gradients. The finest mesh dimension was 0.005 μm, with the mesh coarsening with increased distance from the ferrite/martensite interface. In total, the model was discretized by 13,000 3D solid elements (C3D8 [78]) and 332 cohesive elements (COH3D8 [78]). During simulations, once an element fulfilled the assigned fracture criterion described in Section 4.2.2 - 4.2.4, it was deleted.

The martensite volume fraction in the model was prescribed to be 22%, per the experimental findings in [32]. In the current study, a pointwise plane stress state, instead of an average plane stress, was adopted on the surface of the model. If enforcing an average plane stress in Abaqus, the material points within each phase are required to move uniformly along the thickness direction. In comparison, the pointwise plane stress state

allows non-uniform, out-of-plane movement at every point, while mandating zero out-of-plane stress, which is consistent with experimental work in which microstructural fracture incidents on the specimen surface are studied [20,22,30].

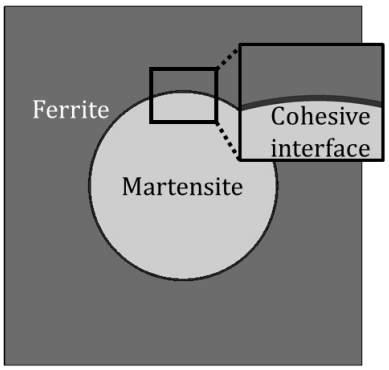

Figure 4.1: Illustration of the idealized RVE model, which contains a circular martensite grain in the center of a ferrite matrix. The cohesive layer between these two phases is used to represent the ferrite/martensite interface behavior.

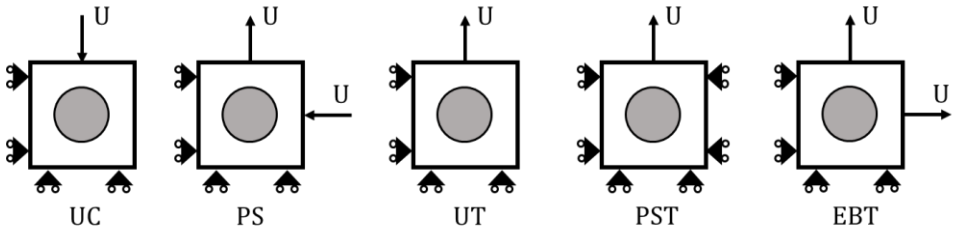

Figure 4.2: Boundary conditions applied for uniaxial compression (UC), pure shear (PS), uniaxial tension (UT), plane strain tension (PST), and equi-biaxial tension (EBT).

To investigate the influence of global stress state on the local stress state variations and fracture initiation behavior, the RVE model was subjected to the following five stress states: uniaxial compression, uniaxial tension, pure shear, plane strain tension, and equi-

biaxial tension. This covers nearly the full range of stress states that thin sheet metals can reach, as shown in Figure 1.2. The boundary conditions for all five loading conditions, are shown in Figure 4.2. Pure shear was modeled by applying tension in one direction and compression in the perpendicular in-plane direction.

4.2.2. Ductile fracture model for ferrite

Ferrite undergoes ductile fracture, which is generally taken to be the result of stress state dependent processes of void nucleation, growth, and coalescence [50,57,84–87]. To describe the stress state dependence of strain to failure of ductile materials, Bai and Wierzbicki proposed a modified Mohr-Coulomb (MMC) model [14] by transforming the Mohr-Coulomb model [88] from stress space to the space of ($\bar{\varepsilon}_f$, η, $\bar{\theta}$) using a stress state dependent plasticity model. In the current paper, the 3-parameter MMC model [60] is adopted, which describes the fracture strain as a function of stress triaxiality and Lode angle parameter through the following equation:

$$\bar{\varepsilon}_f = \left\{ \frac{A}{c_2} \left[c_\theta^s + \frac{\sqrt{3}}{2-\sqrt{3}} (1 - c_\theta^s) \left(\sec\left(\frac{\bar{\theta}\pi}{6}\right) - 1 \right) \right] \left[\sqrt{\frac{1+c_1^2}{3}} \cos\left(\frac{\bar{\theta}\pi}{6}\right) + c_1 \left(\eta + \frac{1}{3} \sin\left(\frac{\bar{\theta}\pi}{6}\right) \right) \right] \right\}^{-\frac{1}{n}} \quad \text{Eq. 4.1}$$

where A and n are Swift hardening law parameters ($\sigma_y = A(\varepsilon_0 + \bar{\varepsilon}^p)^n$, [72]), and c_1, c_2, and c_θ^s are model parameters. Bai and Wierzbicki showed that c_1 and c_θ^s control the shape of the fracture locus and c_2 controls the failure strain magnitude [14].

4.2.3. Brittle fracture model for martensite grains

Experimental observations have shown that the martensite grains in DP steel are brittle [18,89]. Therefore, in the present study, the maximum principal stress criterion was adopted to describe martensite failure such that martensite is assumed to fail when:

$$\sigma_1 > \sigma_c \qquad \text{Eq. 4.2}$$

where σ_1 is the maximum principal stress of a material point, and σ_c is the critical failure strength of the martensite.

4.2.4. Cohesive zone model for ferrite/martensite interface

Cohesive zone models are widely used for simulating fracture along interfaces due to their simple formulation, ease of implementation, and flexibility [90]. They have been adopted by researchers to simulate the ferrite/martensite interface decohesion behavior in DP steels [35,51,80,82,83]. In the current paper, the ferrite/martensite interface debonding behavior was simulated using a CZM consisting of a linear elastic traction-separation law coupled with a quadratic nominal stress damage initiation criterion. A typical linear elastic traction-separation response is illustrated in Figure 4.3. Before damage initiation, the slope of the traction-displacement curve is described by the interface stiffness, K. Damage begins to accumulate once the traction reaches the cohesive strength, t^0, after which the interface gradually loses its load-bearing capacity with increasing separation distance until failure. The energy per unit crack area required for this process, E^c, corresponds to the area under the traction-separation plot in Figure 4.3. In the most general form of this CZM, each of the parameters (K, t^0, and E^c) may have different values along the normal direction and the two tangential directions of an interface. In the current study, the behavior

is assumed to be the same in the two tangential directions. Therefore, six parameters (K_{nn}, t_{nn}^0, E_{nn}^c, K_{tt}, t_{tt}^0, and E_{tt}^c) are needed to fully define the cohesive interface behavior.

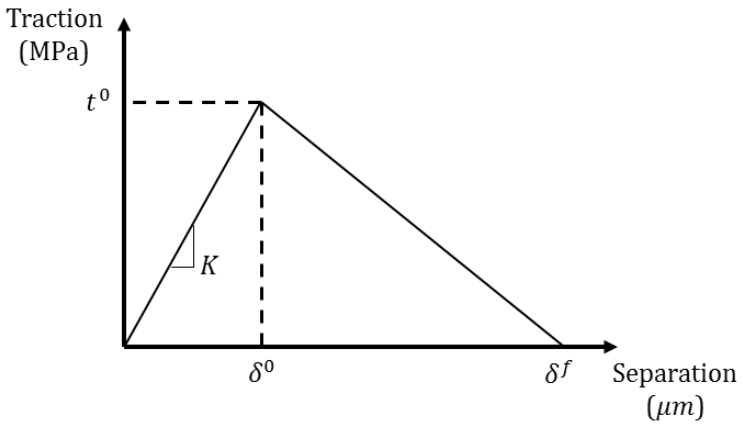

Figure 4.3: Illustration of the linear traction-separation law, where t^0 is the cohesive strength, δ^0 is the interface separation distance at t^0, K is the interface stiffness, and δ^f is the interface separation at total debonding.

Due to the complexity of experimentally determining the CZM parameters, assumptions on the relationships between parameters are commonly made, which reduce the number of independent parameters that need to be identified. In [91], Scheider and Brocks argued that the cohesive strength along the tangential direction should be much lower than the cohesive strength along the normal direction; thus, they assumed the following relationship:

$$t_{tt}^0 = 0.35 t_{nn}^0 \qquad \text{Eq. 4.3}$$

In addition, Roe and Siegmund related the tangential separation at maximum tangential traction, δ_{tt}^0, and the normal separation at maximum normal traction, δ_{nn}^0, through the equation $\delta_{tt}^0 = \frac{\sqrt{2}}{2}\delta_{nn}^0$ [92], suggesting that the cohesive energy be defined as:

$$E_{nn}^c = e t_{nn}^0 \delta_{nn}^0 \quad \text{Eq. 4.4}$$

$$E_{tt}^c = \sqrt{\frac{e}{2}} t_{tt}^0 \delta_{nn}^0 \quad \text{Eq. 4.5}$$

where $e \approx 2.7$ and δ_{nn}^0 is the normal separation at maximum normal traction. Combining the above with Eq. 4.3 gives the following relationships between the normal stiffness (K_{nn}) and tangential stiffness (K_{tt}) and between the cohesive energy under pure normal loading (E_{nn}^c) and the cohesive energy under pure tangential loading (E_{tt}^c):

$$K_{tt} = 0.49 K_{nn} \quad \text{Eq. 4.6}$$

$$E_{tt}^c = 0.15 E_{nn}^c \quad \text{Eq. 4.7}$$

Using these relationships, the number of independent parameters that must be defined for the CZM reduces to three: K_{nn}, t_{nn}^0, and E_{nn}^c.

4.3. Results and discussion

4.3.1. Model parameter identification

The flow behavior of ferrite and martensite defined in [32] were adopted in the current study, and can be described by a Swift law:

$$\sigma_y = A(\varepsilon_0 + \bar{\varepsilon}^p)^n \quad \text{Eq. 4.8}$$

with $A = 889$ MPa, $\varepsilon_0 = 0.005$, and $n = 0.177$ for ferrite, and $A = 4222$ MPa, $\varepsilon_0 = 0.006$, and $n = 0.247$ for martensite.

In DP steels, the properties of the constituent phases and the ferrite/martensite interface vary due to alterations in composition and processing parameters [34,69,93]. To investigate the impact of varying properties of the two phases and the ferrite/martensite interface on the stress-state dependent fracture initiation behavior in the microstructure, reference values for each of the failure parameters were selected, and a parametric study was performed to determine how the fracture mechanisms change with different parameters under different stress states.

Experimental fracture data on ferritic steel HT400 [94] was used to calibrate the MMC model parameters, given in Table 4.1, for the ferrite phase in the current study as shown in Figure 4.4. For martensite, a critical principal stress of $\sigma_c = 2140$ MPa reported by Ramazani et al. [34] was adopted.

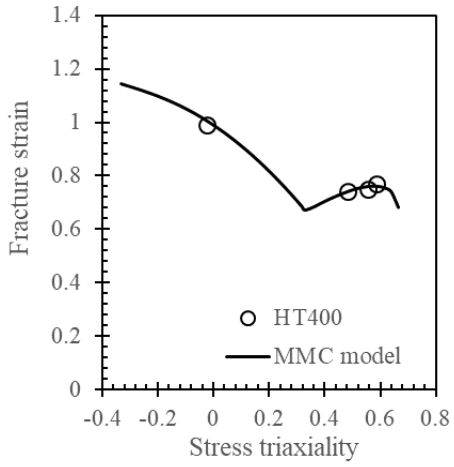

Figure 4.4: Experimental fracture strain of HT400 ferritic steel (symbols) from [94] and the corresponding calibrated Modified Mohr-Coulomb model (line).

As the ferrite/martensite interface properties are challenging to determine experimentally, there are no directly measured ferrite/martensite interface properties available in the literature. In the current work, the normal interface stiffness was assumed to be the same as the elastic modulus of the constituent phases (201 GPa/μm. Note that the constitutive thickness of the cohesive elements was 1 μm in the model). The cohesive strength of the interface was taken to be 1100 MPa along the normal direction, as given in [82]. In [95], Ramazani et al. predicted the ferrite/martensite interface energy to be 6×10^{-6} μJ/μm^2 via first-principles calculations. This value was taken as the reference value for the current work. All model parameter reference values are given in Table 4.1.

Table 4.1: Reference deformation and fracture model parameter values for ferrite, martensite, and their interface.

Ferrite	$\boldsymbol{A}$	$\boldsymbol{\varepsilon_0}$	$\boldsymbol{n}$	$\boldsymbol{c_1}$	$\boldsymbol{c_2}$	$\boldsymbol{c_\theta^s}$
	889 MPa	0.005	0.18	0.048	434 MPa	0.85
Martensite	$\boldsymbol{A}$	$\boldsymbol{\varepsilon_0}$	$\boldsymbol{n}$	$\boldsymbol{\sigma_c}$		
	4222 MPa	0.006	0.25	2140 MPa		
Interface	$\boldsymbol{K_{nn}}$	$\boldsymbol{K_{tt}}$	$\boldsymbol{t_{nn}^0}$	$\boldsymbol{t_{tt}^0}$	$\boldsymbol{E_{nn}^c}$	$\boldsymbol{E_{tt}^c}$
	201 GPa	100 GPa	1100 MPa	385 MPa	6×10^{-6} μJ/μm^2	0.9×10^{-6} μJ/μm^2

4.3.2. Fracture initiation behavior with reference parameter values

With the reference parameter values in Table 4.1, the idealized RVE model in Figure 4.1 was loaded under five different stress states: uniaxial compression, pure shear, uniaxial tension, plane strain tension, and equi-biaxial tension. All simulations were performed up to fracture initiation, which was defined as the moment when the first element reached its fracture criterion and was deleted. The location of the first element to be deleted was taken to be the fracture initiation site. The evolution of global stress states up to fracture initiation are shown in Figure 4.5a and c.

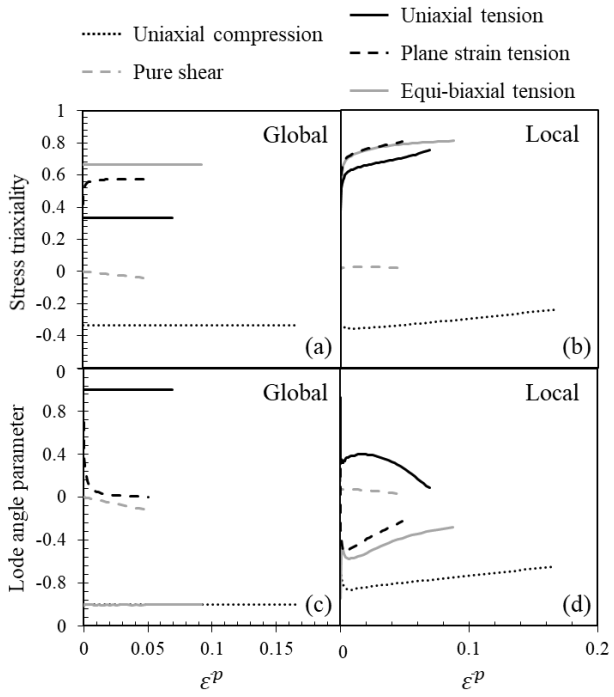

Figure 4.5: Evolution of global and local (a,b) stress triaxiality and (c,d) Lode angle parameter as a function of global von Mises equivalent plastic strain. The local variable values in (b) and (d) were extracted from the fracture initiation sites within ferrite marked in Figure 4.7.

The equivalent plastic strain fields in the model at a global equivalent plastic strain of 4% are shown in Figure 4.6. As highlighted in the figure, the local equivalent plastic strains in the ferrite were concentrated near the ferrite/martensite interface in all five stress states due to microstructural heterogeneity. However, the specific strain concentration sites were different for different stress states. For uniaxial compression and pure shear, they were at the regions that are 45° with respect to the first principal stress directions (the *y* direction). They approached the *y* direction in uniaxial tension and were fully aligned with the *y* direction in plane strain tension. The strain concentration sites were uniformly distributed along the ferrite/martensite interface in equi-biaxial tension.

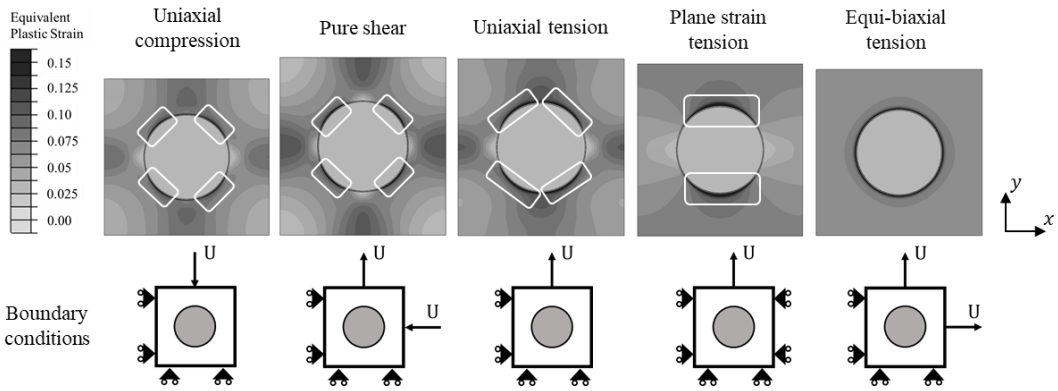

Figure 4.6: Local equivalent plastic strain fields in the idealized RVE model for a global equivalent plastic strain of 4% under uniaxial compression, pure shear, uniaxial tension, plane strain tension, and equi-biaxial tension. The boxes highlight the strain concentration sites in the simulations.

Simulation results showed that fracture initiated in ferrite for all stress states studied, as shown in Figure 4.7. Similar to the strain concentration sites, the microstructure inhomogeneity resulted in the fracture initiation sites being adjacent to the

ferrite/martensite interface, but their specific locations were different for different stress states. The evolution of local stress state at these locations up to fracture initiation is shown in Figure 4.5b and d. As global equivalent plastic strain increased, the local stress state at the fracture initiation site in the uniaxial tension simulation approached that of the local stress states in the plane strain tension and equi-biaxial tension simulations. This indicates that under tension dominated loading (uniaxial tension, plane strain tension, and equi-biaxial tension), the local stress state resulting in fracture initiation differed from the global stress state due to local microstructural inhomogeneity. Conversely, for uniaxial compression and pure shear the local stress state at the corresponding fracture initiation sites resembled their global counterparts.

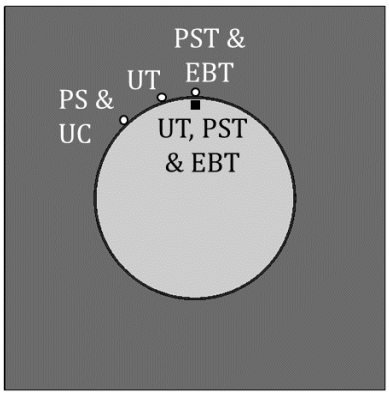

Figure 4.7: Fracture initiation sites in ferrite (circles) and martensite (square) when using the reference parameter values (Table 4.1) for loading under uniaxial compression (UC), pure shear (PS), uniaxial tension (UT), plane strain tension (PST), and equi-biaxial tension (EBT).

4.3.3. Fracture initiation behavior with varying parameter values

As noted above, when adopting the reference parameter values for martensite, ferrite, and their interface, fracture initiated in ferrite under all investigated stress states, meaning the dominant fracture initiation mechanism was stress state independent. Since the mechanical properties of ferrite, martensite, and their interface vary in DP steels, and fracture initiation from both phases and their interface have all been observed experimentally, it is of utility to vary the fracture model parameters to determine the effect of phase/interface properties and stress state on fracture initiation behavior.

For parameter variation, a metric is required to evaluate the relative failure behavior of each phase and interface. In the MMC model used for ferrite, the fracture behavior is described by a limit on equivalent plastic strain, while in the maximum principal stress criterion, used for martensite, the fracture behavior is described by a limit on stress. For comparative purposes, the fracture behavior of ferrite and martensite will be expressed in terms of fracture energy E_f, which is calculated from fracture strain $\bar{\varepsilon}_f$ for ferrite and from fracture stress σ_c for martensite, using the following equations:

$$E_f^F \approx E_f^p = \int_0^{\bar{\varepsilon}_f} \sigma_y^F \, d\bar{\varepsilon}^p \qquad \text{Eq. 4.9}$$

$$E_f^M = E_f^e + E_f^p = \frac{\sigma_c^2}{2E} + \int_0^{\bar{\varepsilon}_c^p} \sigma_y^M \, d\bar{\varepsilon}^p \qquad \text{Eq. 4.10}$$

where E_f^F and E_f^M are the fracture energies of ferrite and martensite, E_f^e and E_f^p are the elastic and plastic parts of the fracture energy, σ_y^F and σ_y^M are the flow stresses of ferrite and martensite given by Eq. 4.8, and $\bar{\varepsilon}_c^p$ is the plastic strain in martensite at the fracture stress σ_c. As shown in Figure 4.4, the MMC fracture strain for ferrite ($\bar{\varepsilon}_f$) is stress state

dependent. In the present study, the fracture strain for uniaxial tension was adopted to calculate the fracture energy of a given set of parameters. With the reference parameter values, this gives a ferrite fracture energy of 475×10^{-6} μJ/μm^3. For martensite, the calculated fracture energy corresponding to the reference critical principal stress ($\sigma_c = 2140$ MPa) is 115×10^{-6} μJ/μm^3. For the parametric study, the martensite and the ferrite/martensite interface fracture parameters were varied while keeping the ferrite properties constant.

4.3.3.1. Variation of martensite fracture parameters

Using data from Vickers microhardness tests, Koo et al. fitted a linear relationship between the ultimate tensile strength (UTS) of martensite in DP steels and the C content (in wt %) in martensite [96], which is given as:

$$\text{UTS} = 3241 \text{ MPa} \times \%C + 758 \text{ MPa} \qquad \text{Eq. 4.11}$$

Using ThermoCalc [97], Ramazani et al. predicted the C content of martensite in DP600 to be between 0.15 wt % and 1.3 wt % [69]. According to Eq. 4.11, a martensite C content of 0.15 wt % gives a UTS lower bound of 1244 MPa. Therefore, the martensite UTS in the current study was varied between this lower bound (1244 MPa) and the reference value (2140 MPa), which corresponds to a martensite fracture energy range of 5.2×10^{-6} μJ/μm^3 to 115×10^{-6} μJ/μm^3 (see Table 4.2).

Table 4.2: Fracture energy ranges used in parametric study.

	Martensite (μJ/μm^3**)**	**Interface (**μJ/μm^2**)**
Maximum value	115×10^{-6}	6×10^{-6}
Minimum value	5.2×10^{-6}	0.06×10^{-6}

4.3.3.2. Variation of cohesive energy based on DFT modeling[5]

In order to determine a relevant cohesive energy range for the ferrite/martensite interface, the density functional theory (DFT) was adopted. Supercells for both martensite and ferrite were created, with each phase containing 2 × 2 × 6 unit cells along three orthogonal directions, as illustrated in Figure 4.8. For each phase, a total of 6 layers were modeled and the center two layers were frozen during the relaxation in order to retain the crystal symmetry in the bulk form. Structural relaxation in the DFT-based calculations was performed through the plane-wave basis and projector augmented wave (PAW) method [98] within the Vienna Ab initio Simulation Package (VASP) [99]. The choice of the exchange-correlational functional is the Perdew–Burke–Ernzerhoff (PBE) [100] generalized gradient functional. The optB88-vdW functional was applied to account for dispersion interactions within the structure. Convergence tests showed that energies converged to within 1 meV atom^{-1} when a 500 eV cutoff energy with a 8 × 8 × 1 k-point mesh was adopted, which was then used for all the calculations. Structure relaxation was iterated until the energy differences were below 10^{-6} eV and until all forces on the atoms were below 0.05 eV Å^{-1}.

In the current study, the work of adhesion, which we refer to here as the cohesive energy of the ferrite/martensite interface, is calculated as $E_{nn}^{c} = \gamma_F + \gamma_M - \gamma_{FM}$, where γ_F and γ_M are the surface energies for ferrite and martensite, respectively, when they are separate, and γ_{FM} is the energy per unit area when ferrite and martensite are stacked

[5] The work in this subsection was led by Y. Lu and S.B. Sinnott.

together. A large value of work of adhesion indicates a stable interfacial structure, meaning that the stacked structure is preferred over the separate one.

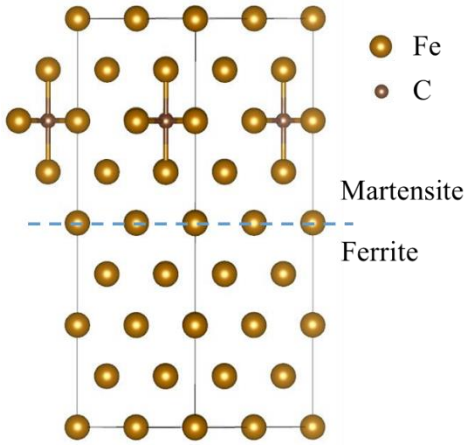

Figure 4.8: Illustration of the supercells for both ferrite and martensite.

The work of adhesion is not constant and depends on a variety of parameters like interface orientations, stacking fault at the interface, and C interstitial locations in the martensite. In the current study, these parameters were varied to probe the possible range of the work of adhesion. While the C concentration in the martensite was also varied, it was found to have only a limited influence on work of adhesion. Due to the extremely low C concentrations in ferrite, C was not included in the DFT-based model of ferrite [69]. Because of the limited supercell size capable in DFT-based calculations, only two interface orientations were investigated in the current study, i.e., (001) and (110). The models were created both with and without a stacking fault at the interface. Here, a stacking fault at the interface means the (001) plane of the ferrite phase was stacked on the (001) plane of the martensite phase, and it is eliminated when the ferrite (001) plane is stacked on the martensite (002) plane. A similar rule also applies to the (110) oriented interface. In the

martensite, the C atom was placed either at the interface or at the center of the martensite supercell.

With different combinations of the above parameters, a total of 18 model configurations were calculated. The predicted work of adhesion range was $0.16 \times 10^{-6} - 5.83 \times 10^{-6}$ $\mu J/\mu m^2$. The upper bound corresponds to when the (110) plane of ferrite was stacked on the (220) plane of martensite and when the C atom was away from the interface, while the lower bound corresponds to when the (001) plane of ferrite was stacked on the (110) plane of martensite and the C atom was at the interface. The trend from the predictions indicates that atomic mismatch decreased the interface stability dramatically. Meanwhile, the C interstitials in martensite increased the original Fe-Fe bond length so that C interstitials at the interface made the stacked structure easier to separate resulting in a lower work of adhesion. Therefore, C interstitials at the misoriented interface between ferrite and martensite could generate a less stable interface, resulting in a higher possibility of creating defects. The cohesive energy range investigated in the current study is also summarized in Table 4.2.

4.3.3.3. Simulation results with varying parameter values

For each parameter set, the model was loaded under the five stress states shown in Figure 4.2, and a total of over 100 simulations were performed. The fracture initiation behavior in the simulations was categorized into three types: fracture initiation in ferrite, fracture initiation at the ferrite/martensite interface, and fracture initiation in martensite. The simulation results, along with boundaries delineating the transition of fracture initiation types as a function of stress triaxiality (for plane stress conditions) and fracture

energy, are shown in Figure 4.9a and b. The results are expressed as a function stress triaxiality only because with the plane stress assumption in the current study, the Lode angle parameter is coupled with stress triaxiality through Eq. 1.3. Of the stress states studied, there are no cases where the stress triaxiality is equal but Lode angle differs in two separate stress states. Some of the stress states studied – uniaxial compression and equi-biaxial tension as well as pure shear and plane strain tension – have the same Lode angle parameter but different stress triaxiality values; therefore, the difference in their fracture initiation behavior can be attributed to stress triaxiality alone. However, in general, the stress states studied do not allow for the decoupling of the effects of Lode angle and stress triaxiality. Therefore, as stress triaxiality has a more clearly defined physical meaning, we focus on its influence here.

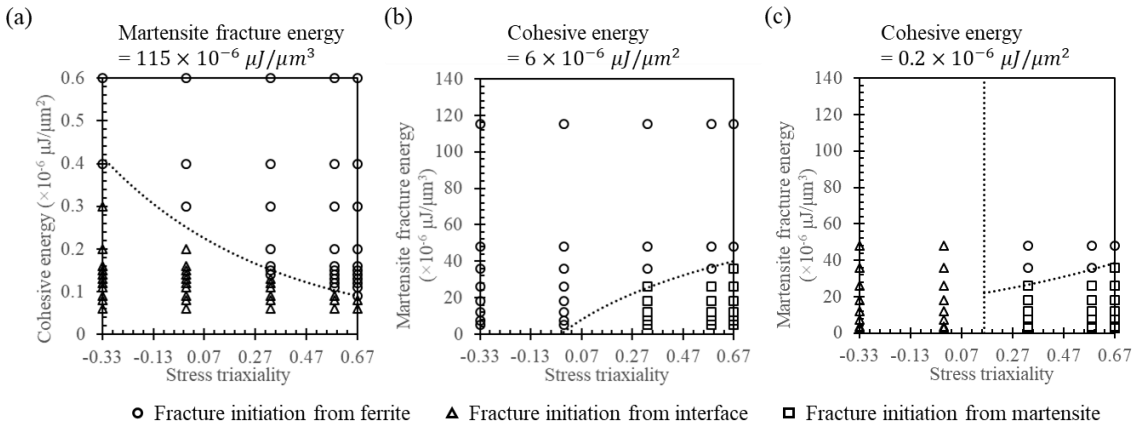

Figure 4.9: Energy versus stress triaxiality (for plane stress conditions) combinations that led to transitions in fracture initiation sites between (a) the ferrite/martensite interface and ferrite, (b) ferrite and martensite, and (c) the ferrite/martensite interface and martensite. Each symbol indicates one simulation, and the lines mark the approximate boundaries between different dominant mechanisms.

It is noted that the transition from fracture initiation in ferrite to the cohesive interface depended on the global stress triaxiality, and changed with triaxiality when the cohesive energy was between 0.09×10^{-6} μJ/μm^2 and 0.4×10^{-6} μJ/μm^2 (equivalent to 0.02% to 0.09% of the ferrite fracture energy). Figure 4.9a also shows that fracture tended to initiate from the ferrite/martensite interface for low stress triaxialities and from ferrite for high stress triaxialities.

On the other hand, the transition from failure within ferrite to failure within martensite was stress state dependent only when the martensite fracture energy was lower than 36×10^{-6} μJ/μm^3, or 10% of the ferrite fracture energy. When investigating the ductile to brittle transition temperature of DP590 and AISI-1018 steels, Chao et al. showed that the ratio of brittle to ductile fracture energy was between 5% and 27% [101], indicating a fracture energy ratio of martensite to ferrite of 10% or lower is appropriate. Since fracture initiation in martensite was not observed under pure shear and uniaxial compression in the current simulations, even with the lowest martensite fracture energy probed (3.8×10^{-6} μJ/μm^3), corresponding to the martensite UTS lower bound discussed in Section 4.3.3.1, it is concluded that fracture does not initiate from martensite in DP steels under uniaxial compression or pure shear loading. The fracture initiation sites in martensite were the same for all three other loading types (uniaxial tension, plane strain tension, and equi-biaxial tension), as indicated by the square in Figure 4.7, while the fracture initiation sites in ferrite were dependent on the global stress state.

In addition to the simulations above, one additional set of simulations was performed to inspect the fracture initiation transition between martensite and the ferrite/martensite interface. This was achieved by setting the cohesive energy to

0.2×10^{-6} μJ/μm^2 and varying the martensite fracture energy. The cohesive energy was chosen such that stress state dependent fracture initiation behavior was observed (refer to Figure 4.9a). The corresponding fracture initiation site transition behavior is shown in Figure 4.9c. At low stress triaxialities, fracture always initiated at the ferrite/martensite interface, while at high stress triaxialities, fracture initiated either from martensite or ferrite, depending on the martensite fracture energy.

The results above demonstrate that the fracture initiation mechanisms in the microstructure of DP steels are a result of both material/interface properties and macroscopically applied stress state. Material/interface properties exhibit a stronger influence on the fracture initiation mechanisms than the macroscopic applied stress state within the material and stress state ranges investigated. It is also clear from Figure 4.9 that when the fracture initiation behavior was stress state dependent, failure tended to initiate at the ferrite/martensite interface at low stress triaxialities, in ferrite at intermediate stress triaxialities, and in martensite at high stress triaxialities.

4.4. Conclusions

In the current study, the stress state dependent fracture mechanisms of DP steels were investigated through micromechanical simulations. In order to study the influence of global stress state on fracture initiation while minimizing the influence of martensite morphology, an idealized RVE model was adopted. The primary contributions of this study include:

- Fracture criteria for all three possible failure locations (i.e., in ferrite, in martensite, or at the ferrite/martensite interface) were explicitly modeled in

the idealized RVE model in the current study. Reference fracture model parameter values were determined based on experimental or computational results reported in the literature. With the reference parameter values, fracture initiation in ferrite was dominant regardless of stress state.

- To determine the relative importance of constituent material properties on stress state dependent failure, a parametric study was performed in which the fracture model parameters of martensite and the ferrite/martensite interface were varied. The appropriate ranges for fracture energy were determined based on C content in martensite, and first-principles calculations for the ferrite/martensite interface. Simulation results showed that the fracture initiation behavior was stress state dependent when the martensite fracture energy and/or the interface cohesive energy were within a certain subset of their respective variation ranges, indicating that heterogeneities in actual microstructures, together with phase/interface properties, can drive stress state dependent fracture initiation.
- When fracture initiation behavior is stress state dependent, fracture initiates from martensite under high global stress triaxialities, from ferrite at intermediate global stress triaxialities, and from the ferrite/martensite interface at low global stress triaxialities. Under pure shear and uniaxial compression loading, fracture never initiates from martensite.
- Regardless of the macroscopic stress state, under tension-dominated loading the local stress triaxiality values at the fracture initiation sites within the ferrite are similar among different loading conditions. This is attributed

to microstructural inhomogeneities, highlighting their dominant effect on the microstructure level fracture initiation behavior in DP steels when subjected to tension-dominated loading. In uniaxial compression and pure shear loading, the local stress triaxiality values at the fracture initiation sites within the ferrite resembled their global counterparts, indicating that global stress state also played a role in initiating local fracture.

Chapter 5 Multiaxial fracture of DP600 and the microstructural level mechanisms through micromechanics modeling[6]

5.1. Introduction

The fracture behavior of DP steels has been investigated at both the macroscale and the microscale. Studies at the macroscale consider the material as a continuum and describe the fracture behavior observed experimentally either through forming limit diagrams (FLDs) [16,102,103] or through a function that describes fracture strain as a function of stress state [15,16]. Habibi et al. compared the ability of six fracture models to capture the fracture behavior of DP600 measured through Nakazima tests [16]. Their results showed that the maximum shear stress model, the modified Mohr-Coulomb (MMC) model, and the Lou-Huh fracture model reasonably captured the fracture test results over the stress state studied. In a similar study, Qin and Beese calibrated the MMC model for DP600 based on experiments spanning a wider stress state range than in ref. [16], capturing the material's fracture behavior in the low stress triaxiality range [104], and highlighting the importance of calibrating fracture models over a wide stress state range for a comprehensive description of material behavior.

While RVE models have been subjected to multiaxial loadings in limited studies, only two of these studies compared the simulation results with multiaxial loading

[6] Reproduced from: Qin, S. and Beese, A.M., 2020. Multiaxial fracture of DP600 and the microstructural level mechanisms through micromechanics modeling. *In prep*.

experimental data [35,49]. Lian et al. loaded an RVE model of DP600 under uniaxial tension, plane strain tension, and equi-biaxial tension [49], and predicted a stress state dependent damage initiation strain that agree well with macro scale experiments. However, these simulations were performed without fracture models included for the constituent phases; instead, the stress drop in the simulations due to microstructure inhomogeneity was taken as an indication of damage initiation. In another study, Uthaisangsuk et al. loaded RVE models under different stress states using a multiscale approach [35]. The authors performed macroscale finite element simulations of Nakazima stretching and hole expansion tests, and applied the local deformation field where cracks initiated as the boundary conditions in RVE simulations. They used the GTN model [50,57] to simulate ferrite fracture and a cohesive zone model to simulate ferrite/martensite interface decohesion. The moment of fracture initiation in the RVE simulations agreed well with experiments.

Despite existing investigations of the multiaxial fracture behavior of DP steels through RVE simulations, a comprehensive study simulating the microstructural level stress state dependent fracture behavior of DP steels, with fracture models incorporated for both phases, is absent. The simulations by Lian et al. [49] addressed only three stress states and did not include fracture models for ferrite or martensite, while the simulations by Uthaisangsuk et al. [35] addressed only two stress states, and did not focus on the stress state dependent fracture strain. Simulating the fracture behavior under different stress states is critical to the understanding of the fracture mechanisms of DP steels.

In the current study, an RVE model based on the microstructure observed in DP600 steel, and with fracture models defined for the constituent phases, was developed and

studied under seven different stress states. The simulations of the RVE model under deformation provide information about the distribution of stress/strain within the microstructure, local stress state, and the initiation and propagation of microcracks due to microstructural inhomogeneity. This information was used to predict the continuum level stress state dependent fracture strains of DP600, which were compared to experimental data. Five microscale criteria used to define RVE-level are presented. The continuum level strain to failure and dominant fracture mechanisms were found to be stress state dependent regardless of whether or not the fracture models for the individual phases were stress state dependent.

5.2. RVE modeling

5.2.1. Microstructure characterization

The microstructure of the 1.6 mm thick DP600 sheet studied was characterized through electron backscattered diffraction (EBSD). The two phases present in DP steels, ferrite and martensite, have similar crystal structures: ferrite is body-centered cubic (bcc) while martensite phase is body-centered tetragonal (bct). Compared to the bcc structure of ferrite, the bct structure of martensite is only slightly distorted along one direction: if c is the lattice parameter along the distorted direction and a is that along the other two directions, the c/a ratio is between 1 and 1.08, depending on the martensite carbon content [105,106]. As a result, conventional Kikuchi patterns in EBSD cannot distinguish the two phases. However, if indexing martensite as bcc ferrite, the quality of its Kikuchi pattern, referred as Image Quality (IQ), will be lower compared to that of ferrite due to the distorted lattice structure [29,107]. Thus, the two phases can be separated by comparing the IQ

values. The IQ-based phase map of the current material is shown in Figure 5.1a, showing a martensite volume fraction of 10%. The inverse pole figure of the same region, as shown in Figure 5.1b, revealed that the grains were equiaxed without any preferred orientation.

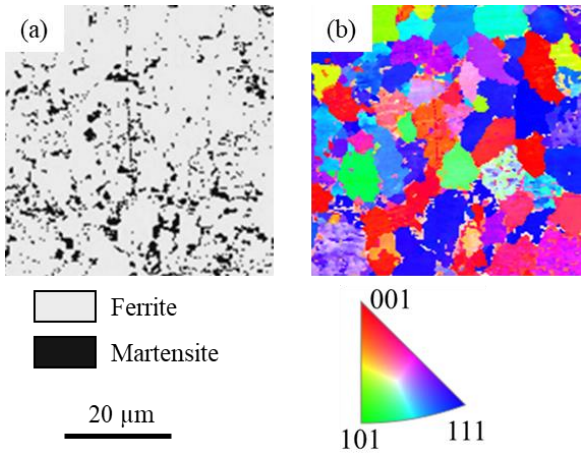

Figure 5.1: (a) Phase map of DP600 constructed based on the image quality map. (b) Inverse pole figure of the region in (a), showing equiaxed grains with random orientations.

5.2.2. RVE model

In order to simulate the fracture behavior of DP600 at the microscale, RVE models based on the observed microstructure were constructed in the finite element software ABAQUS [78]. The in-plane size of the RVE models was chosen to be 40 μm × 40 μm, consistent with a previous study on DP600 [32]. The ferrite was modeled as a homogenous continuum with martensite distributed throughout based on the EBSD IQ-based phase maps. To avoid unrealistic stress concentration caused by sharp martensite boundaries, the martensite profiles were modeled with splines (Figure 5.2a).

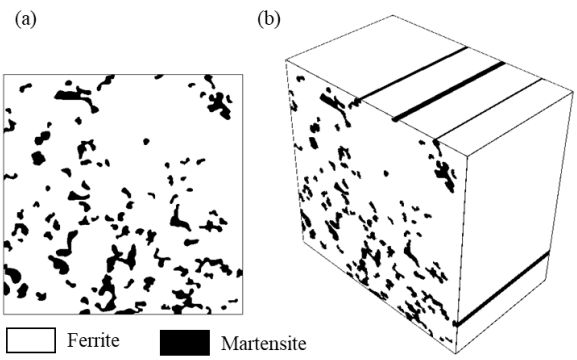

Figure 5.2: RVE model developed based on optical images of DP600. (a) Front view of the model showing the distribution of martensite. (b) Three-dimensional view showing the extrusion of the model. The in-plane size of the model is 40 μm by 40 μm, with an extruded thickness of 25 μm.

While phase maps give a two-dimensional image of microstructure, microstructure and stress state are intrinsically three-dimensional. To approximate the three-dimensional nature, the RVE model was extruded along the third direction (Figure 5.2b). To determine an appropriate thickness, extruded RVE models of different thicknesses were investigated and loaded under uniaxial tension, and their simulated engineering stress strain curves were compared as shown in Figure 5.3. For comparison, two-dimensional versions of the model without extrusion were also studied. In the three-dimensional models, hexahedral reduced integration elements (element type C3D8R [78]) were used. In the two-dimensional models, either plane stress elements (element type CPS4 [78]) or generalized plane strain elements (element type CPEG4 [78]) were used, resulting in pointwise plane stress and average plane stress, respectively. A discussion on the differences between these conditions is given in ref. [32]. In the current study, all three-dimensional models were

simulated using ABAQUS/explicit, while all two-dimensional models were simulated with ABAQUS/implicit [78].

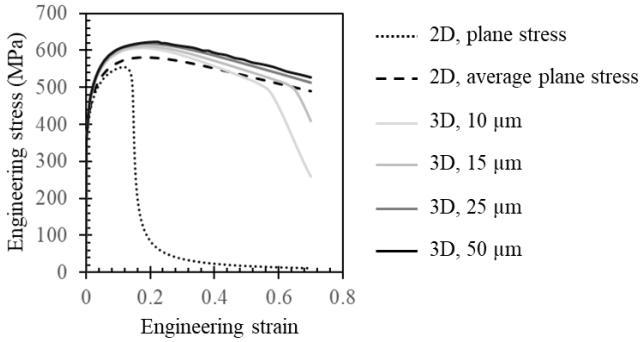

Figure 5.3: Simulated engineering stress strain curves from three-dimensional models extruded to different thicknesses, and their comparison to two-dimensional models with different out-of-plane stress states.

Comparison of the engineering stress strain curves in Figure 5.3 shows that the responses of the three-dimensional models were similar to that of the two-dimensional average plane stress model, while the two-dimensional pointwise plane stress model resulted in an early drop of the engineering stress. The early drop of engineering stress was also observed for three-dimensional models with small thicknesses, but was absent in the studied strain range when the thickness was 25 μm or greater. Therefore, in subsequent studies, the three-dimensional model with a thickness of 25 μm was adopted. The 25 μm thick model was discretized with of 366,951 hexahedral C3D8R elements with an in-plane element size of ~ 0.8 μm and out-of-plane element size of 2 μm.

The RVE model was subjected to seven different loading conditions including uniaxial tension and six multiaxial loading states with different U_1/U_2 ratios (0.55, 0.5,

0.45, 0.4, 0, and -1) as illustrated in Figure 5.4. Note that $U_1/U_2 = 0$ corresponds to plane strain tension and $U_1/U_2 = -1$ corresponds to equi-biaxial tension. For uniaxial tension, the right boundary was kept vertical but free to move horizontally. No constraints along the out-of-plane direction was applied, so the RVE model was always under a global plane stress state.

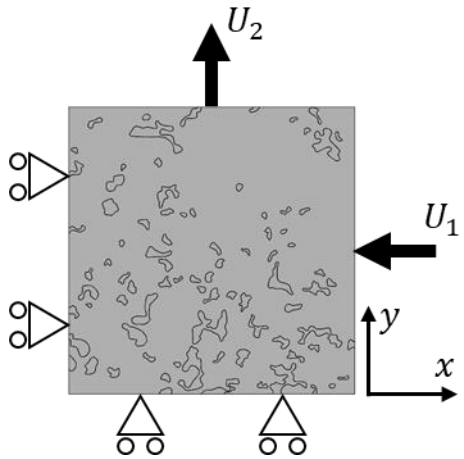

Figure 5.4: Schematic of the displacement boundary conditions applied in the multiaxial loading simulations of the RVE model in the current study.

5.2.3. Plasticity and fracture models for ferrite and martensite

In the current study, the plasticity behavior of each phase was modeled with a von Mises yield surface, associated flow rule, and a Swift law hardening relationship given as:

$$\sigma_y = A\left(\varepsilon_0 + \bar{\varepsilon}_p\right)^n \qquad \text{Eq. 5.1}$$

where σ_y is the yield stress, $\bar{\varepsilon}^p$ is the equivalent plastic strain, and A, n, and ε_0 are fitted parameters. The Swift law parameters for both phases were determined from micro-pillar compression test results reported by Madej et al. [39], while the A value for ferrite was

calibrated based on the measured uniaxial tension data in the present study. The calibrated plasticity model parameters are given in Table 5.1.

Table 5.1: Calibrated strain hardening parameters for ferrite and martensite.

	A	n	ε_0
Ferrite	889 MPa	0.177	0.005
Martensite	4222 MPa	0.247	0.006

To simulate fracture at the micro scale, the MMC model was used to describe failure in ferrite and a maximum principal stress criteria was used to describe failure in martensite phase. The MMC model describes the fracture strain $\bar{\varepsilon}_f^{ferrite}$ as a function of stress triaxiality η and Lode angle parameter $\bar{\theta}$:

$$\bar{\varepsilon}_f^{ferrite} = \left\{ \frac{A}{c_2}\left[c_3 + \frac{\sqrt{3}}{2-\sqrt{3}}(1-c_3)\left(\sec\left(\frac{\bar{\theta}\pi}{6}\right)-1\right)\right]\left[\sqrt{\frac{1+c_1^2}{3}}\cos\left(\frac{\bar{\theta}\pi}{6}\right) + c_1\left(\eta + \frac{1}{3}\sin\left(\frac{\bar{\theta}\pi}{6}\right)\right)\right]\right\}^{-\frac{1}{n}} \quad \text{Eq. 5.2}$$

where A and n are the Swift law parameters, and c_1, c_2, and c_3 are model parameters. Additionally, a ferrite damage indicator D was calculated as:

$$D^{ferrite} = \int_0^{\bar{\varepsilon}^{p,ferrite}} \frac{d\bar{\varepsilon}^{p,ferrite}}{\bar{\varepsilon}_f^{ferrite}} \quad \text{Eq. 5.3}$$

where $\bar{\varepsilon}^{p,ferrite}$ is the equivalent plastic strain in ferrite. For damage accumulation, the initial value of $D^{ferrite}$ is 0, and it increases with plastic deformation. Fracture of an element is defined to occur when $D^{ferrite} = 1$.

To describe the brittle martensite phase, the maximum principal stress failure criterion was adopted, which indicates failure occurs when:

$$\sigma_1 = \sigma_c^{martensite} \qquad \text{Eq. 5.4}$$

where σ_1 is the maximum principal stress at a material point, and σ_c is the critical stress for martensite failure. A damage indicator for martensite was computed in simulations to identify the ratio of the maximum principal stress at a given time to the failure stress at each point within martensite, or:

$$D^{martensite} = \frac{\sigma_1}{\sigma_c^{martensite}} \qquad \text{Eq. 5.5}$$

5.3. Microstructural level fracture criteria

To assess the ability of the RVE modeling to capture the stress state dependent macroscale strain to failure behavior, five microstructure-level fracture criteria were defined and considered as defined below. In what follows, all crack lengths and damage areas are defined in terms of the reference (undeformed) configuration.

- **Crack length 1 (CL1)**: The RVE was considered to have reached fracture when the projected length of the major crack in the RVE model exceeded 50% of the model size: $\frac{l_c}{w} \geq 50\%$, where w is the model width and l_c is the projected length of the major crack. The major crack was defined as that which eventually resulted in total separation of the model; therefore, only the microcracks that composed the crack resulting in final failure were considered. Overlapping projections of the major cracks were only counted once (Figure 5.5a).

- **Crack length 2 (CL2)**: A criterion similar to CL1, but the overlapping projections of the major cracks were all considered: $\frac{l_c}{w} = \frac{l_{c1}+l_{c2}+l_{c3}}{w} \geq f_{CL2}^c$, where f_{CL2}^c is the critical ratio for failure (Figure 5.5b). By including the overlapping projections of the crack, this criterion considers the contribution of all microcracks that eventually contribute to total separation of the model.
- **Damage area (DA)**: The RVE was considered to have reached fracture when the area of all cracks in the model exceeded a critical percentage of the model total area (Figure 5.5c): $\frac{A_{damage}}{A_{model}} \geq f_{DA}^c$, where A_{damage} and A_{model} refer to the initial 2D area of eventually deleted elements and the initial 2D area of the model, respectively, and f_{DA}^c is the critical ratio for failure. Different from the CL1 and CL2 criterion, all microcracks, regardless of whether they eventually formed the major crack, were considered.
- **Engineering stress drop (SD-eng)**: The RVE was considered to have reached fracture when the engineering stress along the maximum principal stress direction in the model dropped a critical fraction of its peak value (Figure 5.5d): $\frac{\sigma_{drop}^{Eng}}{\sigma_{max}^{Eng}} \geq f_{eng}^c$. In the present study, the vertical direction corresponded to the maximum principal stress direction in all loading cases.
- **Von Mises stress drop (SD-vM)**: The RVE was considered to have reached fracture when an equivalent stress dropped a critical percentage compared to its peak value. In this study, the von Mises stress formulation was

adopted to calculate this equivalent stress (Figure 5.5e): $\frac{\sigma_{drop}^{vM}}{\sigma_{max}^{vM}} \geq f_{vM}^{c}$. Compared to the SD-eng criterion, this criterion considers the influence of the second and third principal stresses when evaluating the loss of load bearing capacity.

Among the five microstructure-level fracture criteria above, three (CL1, CL2, and DA) describe microstructure-level fracture in terms of the geometry of microcrack formation, while the other two (SD-eng and SD-vM) describe RVE-level fracture in terms of a critical loss of load bearing capacity.

5.4. Model parameter calibration

5.4.1. Model parameters for ferrite and martensite fracture

Koo et al. estimated the ultimate tensile strength (UTS) of martensite in DP steels through Vickers microhardness tests, and found the following linear relationship between the UTS of martensite and its carbon content (in wt %) [96]:

$$\mathrm{UTS} = 3241\ \mathrm{MPa} \times \%C + 758\ \mathrm{MPa} \qquad \text{Eq. 5.6}$$

Ramazani et al. [69] provided another empirical relationship between martensite volume fraction and carbon content in martensite:

$$\mathrm{C}\% = 3 \times 10^{-9} \times V_m^6 - 5 \times 10^{-7} \times V_m^5 + 4 \times 10^{-5} \times V_m^4 - 0.0017 \times V_m^3 + 0.0392 \times V_m^2 - 0.4857 \times V_m + 2.9273 \qquad \text{Eq. 5.7}$$

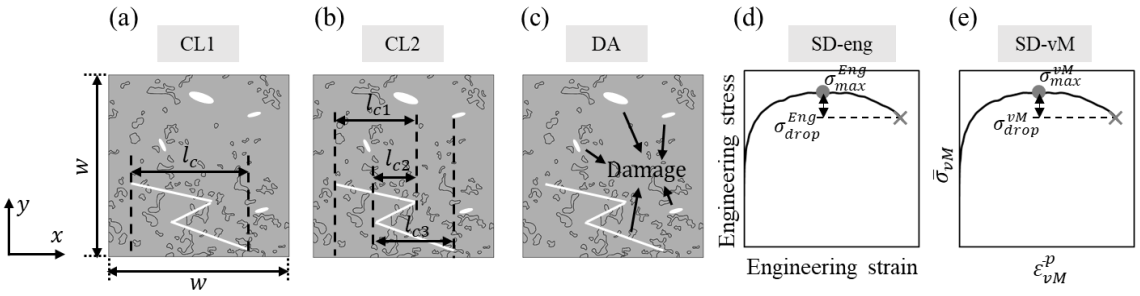

Figure 5.5: Schematic of the microstructural fracture criteria adopted in the current study: (a) crack length 1 (CL1), (b) crack length 2 (CL2), (c) damage area (DA), (d) engineering stress drop (SD-eng), and (e) von Mises stress drop (SD-vM). The white areas in (a), (b), and (c) indicate failed elements in the simulations, and w is the size of the model (40 μm in the current study), A_{damage} and A_{model} refer to the total area of the white regions and total area of the model, respectively.

where V_m is the volume fraction of martensite. Based on Eq. 5.6 and Eq. 5.7, and the martensite volume fraction, the fracture stress, σ_c, for martensite can be estimated. This gives a value of $\sigma_c^{martensite}$ =2865 MPa for the current study.

For ferrite, the c_1 and c_3 in the MMC model reported in ref. [108] were adopted, while c_2 was calibrated in the present study by matching the simulated fracture strain with the CL1 criterion under uniaxial tension with that determined experimentally in Chapter 3. The calibrated fracture model parameters for both phases are given in Table 5.2.

Table 5.2: Calibrated fracture parameters for ferrite and martensite.

	$\boldsymbol{\sigma_c}$	$\boldsymbol{c_1}$	$\boldsymbol{c_2}$	$\boldsymbol{c_3}$
Ferrite	-	0.048	500 MPa	0.846
Martensite	2865 MPa	-	-	-

5.4.2. Parameters for microstructure-level fracture criteria

With the parameters in Table 5.2, the RVE model was loaded under uniaxial tension up to the point when the CL1 fracture criterion was fulfilled. The crack length, damage area, engineering stress drop, and von Mises stress drop at this configuration were computed, and these values were defined as the critical values corresponding to failure in each of these microfracture models (i.e., f_{CL2}^{c}, f_{DA}^{c}, f_{eng}^{c}, and f_{vM}^{c}). These values are given in Table 5.3.

Table 5.3: Calibrated parameters for the microstructure-level fracture criteria, based on uniaxial tension.

f_{CL2}^{c}	f_{DA}^{c}	f_{eng}^{c}	f_{vM}^{c}
0.5	0.011	0.43	0.13

5.5. Results

With the RVE- level fracture criteria in Section 5.3, the ability of RVE simulations to describe and predict the macroscale stress state dependent fracture strain of the material is assessed while the RVE based simulations also provide information on microcrack initiation and propagation behavior, thus casting light on failure micromechanisms. In this section, the RVE simulated stress state dependent fracture strain will be discussed and compared to macroscopic experimental data. The simulated fracture mechanisms will be discussed in Section 0.

5.5.1. RVE simulation results

In the simulations in which the RVE model was loaded under uniaxial tension and six multiaxial loading conditions, the evolution of global stress triaxiality η^{global} and Lode angle parameter $\bar{\theta}^{global}$, as defined in Eq. 1.1 and Eq. 1.2, were computed. These evolutions are plotted versus the global (RVE-level) von Mises equivalent plastic strain for all loading conditions in Figure 5.6. The global von Mises equivalent plastic strain was calculated as:

$$\bar{\varepsilon}^{p,global} = \sqrt{\frac{2}{3}\left[\left(\varepsilon_{11}^{p,global}\right)^2 + \left(\varepsilon_{22}^{p,global}\right)^2 + \left(\varepsilon_{33}^{p,global}\right)^2\right]} \qquad \text{Eq. 5.8}$$

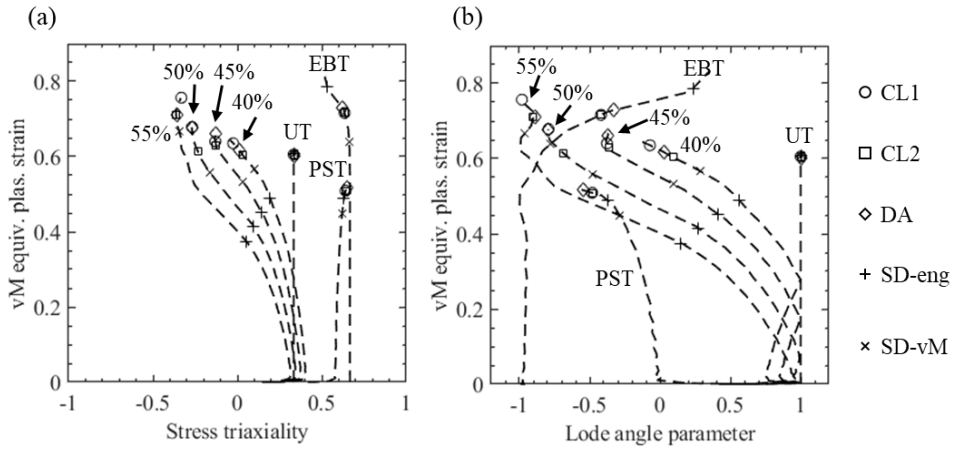

Figure 5.6: Evolution of global (a) stress triaxiality and (b) Lode angle parameter in the RVE simulations. The symbols mark the moment of fracture determined by the respective microstructural fracture criteria. UT: uniaxial tension. PST: plane strain tension. EBT: equi-biaxial tension. The percentages in the figure indicate the U_1/U_2 ratio applied in the boundary conditions.

where $\varepsilon_{11}^{p,global}$, $\varepsilon_{22}^{p,global}$, and $\varepsilon_{33}^{p,global}$ are the global plastic strains along the *x*, *y*, and *z* directions (Figure 5.4), respectively. The values of $\varepsilon_{11}^{p,global}$ and $\varepsilon_{22}^{p,global}$ are calculated based on the displacements and forces on the top and right boundaries, while $\varepsilon_{33}^{p,global} = -\left(\varepsilon_{11}^{p,global} + \varepsilon_{22}^{p,global}\right)$ through the assumption of plastic incompressibility.

For each loading condition, the simulated fracture strains $\bar{\varepsilon}_f^{global}$, defined as the value of $\bar{\varepsilon}^{p,global}$ at the moment an RVE-level fracture criterion was fulfilled, as a function of stress state, are given in Figure 5.6. The values of $\bar{\varepsilon}_f^{global}$ differed for fracture criteria, with their difference increasing with shear dominated loading conditions (U_1/U_2 ratios of 0.55, 0.5,0.45, or 0.4) compared to tension dominated conditions (plane strain tension, for which U_1/U_2=0 and equi-biaxial tension, for which U_1/U_2=-1). The $\bar{\varepsilon}_f^{global}$ values as a function of global stress state and RVE-level fracture criteria are given in Table 5.4.

In addition, the criteria based on load bearing capacity (SD-eng and SD-vM) predicted smaller fracture strains than the criteria based on crack length/area (CL1, CL2, and DA) in most loading cases, with the only exception being the SD-eng criterion under equi-biaxial tension, which predicted a higher fracture strain than the crack length/area based criteria. This can be explained by the fact that under shear dominated loading conditions, local damage sites in the microstructure (voids and microcracks) tend to distort instead of extend, referred to as void shearing [109–111]. While both distortion and extension can result in loss of load bearing capacity, the effect of distortion is not included in the crack length or area based criteria in the current study.

Table 5.4: Stress triaxiality (η_{avg}^{global}), Lode angle parameter ($\bar{\theta}_{avg}^{global}$), and fracture strain ($\bar{\varepsilon}_f^{global}$) values for different loading types and different microstructure-level fracture criteria.

Loading type		UT	0.55	0.5	0.45	0.4	PST	EBT
CL1	η_{avg}^{global}	0.33	-0.02	0.10	0.20	0.27	0.60	0.66
	$\bar{\theta}_{avg}^{global}$	1.00	-0.05	0.28	0.55	0.69	-0.14	-0.89
	$\bar{\varepsilon}_f^{global}$	0.61	0.76	0.68	0.64	0.64	0.51	0.72
CL2	η_{avg}^{global}	0.33	0.00	0.13	0.20	0.28	0.60	0.66
	$\bar{\theta}_{avg}^{global}$	1.00	0.01	0.40	0.57	0.73	-0.14	-0.89
	$\bar{\varepsilon}_f^{global}$	0.61	0.71	0.61	0.63	0.60	0.51	0.72
CA	η_{avg}^{global}	0.33	0.00	0.10	0.19	0.28	0.60	0.66
	$\bar{\theta}_{avg}^{global}$	1.00	0.02	0.29	0.53	0.71	-0.15	-0.88
	$\bar{\varepsilon}_f^{global}$	0.60	0.71	0.68	0.66	0.62	0.52	0.73
SD-eng	η_{avg}^{global}	0.33	0.22	0.25	0.29	0.33	0.60	0.65
	$\bar{\theta}_{avg}^{global}$	1.00	0.63	0.73	0.80	0.83	-0.13	-0.80
	$\bar{\varepsilon}_f^{global}$	0.61	0.38	0.42	0.45	0.49	0.49	0.79
SD_vM	η_{avg}^{global}	0.33	0.02	0.17	0.26	0.30	0.59	0.67
	$\bar{\theta}_{avg}^{global}$	1.00	0.07	0.50	0.71	0.77	-0.11	-0.94
	$\bar{\varepsilon}_f^{global}$	0.61	0.67	0.56	0.53	0.57	0.45	0.64

5.5.2. Comparison of RVE predictions to macroscale results

To evaluate the predictability of the simulation results, the simulated fracture strains were compared to the stress state dependent macroscopic strain to failure results reported in Chapter 3. As η^{global} and $\bar{\theta}^{global}$ are not constant in the RVE simulations (Figure 5.6), their time averages were taken as the corresponding global stress state values for each loading type. In the present study, they were calculated as follows:

$$\eta_{avg}^{global} = \frac{1}{\bar{\varepsilon}_f^{global}} \int_0^{\bar{\varepsilon}_f^{global}} \eta^{global}\, d\bar{\varepsilon}^p$$

$$\bar{\theta}_{avg}^{global} = \frac{1}{\bar{\varepsilon}_f^{global}} \int_0^{\bar{\varepsilon}_f^{global}} \bar{\theta}^{global}\, d\bar{\varepsilon}^p \qquad \text{Eq. 5.9}$$

The values for each loading condition are given in Table 5.4. Note that for the same loading condition, as $\bar{\varepsilon}_f^{global}$ varied with microstructure-level fracture criteria, the corresponding η_{avg}^{global} and $\bar{\theta}_{avg}^{global}$ values also varied with failure criteria.

Figure 5.7 compares the RVE simulation predictions in the present study and the experimental results in Chapter 3. Given that the plane stress approximation applies to both the RVE model and the experiments, the relationship between stress triaxiality and Lode angle parameter in all cases studied is given as [58]:

$$\sin\left(\frac{\pi}{2}\bar{\theta}_{avg}^{global}\right) = -\frac{27}{2}\eta_{avg}^{global}\left[\left(\eta_{avg}^{global}\right)^2 - \frac{1}{3}\right] \qquad \text{Eq. 5.10}$$

For comparison, the MMC model reported in Chapter 3 is also shown in the figure. Note that this model was calibrated based on the macroscopic experimental results and described the fracture behavior of DP600, while the MMC model in Section 5.2.3 describes the fracture behavior of ferrite only.

As shown in Figure 5.7, under high stress triaxialities ($\eta_{avg}^{global} > 0.33$), the RVE predictions agreed qualitatively with experiments regardless of the RVE-level fracture criterion applied. Quantitatively, the SD-vM criterion achieved the best approximations to experimental data, with a relative error of 25% or less. Under low stress triaxialities ($\eta_{avg}^{global} < 0.33$), the agreement between RVE predictions and experiments was strongly

dependent on RVE-level fracture criteria. The SD-eng criterion had the worst agreement with experiments in this regime, indicating that describing the loss of load bearing capacity through one stress component is insufficient to capture failure over large stress state ranges. The predictions of the three crack length/area based criteria (CL1, CL2 and DA) were similar to each other in this regime, agreeing well with experiments near $\eta_{avg}^{global} = 0.33$ and $\eta_{avg}^{global} = 0$, but overpredicting the strain to failure in between. In addition, while experimental data resulted in a parabolic relationship between strain and stress triaxiality in this regime, the crack length/area based criteria predicted a linear relationship. The SD-vM criterion resulted in the best agreement with experiments as it not only captured the parabolic shape in this region, but also accurately predicted the failure strain, comparable with the macroscopic MMC model.

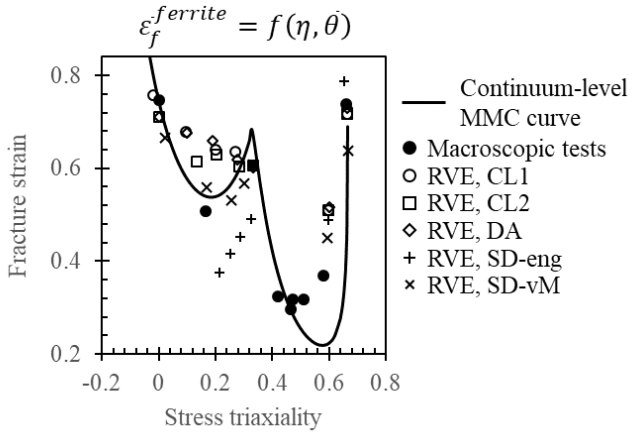

Figure 5.7: Fracture strain of DP600 as a function of stress triaxiality (for the case of plane stress) determined from macroscopic tests and RVE simulations with different RVE-level fracture criteria ($\bar{\varepsilon}_f^{ferrite} = f(\eta, \bar{\theta})$). The continuum-level MMC curve is from Chapter 3.

Note that the above results are compared over a global stress triaxiality range from 0 to 0.67, but the fracture model parameters in Section 5.2.3 and the RVE-level fracture criteria parameters in Section 5.3 were calibrated based on only one stress state: uniaxial tension ($\eta^{global} = 0.33, \bar{\theta}^{global} = 1$). This shows that with properly calibrated fracture models for the constituent phases and a proper RVE-level fracture criterion, RVE models have the potential to describe the macroscopic fracture behavior of DP600.

5.6. Discussion

5.6.1. Microcrack propagation mechanisms

To examine the dependence of RVE-level crack propagation mechanisms on global stress state, the crack initiation and propagation under a low stress triaxiality ($U_1/U_2 = 0.55$) and a high stress triaxiality (plane strain tension) deformation were compared, as shown in Figure 5.8. Under both loading conditions, cracks initiated in martensite, primarily in thin ligaments of martensite, as shown in the inset of Figure 5.8. Under $U_1/U_2 = 0.55$ loading, the initial cracks in martensite propagated into ferrite and new microcracks also formed in ferrite due to strain heterogeneities. These microcracks eventually connected with each other and led to RVE-level failure. Under plane strain tension, however, cracks that initiated in martensite did not propagate into neighboring ferrite. Instead, new microcracks formed in ferrite upon further loading. The propagation of the cracks in ferrite dominated with additional deformation, eventually leading to RVE fracture.

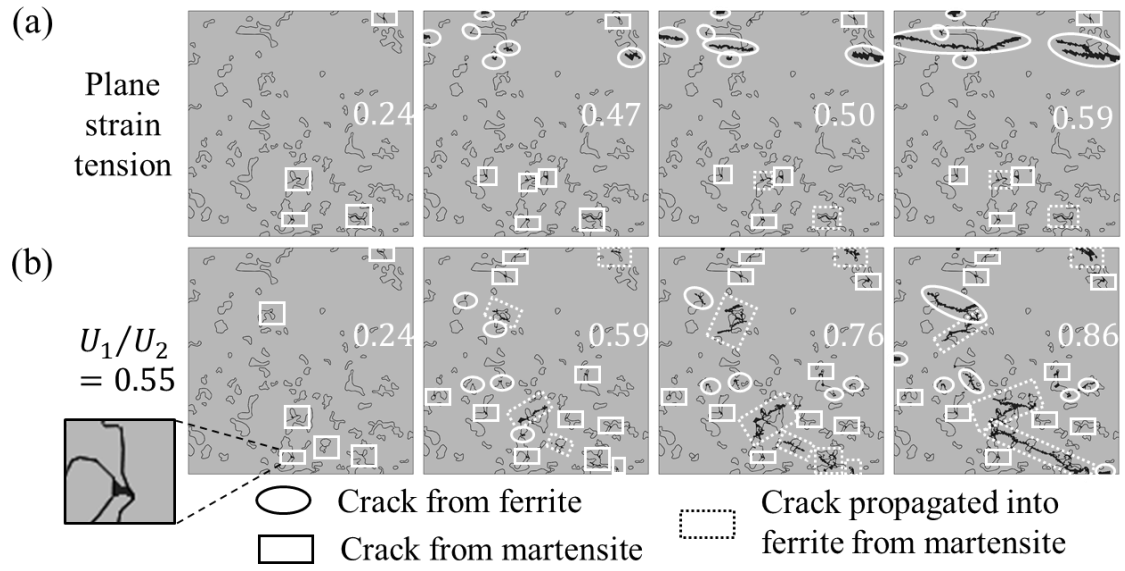

Figure 5.8: Crack initiation and propagation behavior at different global equivalent plastic strain ($\bar{\varepsilon}^{p,global}$) levels under (a) plane strain tension and (b) $U_1/U_2 = 0.55$ loading for $\bar{\varepsilon}_f^{ferrite} = f(\eta, \bar{\theta})$. The numbers in each figure indicate the corresponding $\bar{\varepsilon}^{p,global}$ value.

Since microcrack initiation and propagation correlate with damage accumulation, the local distribution of damage (D, calculated using Eq. 5) under plane strain tension and $U_1/U_2 = 0.55$ loading for $\bar{\varepsilon}_f^{ferrite} = f(\eta, \bar{\theta})$ is shown in Figure 5.9. For high stress triaxiality loading (plane strain tension), plastic strain and damage primarily accumulated in regions with large spacing between martensite, while for low stress triaxiality loading ($U_1/U_2 = 0.55$), plastic strain and damage primarily accumulated in regions with small martensite spacing. The distributions of stress triaxiality and Lode angle parameter in ferrite were also heterogeneous, and were affected not only by martensite spacing, but also

martensite morphology. Specifically, the local stress triaxiality in ferrite was the highest in regions with closely spaced martensite and regions near sharp corners of martensite.

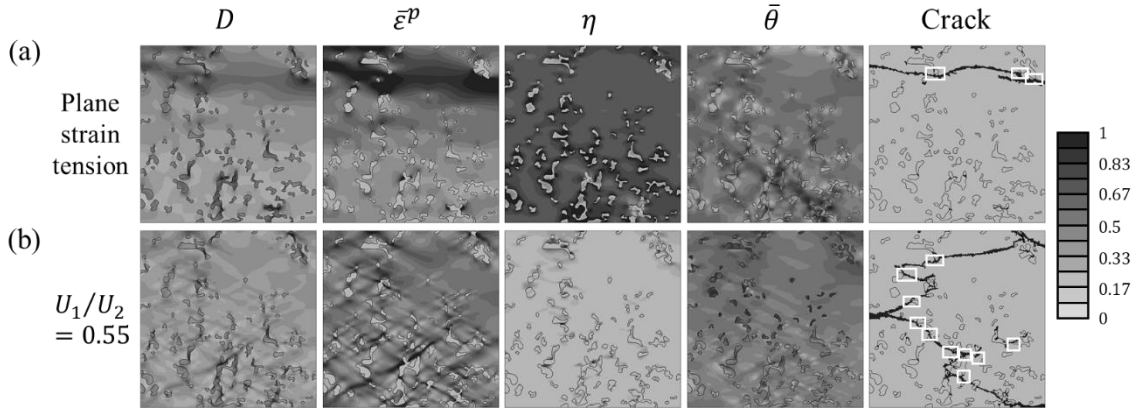

Figure 5.9: Local distributions of damage (D), equivalent plastic strain ($\bar{\varepsilon}^p$), stress triaxiality (η), and Lode angle parameter ($\bar{\theta}$) in the RVE model at a global equivalent plastic strain ($\bar{\varepsilon}^{p,global}$) of 0.41, and final distribution of microcracks, under (a) plane strain tension and (b) $U_1/U_2 = 0.55$ loading for $\bar{\varepsilon}_f^{ferrite} = f(\eta, \bar{\theta})$. Damage is calculated based on Eq. 5.3 for ferrite and based on Eq. 5.5 for martensite. Under plane strain tension, damage and strain localization were highest in the top right region, where the spacing of martensite grains was relatively large, while under $U_1/U_2 = 0.55$ loading, damage and strain localization were highest in the bottom region, where the spacing of martensite grains was relatively small. The boxes in the microcrack distribution images highlight the sharp martensite corners along the crack paths.

The above analysis shows that the propensity for microcracks to form depends on the stress state dependent strain localization behavior, due to material heterogeneity, macroscopic applied stress state, and phase fracture criteria. The heterogeneous

distribution of martensite results in high strain regions in ferrite within large martensite spacing regions for high global stress triaxiality loading and within regions of small martensite spacing for low global stress triaxiality loading). Within these regions, the sharp corners of martensite result in locally high stress triaxiality, leading to damage initiation in ferrite. In addition, the above results showed that even though microcracks initiated in martensite, these cracks did not participate in final RVE-level failure under high stress triaxiality loading, highlighting the importance of studying microcrack initiation plus propagation behavior when investigating the fracture behavior of DP steels.

According to the above results, the ductility of DP steels can potentially be improved by homogeneously distributing the martensite grains in the microstructure. To illustrate this, two additional RVE models with idealized martensite grains were developed, as shown in Figure 5.10. In the two idealized models, one of them has perfectly distributed martensite grains, while the other one has biased martensite grain distribution. The martensite volume fraction and overall model physical size in the idealized models were the same as those of the microstructure-based RVE model in Section 5.2.2. These models were then loaded under seven different loading conditions, in accordance with those in Section 5.2.2, and the SD-vM criterion was adopted as the RVE-level fracture criterion.

The simulated fracture strain under different stress state is shown in Figure 5.11. Within the stress state range investigated, the RVE model with a biased martensite grain distribution had a lower fracture strain compared to the perfect distribution, and this trend was most obvious under high stress triaxiality. This shows that a homogeneous distribution of martensite grains in the material can indeed improve the ductility of DP steels, especially under high stress triaxiality loading.

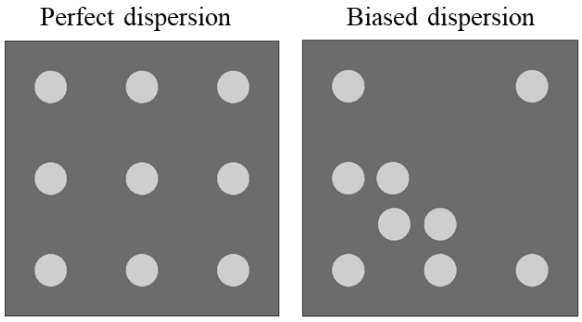

Figure 5.10: The RVE models with an idealized microstructure. The light region corresponds to martensite, and the dark region corresponds to ferrite.

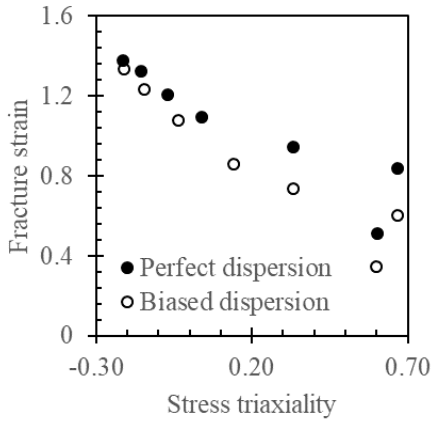

Figure 5.11: The stress state dependent fracture strain of DP600 simulated from the idealized RVE models.

5.6.2. Source of stress state dependence of fracture strain

In DP600, the ferrite phase is ductile, and ductile failure is known to be stress state dependent [50,57,87,109,112]. In the present study, this behavior was captured using the MMC model, as described in Section 5.2.3. The results in Section 5.5 showed that the

corresponding fracture strain of DP600 simulated from the RVE model was also stress state dependent. However, for multiphase materials, whose microstructures are inhomogeneous, the heterogeneities themselves contribute to stress state behavior at the macroscale.

In order to decouple the contributions of stress state dependent ferrite failure and microstructure heterogeneity on macroscale stress state dependent multi-phase microstructure behavior, an additional set of simulations was performed in which a constant strain to failure was adopted for ferrite:

$$\bar{\varepsilon}_f^{ferrite} = \bar{\varepsilon}_{const}^{ferrite} \qquad \text{Eq. 5.11}$$

A value of $\bar{\varepsilon}_{const}^{ferrite} = 1.483$ was used, for which the simulated macroscale fracture strain under uniaxial tension (SD-vM criterion) agreed with experimental data.

The RVE model, with stress state independent fracture models for both ferrite and martensite, was loaded under the same conditions described in Section 5.2.2, and the global fracture strains were calculated as described in Section 5.3. The RVE-level fracture strains under different stress states, along with macroscale strain to failure data, are shown in Figure 5.12. A clear dependence of the fracture strains on stress triaxiality is observed from the RVE simulations, regardless of the RVE-level fracture criteria applied, which indicates that microstructural heterogeneity is a source of stress state dependence of fracture.

To highlight this, the distributions of equivalent plastic strain in the RVE when $\bar{\varepsilon}^{p,global} = 0.3$ and $\bar{\varepsilon}_f^{ferrite} = \bar{\varepsilon}_{const}^{ferrite}$ are compared between different loading conditions in Figure 5.13. At the same global strain, the local strain level is different under different stress states: it is higher under low stress triaxiality loading than under high stress triaxiality

loading, indicating that the strain localization due to microstructure inhomogeneity is stress state dependent, and contributes to the stress state dependence of the global fracture strain shown in Figure 5.12.

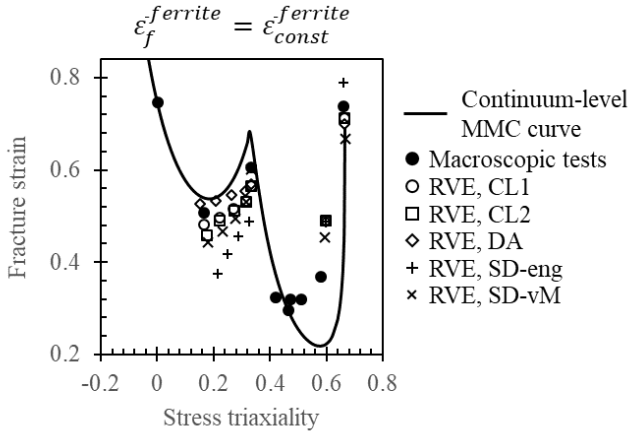

Figure 5.12: Comparison of DP600 fracture strains predicted in RVE simulations with $\bar{\varepsilon}_f^{ferrite} = \bar{\varepsilon}_{const}^{ferrite}$ for different RVE-level fracture criteria. The continuum-level MMC curve is from Chapter 3.

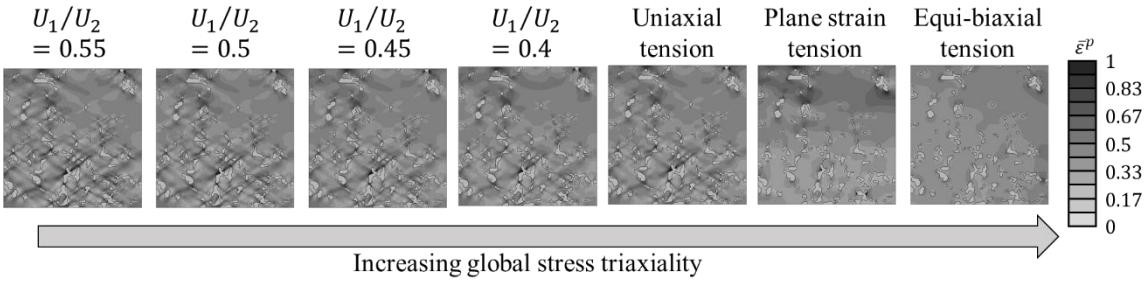

Figure 5.13: Distributions of local equivalent plastic strain in the microstructures for $\bar{\varepsilon}_f^{ferrite} = \bar{\varepsilon}_{const}^{ferrite}$, at a global equivalent plastic strain of 0.3, with increasing global stress triaxiality from left to right. The strain fields are shown on the reference (undeformed) configurations.

5.7. Conclusions

In the present study, the multiaxial fracture behavior of DP600 was investigated through RVE simulations in which fracture criteria for the constituent phases were implemented. The microstructure based RVE model was subjected to seven different stress states. The continuum level stress state dependent fracture strain of the material was predicted from the RVE simulations and was compared with macroscale experimental data. The observed stress state dependent fracture mechanisms were also discussed. The primary contributions of the present study are:

- Five RVE-level fracture criteria were presented, including three based on geometry corresponding to critical crack length or area for failure, and two based a critical deterioration on loading bearing capacity. In the high stress triaxiality range ($\eta_{avg}^{global} > 0.33$), the RVE-level failure strain predicted for each of the microscale criteria qualitatively agreed with macroscale experimental data. In the low stress triaxiality range ($\eta_{avg}^{global} < 0.33$), the geometry based criteria were unable to capture the parabolic shape of the plane stress fracture strain curve. The results of one of the load bearing capacity criteria (SD-vM) agreed well with experiments in this range.
- The microcrack propagation behavior was dependent on both stress state as well. In all simulations, microcracks initiated from martensite. The martensite microcracks then propagated into ferrite only under low stress triaxiality loading, while under high stress triaxiality loading, the martensite microcracks were arrested by neighboring ferrite, and new microcracks subsequently formed in ferrite in regions with large martensite spacing. The

propagation of cracks in ferrite was the dominant failure mechanism under high stress triaxiality loading.

- By altering the criteria for ferrite failure from the stress state dependent MMC model to the stress state independent constant strain model, it was shown that the source of macroscale stress state dependent strain to failure in DP600 can be partially attributed to the inhomogeneous microstructure (in addition to stress state dependent failure behavior of the constituent phases). The microstructure level inhomogeneity resulted in heterogeneous strain fields that depended on the macroscopically applied stress state.

Chapter 6 Summary and future work

6.1. Summary and conclusions

The multiaxial plasticity and fracture behavior of DP600 were investigated at both macroscale and microscale. Continuum level mechanical tests were performed, and the results assisted the development of macroscopic multiaxial plasticity and fracture models of the material. At the microscale, microstructure based finite element models were developed, and were shown to be able to capture the multiaxial plasticity and fracture behavior of DP600 at the continuum scale. At the same time, the microstructure based models provided additional insights into the influence of the inhomogeneous microstructure on the macroscopic mechanical behavior of the material.

The multiaxial plasticity behavior of DP600 was determined through multiaxial loading tests. Its plasticity behavior was found to be independent of stress state and orientation, and a constitutive model with a von Mises yield surface, an associated flow rule, and an isotropic hardening law was developed to describe its continuum level plasticity behavior. A microstructure based RVE model was developed and was shown to be able to capture the macroscopic multiaxial mechanical behavior of DP600. Simulation of the RVE model also showed that plastic deformation and stress triaxiality in the microstructure concentrated in regions with closely situated martensite grains.

The multiaxial fracture behavior of DP600 was determined through a combined experimental and computational approach. Fracture tests were performed on six different specimen geometries, enabling the probe of fracture strains under nine different stress states, covering a wide stress state range ($0 < \eta < 0.67$). Finite element simulations with a J2 plasticity model well captured the force displacement curves of all fracture tests. The

fracture strains and stress state variable values, which cannot be directly measured in experiments, were determined by combining the experiments with finite element simulations. The modified Mohr-Coulomb model was calibrated and was shown to be able to capture the stress state dependent fracture strains of the material.

An idealized RVE model was developed to study the stress state dependent fracture mechanisms of DP steels. A ductile fracture model for the ferrite, a brittle fracture model for the martensite, and a cohesive zone model for the ferrite/martensite interface was implemented, so that all possible fracture localization can be simulated. The RVE model was subjected to five loading conditions. Simulations showed that when the martensite fracture energy and/or the interface cohesive energy were in a certain range, the fracture initiation behavior was stress state dependent; in such cases, fracture initiated from martensite under high global stress triaxialities, from ferrite at intermediate global stress triaxialities, and from the ferrite/martensite interface at low global stress triaxialities. Under pure shear and uniaxial compression loading, fracture never initiated from martensite.

The stress state dependent fracture mechanisms of DP600 were also investigated with an RVE model based on observed microstructure. Fracture models were implemented to the ferrite and the martensite phase, and the model was loaded under seven different stress states. Five microstructure-level fracture criteria were presented, and their capability of predicting the continuum level stress state dependent fracture strains were discussed. It was found that the von Mises stress based criterion best approximated the macroscale experimental data. After changing the ferrite fracture behavior in the model from stress state dependent to stress state independent, the RVE predicted fracture strains were still stress state dependent, showing that the source of the stress state dependence in DP600

fracture behavior can be partially attributed to the inhomogeneous microstructure. The RVE simulations showed that in DP600, the material fails by ferrite microcrack propagation under high stress triaxiality loading, and fails by continuous microcrack initiation accompanied by microcrack propagation under low stress triaxiality loading.

6.2. Future work

The multiaxial plasticity and fractur behavior of DP600 was systematically investigated in the thesis. However, all of the loading conditions in this study was monotonic and proportional, without any change in loading paths. In order to understand the role of microstructure on the macroscopic mechanical behavior of DP600 in service conditions, multiscale investigations under cyclic loading conditions and under non-proportional loading conditions with loading path alterations are needed.

Appendix

Published papers during Ph.D. study

Bobbio, L.D.*, Qin, S.*, Dunbar, A., Michaleris, P. and Beese, A.M., 2017. Characterization of the strength of support structures used in powder bed fusion additive manufacturing of Ti-6Al-4V. *Additive Manufacturing*, 14, pp.60-68. (* Contributed equally)

Qin, S., McLendon, R., Oancea, V. and Beese, A.M., 2018. Micromechanics of multiaxial plasticity of DP600: Experiments and microstructural deformation modeling. *Materials Science and Engineering: A*, 721, pp.168-178.

Wilson-Heid, A.E., Qin, S. and Beese, A.M., 2018. Anisotropic multiaxial plasticity model for laser powder bed fusion additively manufactured Ti-6Al-4V. *Materials Science and Engineering: A*, 738, pp.90-97.

Shang, S.L., Shimanek, J., Qin, S., Wang, Y., Beese, A.M. and Liu, Z.K., 2020. Unveiling dislocation characteristics in N i 3 Al from stacking fault energy and ideal strength: A first-principles study via pure alias shear deformation. *Physical Review B*, 101(2), p.024102.

Qin, S., Lu, Y., Sinnott, S.B. and Beese, A.M., 2020. Influence of phase and interface properties on the stress state dependent fracture initiation behavior in DP steels through computational modeling. *Materials Science and Engineering: A*, p.138981.

Qin, S. and Beese, A.M., 2020. Multiaxial fracture of DP600: through mechanical testing experiments and finite element modeling. *Submitted*.

Qin, S, Shang, S-L, Shimanek, J., Liu, Z-K, Beese, A. M., Macroscopic plastic deformation through an integrated first-principles calculations and finite element simulations: Application to nickel single crystal. *Submitted*.

Qin, S. and Beese, A.M., 2020. Multiaxial fracture of DP600 and the microstructural level mechanisms through micromechanics modeling. *In prep*.

Bibliography

[1] M. Bhargava, A. Tewari, S.K. Mishra, Forming limit diagram of Advanced High Strength Steels (AHSS) based on strain-path diagram, Mater. Des. 85 (2015) 149–155. doi:10.1016/j.matdes.2015.06.147.

[2] M.Y. Demeri, Advanced High Strength Steels: Science, Technology and Applications, ASM international, 2013.

[3] WorldAutoSteel, Dual Phase (DP) Steels, (n.d.). http://www.worldautosteel.org/steel-basics/steel-types/dual-phase-dp-steels/.

[4] A. Alaie, S.Z. Rad, J. Kadkhodapour, M. Jafari, M.A. Asadabad, S. Schmauder, Effect of microstructure pattern on the strain localization in DP600 steels analyzed using combined in-situ experimental test and numerical simulation, Mater. Sci. Eng. A. 638 (2015) 251–261. doi:10.1016/j.msea.2015.04.071.

[5] R.-M. Rodriguez, I. Gutiérrez, Unified Formulation to Predict the Tensile Curves of Steels with Different Microstructures, Mater. Sci. Forum. 426–432 (2003) 4525–4530. doi:10.4028/www.scientific.net/MSF.426-432.4525.

[6] N.J. Kim, G. Thomas, Effects of morphology on the mechanical behavior of a DP Fe 2Si 0.1C steel, Metall. Trans. A. 12 (1981) 483–189. file://ce/rd_organisation/PTA-MAD/Common/10 Literature/2008/AHSS/DP/Kim (1981) # Effects of morphology on the mechanical behavior of a DP Fe 2Si 0.1C steel.pdf.

[7] A.M. Sherman, R.G. Davies, Influence of martensite carbon content on the cyclic properties of dual-phase steel, Int. J. Fatigue. 3 (1981) 195–198. doi:10.1016/0142-

1123(81)90020-7.

[8] W.C. Leslie, The physical metallurgy of steels, 1981.

[9] D. Mohr, M. Oswald, A new experimental technique for the multi-axial testing of advanced high strength steel sheets, Exp. Mech. 48 (2008) 65–77. doi:10.1007/s11340-007-9053-9.

[10] D. Mohr, M. Dunand, K.H. Kim, Evaluation of associated and non-associated quadratic plasticity models for advanced high strength steel sheets under multi-axial loading, Int. J. Plast. 26 (2010) 939–956. doi:10.1016/j.ijplas.2009.11.006.

[11] M. Dunand, D. Mohr, Optimized butterfly specimen for the fracture testing of sheet materials under combined normal and shear loading, Eng. Fract. Mech. 78 (2011) 2919–2934. doi:10.1016/j.engfracmech.2011.08.008.

[12] M. Dunand, D. Mohr, On the predictive capabilities of the shear modified Gurson and the modified Mohr-Coulomb fracture models over a wide range of stress triaxialities and Lode angles, J. Mech. Phys. Solids. 59 (2011) 1374–1394. doi:10.1016/j.jmps.2011.04.006.

[13] K.L. Nielsen, V. Tvergaard, Ductile shear failure or plug failure of spot welds modelled by modified Gurson model, Eng. Fract. Mech. 77 (2010) 1031–1047. doi:10.1016/j.engfracmech.2010.02.031.

[14] Y. Bai, T. Wierzbicki, Application of extended Mohr – Coulomb criterion to ductile fracture, Int. J. Fract. 161 (2010) 1–20. doi:10.1007/s10704-009-9422-8.

[15] J. Lian, M. Sharaf, F. Archie, S. Münstermann, A hybrid approach for modelling of

plasticity and failure behaviour of advanced high-strength steel sheets, Int. J. Damage Mech. 22 (2013) 188–218. doi:10.1177/1056789512439319.

[16] N. Habibi, A. Ramazani, V. Sundararaghavan, U. Prahl, Failure predictions of DP600 steel sheets using various uncoupled fracture criteria, Eng. Fract. Mech. 190 (2018) 367–381. doi:10.1016/j.engfracmech.2017.12.022.

[17] Y. Tomota, I. Tamura, Mechanical Behavior of Steels Consisting of Two Ductile Phases, Trans. Iron Steel Inst. Japan. 22 (1982) 665–677. doi:10.2355/isijinternational1966.22.665.

[18] G. Avramovic-Cingara, Y. Ososkov, M.K. Jain, D.S. Wilkinson, Effect of martensite distribution on damage behaviour in DP600 dual phase steels, Mater. Sci. Eng. A. 516 (2009) 7–16. doi:10.1016/j.msea.2009.03.055.

[19] A.F. Szewczyk, J. Gurland, A Study of the Deformation and Fracture of a Dual-Phase Steel, Metall. Trans. A. 13 (1982) 1821–1826. doi:10.1007/BF02647838.

[20] H. Ghadbeigi, C. Pinna, S. Celotto, Failure mechanisms in DP600 steel: Initiation, evolution and fracture, Mater. Sci. Eng. A. 588 (2013) 420–431. doi:10.1016/j.msea.2013.09.048.

[21] M. Sarwar, R. Priestner, Influence of ferrite-martensite microstructural morphology on tensile properties of dual-phase steel, J. Mater. Sci. 31 (1996) 2091–2095. doi:10.1007/BF00356631.

[22] H. Ghadbeigi, C. Pinna, S. Celotto, J.R. Yates, Local plastic strain evolution in a high strength dual-phase steel, Mater. Sci. Eng. A. 527 (2010) 5026–5032. doi:10.1016/j.msea.2010.04.052.

[23] M. Jafari, S. Ziaei-Rad, N. Saeidi, M. Jamshidian, Micromechanical analysis of martensite distribution on strain localization in dual phase steels by scanning electron microscopy and crystal plasticity simulation, Mater. Sci. Eng. A. 670 (2016) 57–67. doi:10.1016/j.msea.2016.05.094.

[24] J. Kadkhodapour, A. Butz, S. Ziaei Rad, Mechanisms of void formation during tensile testing in a commercial, dual-phase steel, Acta Mater. 59 (2011) 2575–2588. doi:10.1016/j.actamat.2010.12.039.

[25] N. Saeidi, F. Ashrafizadeh, B. Niroumand, M.R. Forouzan, F. Barlat, Damage mechanism and modeling of void nucleation process in a ferrite-martensite dual phase steel, Eng. Fract. Mech. 127 (2014) 97–103. doi:10.1016/j.engfracmech.2014.05.017.

[26] N. Saeidi, F. Ashrafizadeh, B. Niroumand, F. Barlat, Evaluation of Fracture Micromechanisms in a Fine-Grained Dual Phase Steel during Uniaxial Tensile Deformation, Steel Res. Int. 85 (2014) 1386–1392. doi:10.1002/srin.201300344.

[27] H. Toda, A.A. Takijiri, M. Azuma, S. Yabu, K. Hayashi, D. Seo, M. Kobayashi, K. Hirayama, A. Takeuchi, K. Uesugi, Damage micromechanisms in dual-phase steel investigated with combined phase- and absorption-contrast tomography, Acta Mater. 126 (2017) 401–412. doi:10.1016/j.actamat.2017.01.010.

[28] E.Y. Guo, M.Y. Wang, T. Jing, N. Chawla, Temperature-dependent mechanical properties of an austenitic-ferritic stainless steel studied by in situ tensile loading in a scanning electron microscope (SEM), Mater. Sci. Eng. A. 580 (2013) 159–168. doi:10.1016/j.msea.2013.04.060.

[29] M. Calcagnotto, Y. Adachi, D. Ponge, D. Raabe, Deformation and fracture mechanisms in fine- and ultrafine-grained ferrite/martensite dual-phase steels and the effect of aging, Acta Mater. 59 (2011) 658–670. doi:10.1016/j.actamat.2010.10.002.

[30] C.C. Tasan, J.P.M. Hoefnagels, M. Diehl, D. Yan, F. Roters, D. Raabe, Strain localization and damage in dual phase steels investigated by coupled in-situ deformation experiments and crystal plasticity simulations, Int. J. Plast. 63 (2014) 198–210. doi:10.1016/j.ijplas.2014.06.004.

[31] C.C. Tasan, M. Diehl, D. Yan, C. Zambaldi, P. Shanthraj, F. Roters, D. Raabe, Integrated experimental-simulation analysis of stress and strain partitioning in multiphase alloys, Acta Mater. 81 (2014) 386–400. doi:10.1016/j.actamat.2014.07.071.

[32] S. Qin, R. McLendon, V. Oancea, A.M. Beese, Micromechanics of multiaxial plasticity of DP600: experiments and microstructural deformation modeling, Mater. Sci. Eng. A. 721 (2018) 168–178. doi:10.1016/j.msea.2018.02.078.

[33] S.K. Paul, A. Kumar, Micromechanics based modeling to predict flow behavior and plastic strain localization of dual phase steels, Comput. Mater. Sci. 63 (2012) 66–74. doi:10.1016/j.commatsci.2012.05.061.

[34] A. Ramazani, M. Abbasi, S. Kazemiabnavi, S. Schmauder, R. Larson, U. Prahl, Development and application of a microstructure-based approach to characterize and model failure initiation in DP steels using XFEM, Mater. Sci. Eng. A. 660 (2016) 181–194. doi:10.1016/j.msea.2016.02.090.

[35] V. Uthaisangsuk, U. Prahl, W. Bleck, Modelling of damage and failure in multiphase high strength DP and TRIP steels, Eng. Fract. Mech. 78 (2011) 469–486. doi:10.1016/j.engfracmech.2010.08.017.

[36] X. Sun, K.S. Choi, W.N. Liu, M.A. Khaleel, Predicting failure modes and ductility of dual phase steels using plastic strain localization, Int. J. Plast. 25 (2009) 1888–1909. doi:10.1016/j.ijplas.2008.12.012.

[37] A. Ramazani, K. Mukherjee, U. Prahl, W. Bleck, Modelling the effect of microstructural banding on the flow curve behaviour of dual-phase (DP) steels, Comput. Mater. Sci. 52 (2012) 46–54. doi:10.1016/j.commatsci.2011.05.041.

[38] V. Uthaisangsuk, U. Prahl, W. Bleck, Failure modeling of multiphase steels using representative volume elements based on real microstructures, Procedia Eng. 1 (2009) 171–176. doi:10.1016/j.proeng.2009.06.040.

[39] L. Madej, J. Wang, K. Perzynski, P.D. Hodgson, Numerical modeling of dual phase microstructure behavior under deformation conditions on the basis of digital material representation, Comput. Mater. Sci. 95 (2014) 651–662. doi:10.1016/j.commatsci.2014.08.035.

[40] P. Chen, H. Ghassemi-Armaki, S. Kumar, A. Bower, S. Bhat, S. Sadagopan, Microscale-calibrated modeling of the deformation response of dual-phase steels, Acta Mater. 65 (2014) 133–149. doi:10.1016/j.actamat.2013.11.036.

[41] J.L. Stewart, L. Jiang, J.J. Williams, N. Chawla, Prediction of bulk tensile behavior of dual phase stainless steels using constituent behavior from micropillar compression experiments, Mater. Sci. Eng. A. 534 (2012) 220–227.

doi:10.1016/j.msea.2011.11.062.

[42] E.Y. Guo, H.X. Xie, S.S. Singh, A. Kirubanandham, T. Jing, N. Chawla, Mechanical characterization of microconstituents in a cast duplex stainless steel by micropillar compression, Mater. Sci. Eng. A. 598 (2014) 98–105. doi:10.1016/j.msea.2014.01.002.

[43] E.Y. Guo, S.S. Singh, H.X. Xie, J.J. Williams, T. Jing, N. Chawla, Microstructure-based modeling of deformation in steels based on constitutive relationships from micropillar compression, Steel Res. Int. 85 (2014) 946–953. doi:10.1002/srin.201300217.

[44] G. Cheng, K.S. Choi, X. Hu, X. Sun, Determining individual phase properties in a multi-phase Q&P steel using multi-scale indentation tests, Mater. Sci. Eng. A. 652 (2016) 384–395. doi:10.1016/j.msea.2015.11.072.

[45] G. Cheng, F. Zhang, A. Ruimi, D.P. Field, X. Sun, Quantifying the effects of tempering on individual phase properties of DP980 steel with nanoindentation, Mater. Sci. Eng. A. 667 (2016) 240–249. doi:10.1016/j.msea.2016.05.011.

[46] S.H. Choi, E.Y. Kim, W. Woo, S.H. Han, J.H. Kwak, The effect of crystallographic orientation on the micromechanical deformation and failure behaviors of DP980 steel during uniaxial tension, Int. J. Plast. 45 (2013) 85–102. doi:10.1016/j.ijplas.2012.11.013.

[47] F.M. Al-Abbasi, J.A. Nemes, Micromechanical modeling of dual phase steels, Int. J. Mech. Sci. 45 (2003) 1449–1465. doi:10.1016/j.ijmecsci.2003.10.007.

[48] S. Sodjit, V. Uthaisangsuk, Microstructure based prediction of strain hardening

behavior of dual phase steels, Mater. Des. 41 (2012) 370–379. doi:10.1016/j.matdes.2012.05.010.

[49] J. Lian, H. Yang, N. Vajragupta, S. Münstermann, W. Bleck, A method to quantitatively upscale the damage initiation of dual-phase steels under various stress states from microscale to macroscale, Comput. Mater. Sci. 94 (2014) 245–257. doi:10.1016/j.commatsci.2014.05.051.

[50] V. Tvergaard, A. Needleman, Analysis of the Cup-Cone Round Tensile Fracture, Acta Metall. 32 (1984) 157–169. doi:10.1016/0001-6160(84)90213-X.

[51] T. Sirinakorn, V. Uthaisangsuk, Investigation of damage initiation in high-strength dual-phase steels using cohesive zone model, Int. J. Damage Mech. 27 (2018) 409–438. doi:10.1177/1056789516679718.

[52] K.S. Choi, W.N. Liu, X. Sun, M.A. Khaleel, Influence of martensite mechanical properties on failure mode and ductility of dual-phase steels, Metall. Mater. Trans. A Phys. Metall. Mater. Sci. 40 (2009) 796–809. doi:10.1007/s11661-009-9792-6.

[53] X. Sun, K.S. Choi, A. Soulami, W.N. Liu, M.A. Khaleel, On key factors influencing ductile fractures of dual phase (DP) steels, Mater. Sci. Eng. A. 526 (2009) 140–149. doi:10.1016/j.msea.2009.08.010.

[54] X. Sun, K.S. Choi, W.N. Liu, M.A. Khaleel, Predicting failure modes and ductility of dual phase steels using plastic strain localization, Int. J. Plast. 25 (2009) 1888–1909. doi:10.1016/j.ijplas.2008.12.012.

[55] T. Sirinakorn, S. Wongwises, V. Uthaisangsuk, A study of local deformation and damage of dual phase steel, Mater. Des. 64 (2014) 729–742.

doi:10.1016/j.matdes.2014.08.009.

[56] D. Gerbig, A. Srivastava, S. Osovski, L.G. Hector, A. Bower, Analysis and design of dual-phase steel microstructure for enhanced ductile fracture resistance, Int. J. Fract. 209 (2018) 3–26. doi:10.1007/s10704-017-0235-x.

[57] A.L. Gurson, Continuum Theory of Ductile Rupture by Void Nucleation and Growth: Part I—Yield Criteria and Flow Rules for Porous Ductile Media, J. Eng. Mater. Technol. 99 (1977) 2. doi:10.1115/1.3443401.

[58] Y. Bai, T. Wierzbicki, A new model of metal plasticity and fracture with pressure and Lode dependence, Int. J. Plast. 24 (2008) 1071–1096. doi:10.1016/j.ijplas.2007.09.004.

[59] M. Luo, M. Dunand, D. Mohr, Experiments and modeling of anisotropic aluminum extrusions under multi-axial loading – Part II : Ductile fracture, Int. J. Plast. 32–33 (2012) 36–58. doi:10.1016/j.ijplas.2011.11.001.

[60] A.M. Beese, M. Luo, Y. Li, Y. Bai, T. Wierzbicki, Partially coupled anisotropic fracture model for aluminum sheets, Eng. Fract. Mech. 77 (2010) 1128–1152. doi:10.1016/j.engfracmech.2010.02.024.

[61] ASTM, Standard Specification for Steel , Sheet , Cold-Rolled , Complex Phase (CP), Dual Phase (DP) and Transformation Induced Plasticity (TRIP), ASTM Int. (2015) 1–5. doi:10.1520/A1088-13.

[62] ASTM, E8/E8M standard test methods for tension testing of metallic materials, ASTM Int. (2010) 1–25. doi:10.1520/E0008.

[63] P. Reu, Virtual Strain Gage Size Study, Exp. Tech. 39 (2015) 1–3. doi:10.1111/ext.12172.

[64] Abaqus User Manual v2016, DS SIMULIA. (2016). https://www.3ds.com/products-services/simulia/.

[65] J. Zhou, A.M. Gokhale, A. Gurumurthy, S.P. Bhat, Realistic microstructural RVE-based simulations of stress – strain behavior of a dual-phase steel having high martensite volume fraction, Mater. Sci. Eng. A. 630 (2015) 107–115. doi:10.1016/j.msea.2015.02.017.

[66] S. Langer, E. Fuller, C. Carter, OOF: image-based finite-element analysis of material microstructures, Mater. Sci. 3 (2001) 15–23.

[67] S. Langer, A.C. Reid, S.I. Haan, R.E. Garcia, R.C. Lua, V.R. Coffman, The OOF2 manual, NIST. (2008).

[68] Synopsys, Simpleware, (n.d.). https://www.synopsys.com/.

[69] A. Ramazani, K. Mukherjee, H. Quade, U. Prahl, W. Bleck, Correlation between 2D and 3D flow curve modelling of DP steels using a microstructure-based RVE approach, Mater. Sci. Eng. A. 560 (2013) 129–139. doi:10.1016/j.msea.2012.09.046.

[70] M. Destrade, J.G. Murphy, G. Saccomandi, Simple shear is not so simple, Int. J. Non. Linear. Mech. 47 (2012) 210–214. doi:10.1016/j.ijnonlinmec.2011.05.008.

[71] A.I. Lurie, Theory of Elasticity, Springer, 2005.

[72] T. Tancogne-Dejean, C.C. Roth, U. Woy, D. Mohr, Probabilistic fracture of Ti-6Al-

4V made through additive layer manufacturing, Int. J. Plast. 78 (2016) 145–172. doi:10.1016/j.ijplas.2015.09.007.

[73] R. v. Mises, Mechanik der festen Körper im plastisch-deformablen Zustand, Nachrichten von Der Gesellschaft Der Wissenschaften Zu Göttingen, Math. Klasse. (1913) 582–592.

[74] P.J. Jacques, Q. Furnemont, S. Godet, T. Pardoen, K.T. Conlon, F. Delannay, Micromechanical characterisation of TRIP-assisted multiphase steels by in situ neutron diffraction, Philos. Mag. 86 (2006) 2371–2392. doi:10.1080/14786430500529359.

[75] C.C. Roth, D. Mohr, Effect of strain rate on ductile fracture initiation in advanced high strength steel sheets : Experiments and modeling, Int. J. Plast. 56 (2014) 19–44. doi:10.1016/j.ijplas.2014.01.003.

[76] C.C. Roth, D. Mohr, Ductile fracture experiments with locally proportional loading histories, Int. J. Plast. 79 (2016) 328–354. doi:10.1016/j.ijplas.2015.08.004.

[77] Y. Bai, Effect of loading history on necking and fracture, Massachusetts Institute of Technology, 2008.

[78] Abaqus User Manual v2017, DS SIMULIA. (2017). https://www.3ds.com/products-services/simulia/.

[79] F.M. Al-Abbasi, J.A. Nemes, Predicting the ductile failure of DP-steels using micromechanical modeling of cells, Int. J. Damage Mech. 17 (2008) 447–472. doi:10.1177/1056789507077441.

[80] V. Uthaisangsuk, U. Prahl, W. Bleck, Micromechanical modelling of damage behaviour of multiphase steels, Comput. Mater. Sci. 43 (2008) 27–35. doi:10.1016/j.commatsci.2007.07.035.

[81] V. Uthaisangsuk, U. Prahl, W. Bleck, Characterisation of formability behaviour of multiphase steels by micromechanical modelling, Int. J. Fract. 157 (2009) 55–69. doi:10.1007/s10704-009-9329-4.

[82] H. Hosseini-Toudeshky, B. Anbarlooie, J. Kadkhodapour, Micromechanics stress-strain behavior prediction of dual phase steel considering plasticity and grain boundaries debonding, Mater. Des. 68 (2015) 167–176. doi:10.1016/j.matdes.2014.12.013.

[83] T. Matsuno, C. Teodosiu, D. Maeda, A. Uenishi, Mesoscale simulation of the early evolution of ductile fracture in dual-phase steels, Int. J. Plast. 74 (2015) 17–34. doi:10.1016/J.IJPLAS.2015.06.004.

[84] A. Weck, D.S. Wilkinson, E. Maire, H. Toda, Visualization by X-ray tomography of void growth and coalescence leading to fracture in model materials, Acta Mater. 56 (2008) 2919–2928. doi:10.1016/j.actamat.2008.02.027.

[85] A.A. Benzerga, J. Leblond, Ductile Fracture by Void Growth to Coalescence.pdf, (2010).

[86] Y. Bao, T. Wierzbicki, On the cut-off value of negative triaxiality for fracture, Eng. Fract. Mech. 72 (2005) 1049–1069. doi:10.1016/j.engfracmech.2004.07.011.

[87] J.R. Rice, D.M. Tracey, On the ductile enlargement of voids in triaxial stress fields, J. Mech. Phys. Solids. 17 (1969) 201–217. doi:10.1016/0022-5096(69)90033-7.

[88] C.A. Coulomb, Essai sur une application des regles de maximis et minimis a quelques problemes de statique relatifs a l'architecture (essay on maximums and minimums of rules to some static problems relating to architecture), (1973).

[89] S.H. Choi, E.Y. Kim, W. Woo, S.H. Han, J.H. Kwak, The effect of crystallographic orientationonthe micromechanical deformation and failure behaviors of DP980 steel during uniaxial tension, Int. J. Plast. 45 (2013) 85–102. doi:10.1016/j.ijplas.2012.11.013.

[90] H. Yuan, X. Li, Effects of the cohesive law on ductile crack propagation simulation by using cohesive zone models, Eng. Fract. Mech. 126 (2014) 1–11. doi:10.1016/j.engfracmech.2014.04.019.

[91] I. Scheider, W. Brocks, Simulation of cup–cone fracture using the cohesive model, Eng. Fract. Mech. 70 (2003) 1943–1961. doi:10.1016/S0013-7944(03)00133-4.

[92] K.L. Roe, T. Siegmund, An irreversible cohesive zone model for interface fatigue crack growth simulation, Eng. Fract. Mech. 70 (2003) 209–232.

[93] M. Nouroozi, H. Mirzadeh, M. Zamani, Effect of microstructural refinement and intercritical annealing time on mechanical properties of high-formability dual phase steel, Mater. Sci. Eng. A. 736 (2018) 22–26. doi:10.1016/j.msea.2018.08.088.

[94] R. Östlund, M. Oldenburg, H.A. Häggblad, D. Berglund, Numerical failure analysis of steel sheets using a localization enhanced element and a stress based fracture criterion, Int. J. Solids Struct. 56 (2015) 1–10. doi:10.1016/j.ijsolstr.2014.12.010.

[95] A. Ramazani, S. Kazemiabnavi, R. Larson, Quantification of ferrite-martensite interface in dual phase steels: A first-principles study, Acta Mater. 116 (2016) 231–

237. doi:10.1016/j.actamat.2016.06.047.

[96] J.Y. Koo, M.J. Young, G. Thomas, On the law of mixtures in dual-phase steels, Metall. Trans. A. 11 (1980) 852–854. doi:10.1007/BF02661217.

[97] Thermodynamic database TCFE6 – TCS Steels/Fe-Alloys Database, (n.d.). www.thermocalc.com.

[98] P.E. Blöchl, Projector augmented-wave method, Phys. Rev. B. 50 (1994) 17953–17979. doi:10.1142/9789814365031_0023.

[99] G. Kresse, J. Furthmüller, Efficient iterative schemes for ab initio total-energy calculations using a plane-wave basis set, Phys. Rev. B. 54 (1996) 11169–11186. doi:10.1103/PhysRevB.54.11169.

[100] J.P. Perdew, K. Burke, M. Ernzerhof, Generalized Gradient Approximation Made Simple, Phys. Rev. Lett. 77 (1996) 3865–3868.

[101] Y.J. Chao, J.D. Ward, R.G. Sands, Charpy impact energy, fracture toughness and ductile-brittle transition temperature of dual-phase 590 Steel, Mater. Des. 28 (2007) 551–557. doi:10.1016/j.matdes.2005.08.009.

[102] F. Ozturk, S. Toros, S. Kilic, Effects of anisotropic yield functions on prediction of forming limit diagrams of DP600 advanced high strength steel, Procedia Eng. 81 (2014) 760–765. doi:10.1016/j.proeng.2014.10.073.

[103] A. Ramazani, M. Abbasi, U. Prahl, W. Bleck, Failure analysis of DP600 steel during the cross-die test, Comput. Mater. Sci. 64 (2012) 101–105. doi:10.1016/j.commatsci.2012.01.031.

[104] S. Qin, A.M. Beese, Multiaxial fracture of DP600: experiments and finite element modeling, Submitted. (2020).

[105] R.E. Smallman, R.J. Bishop, Metals and Materials: Science, Processes, Applications, Elsevier, 2013.

[106] Y. Lu, H. Yu, R.D. Sisson, The effect of carbon content on the c/a ratio of as-quenched martensite in Fe-C alloys, Mater. Sci. Eng. A. 700 (2017) 592–597. doi:10.1016/j.msea.2017.05.094.

[107] M. Calcagnotto, D. Ponge, E. Demir, D. Raabe, Orientation gradients and geometrically necessary dislocations in ultrafine grained dual-phase steels studied by 2D and 3D EBSD, Mater. Sci. Eng. A. 527 (2010) 2738–2746. doi:10.1016/j.msea.2010.01.004.

[108] S. Qin, Y. Lu, S.B. Sinnott, A.M. Beese, Influence of phase and interface properties on the stress state dependent fracture initiation behavior in DP steels through computational modeling, Mater. Sci. Eng. A. 776 (2020) 138981. doi:10.1016/j.msea.2020.138981.

[109] F.A. McClintock, S.M. Kaplan, C.A. Berg, Ductile fracture by hole growth in shear bands, Int. J. Fract. Mech. 2 (1966) 614–627. doi:10.1007/BF00184558.

[110] L. Xue, Constitutive modeling of void shearing effect in ductile fracture of porous materials, Eng. Fract. Mech. 75 (2008) 3343–3366. doi:10.1016/j.engfracmech.2007.07.022.

[111] K. Nahshon, J.W. Hutchinson, Modification of the Gurson Model for shear failure, Eur. J. Mech. - A/Solids. 27 (2008) 1–17. doi:10.1016/j.euromechsol.2007.08.002.

[112] A.A. Benzerga, Micromechanics of coalescence in ductile fracture, J. Mech. Phys. Solids. 50 (2002) 1331–1362. doi:10.1016/S0022-5096(01)00125-9.

VITA

Shipin Qin

Shipin Qin was born in 1990 in Shimen, Hunan province in China. He obtained his B.S. degree in Engineering Mechanics and M.S. degree in Mechanical Engineering from Beijing Institute of Technology. He started his Ph.D. student in Materials Science and Engineering at the Pennsylvania State University in August 2015. His research involves microstructural characterization and computational modeling of dual phase steels and additively manufactured metals.